

UC Irvine

UC Irvine Electronic Theses and Dissertations

Title

Density-Matrix Renormalization Group and Model Reduction Studies of Two-Dimensional Doped and Frustrated Systems

Permalink

<https://escholarship.org/uc/item/6136z0tz>

Author

Jiang, Shengtao

Publication Date

2024

Copyright Information

This work is made available under the terms of a Creative Commons Attribution License, available at <https://creativecommons.org/licenses/by/4.0/>

Peer reviewed|Thesis/dissertation

UNIVERSITY OF CALIFORNIA,
IRVINE

Density-Matrix Renormalization Group and Model Reduction Studies of Two-Dimensional
Doped and Frustrated Systems

DISSERTATION

submitted in partial satisfaction of the requirements
for the degree of

DOCTOR OF PHILOSOPHY

in Physics

by

Shengtao Jiang

Dissertation Committee:
Professor Steven R. White, Chair
Professor A. L. Chernyshev
Assistant Professor Judit Romhányi

2024

Chapter 2 © National Academy of Sciences
Chapter 2 © American Physical Society
Chapter 3 © American Physical Society
Chapter 4 © American Physical Society
Chapter 5 © American Physical Society
All other materials © 2024 Shengtao Jiang

DEDICATION

To my parents.

TABLE OF CONTENTS

	Page
LIST OF FIGURES	v
LIST OF TABLES	xiii
ACKNOWLEDGMENTS	xiv
VITA	xvi
ABSTRACT OF THE DISSERTATION	xviii
1 Introduction	1
1.1 Simulating strongly correlated many-electron problems	1
1.2 Historical development of DMRG and tensor network states	3
1.3 Entanglement entropy and matrix product state representation of quantum many-body wavefunctions	5
1.4 Formulating the DMRG algorithm using matrix product states	7
1.5 Studying two-dimensional systems with DMRG	10
1.6 Spontaneously broken symmetry in DMRG calculations	12
1.7 Finite-size scaling of local order parameters	16
1.8 DMRG scan calculations	18
1.9 Organization of the thesis	21
2 Ground state phase diagram of the extended t-J models	22
2.1 Introduction	22
2.2 Model and method	25
2.3 Phase diagram	26
2.4 Scans varying doping and t'	31
2.5 Electron low-doped phase with coexisting uniform AFM, d -wave singlet and (π, π) p -wave triplet pairing (AFM- $d/\pi p$)	37
2.6 Higher electron doping phase: stripes with d -wave singlet and striped p -wave pairing	39
2.7 Conventional stripe phase and low-doped W3 stripe phase	41
2.8 Energy gaps	43
2.9 Comparisons with width-6 cylinders	45
2.10 Comparison to the cuprates	48

2.11	Inclusion of the third nearest neighbor hopping t''	50
2.12	Summary	51
3	DMRG-based downfolding of the three-band Hubbard model: Importance of density-assisted hopping	53
3.1	Introduction	53
3.2	The three-band Hubbard model	55
3.3	Downfolding into a Wannier single-band model	57
3.4	Effects of t_n	63
3.5	Summary and discussion	65
4	Quantum Spin Nematic in the Square-Lattice J_1-J_2 Ferro-antiferromagnetic Heisenberg Model	67
4.1	Introduction	67
4.2	d -wave pair-BEC	69
4.3	Phase diagram	71
4.4	DMRG results	73
4.5	Reduction of the single-magnon gap in the presence of pairs	78
4.6	Multi-pair states	79
4.7	First order transition from FM to AFM at $J_2 = 0.45$	83
4.8	Summary	84
5	Quantum Phases in Frustrated Honeycomb Spin Models for Kitaev Material Candidates	86
5.1	Introduction	86
5.2	Phase diagram	89
5.3	DMRG calculations	90
5.4	Minimally-augmented spin-wave theory	94
5.5	MAGSWT results	96
5.6	The J_1^Δ - J_3^Δ model	97
5.7	Pseudo-spin-liquid state	99
5.8	Generalized $J_1^{\Delta_1}$ - $J_3^{\Delta_3}$ model for $\text{BaCo}_2(\text{AsO}_4)_2$	101
5.9	The generalized Kitaev- J_3 model for α - RuCl_3	102
5.10	Summary	105
	Bibliography	106
	Appendix A Supplemental materials for Chapter 2	121
	Appendix B Supplemental materials for Chapter 3	124
	Appendix C Supplemental materials for Chapter 4	128
	Appendix D Supplemental materials for Chapter 5	146

LIST OF FIGURES

	Page
1.1 Decomposition of a rank- N tensor $\psi_{s_1, s_2, \dots, s_N}$ that represents a wavefunction into a MPS made of $N-2$ rank-3 tensors in the bulk and two rank-2 tensors on the edges: $\psi_{s_1, s_2, \dots, s_N} = \sum_{l_1, l_2, \dots, l_n} A_{l_1}^{s_1} A_{l_1, l_2}^{s_2} \dots A_{l_{N-1}}^{s_N}$	6
1.2 Decomposition of the Hamiltonian H as a rank- $2N$ tensor to a MPO whose bulk is made of rank-4 tensor.	8
1.3 Construction of the reduced Hamiltonian H_{reduced} by projecting the original H on the basis of $\{ L_{i-1}\rangle S_i\rangle S_{i+1}\rangle R_{i+2}\rangle\}$	9
1.4 Mapping a 2D square lattice to a 1D MPS using the snake path. The leading bipartite entanglement entropy of the ground state is linear to the system width as illustrated by the red cut.	10
1.5 For the Heisenberg model, well-converged spin moment $\langle S_z^{\text{center}} \rangle$ for the center spin as a function of bond dimension m in 6×6 , 8×8 and 10×10 systems, using S_z conservation ($U(1)$ symmetry). The blue dashed line is $\langle S_z^0 \rangle = 0.307$, the known broken symmetry magnetization for an infinite system[1]. At bond dimension 1, DMRG mimics a simple mean field theory, and gives a perfect Néel order parameter of 0.5. At very large bond dimension, DMRG gives the exact result of zero (overall spin singlet) for any finite system with an even number of sites. In between, we see a plateau around the 2D broken symmetry value which sharpens with increasing system size.	14
1.6 Ground states of the S=1/2 Heisenberg antiferromagnetic model on (a) 8×4 , (b) 2×8 , and (c) 4×8 cylinders. The length of the arrow is proportional to the local magnetization $\langle S_i^z \rangle$. There is a staggered pinning field of magnitude $J/2$ applied on both edges. Figure is reproduced from Fig.7 in [2].	17
1.7 Finite-size scaling for the square-lattice Heisenberg AFM using different cylinders with aspect ratio $L_x/L_y = 2$. The $\langle S^z \rangle$ is extracted from the center of the cylinder with staggered pinning field of $0.5J$ on both edges. The finite-size scaling converges to the AFM order in 2D [1] denoted by the dashed line. Figure is reproduced from Ref. [3].	18
1.8 (a) Ground state phase diagram of the anisotropic J_1^Δ - J_3 model (see Chapter 5). (b) A DMRG scan calculation with fixed $\Delta=0$ and varying J_3 , which includes the ferromagnetic (FM), Ising- z (Iz) and zigzag (ZZ) phases.	20

2.1	Approximate phase diagram in the $x - t'$ plane, where x is the doping and t' is the next-nearest neighboring hopping, for width-8 cylinders. The six gray lines indicate the location of parameter-varying “scan” calculations on long cylinders which were the main tool to determine the phase diagram. The green indicates commensurate AFM order; the beige represents conventional stripes, which modulate π -phase shifted domain walls in the AFM order. The slanted lines indicate d -wave pairing order. The simultaneous presence of d -wave pairing and AFM correlations induces weaker momentum- (π, π) p -wave order.	27
2.2	Local properties (left) and a high-probability product state (right) of systems in different phases. The left panels show conventional local measurements for ground states in three different phases. The length of the arrows and the area of the circles represent $\langle S_z \rangle$ and local doping respectively. The spins are colored to indicate different AFM domains. The right panels show particular product states which occurred with maximum probability in a particular search within the corresponding state (see text). (a) and (b): electron low doped phase with $t' = 0.2, x = 0.12$, with simultaneous pairing and AFM order. The highest probability configuration of a pair of holes is diagonal-next-nearest neighbor. (c) and (d): Conventional stripe phase at $t' = 0, x = 0.07$, where half-filled stripes form, and pairing is visible within the stripes, but lacking phase coherence. (e) and (f): W3 striped phase at $t' = -0.2, x = 0.07$, with holes unpaired within the stripes.	29
2.3	A doping-varying scan on a 50×8 cylinder with $t' = 0.2$, appropriate for electron-doped cuprates. Spin, charge are shown in the upper plot in the same way as in Fig. 2.2. The lower plot shows the d -wave singlet pairing with its sign/amplitude indicated by the color/thickness of bonds. The numbers on the middle axis indicate the approximate local doping. No pair field is applied. In the underdoped region ($x \lesssim 0.13$) the system exhibits AFM with strong d -wave pairing. In the overdoped region ($x > 0.13$) stripes are present, with pairing persisting to about $x \approx 0.25 - 0.3$	32
2.4	A doping-varying scan on a 50×8 cylinder with $t' = -0.2$, appropriate for hole-doped cuprates. A staggered magnetic pinning field of 0.03 is applied on the left edge. A global d -wave pair field of 0.005 is applied to measure the pairing response. The system exhibits stripes across the whole doping range shown here with minimal pairing response to the applied pairing field.	33
2.5	A doping-varying scan on a 50×8 cylinder with $t' = 0$. A staggered magnetic pinning field of 0.05 is applied on the both edges. A global d -wave pairfield of 0.005 is applied to measure the pairing response. The system is striped and pairing response peaks near $x = 0.15$, but in non-scan calculation without applied field the system shows no local pairing and the pair-pair correlations die rapidly with separation.	34
2.6	A t' -varying scan on a 42×8 cylinder with doping $x \sim 0.09$. A staggered magnetic pinning field of 0.03 is applied on both edges. No pair field is applied. For $t' > 0$ we see the AFM- $d/\pi p$ phase, while in the region with negative t' we find a conventional stripe phase and pairing is suppressed.	35

2.7	A t' -varying scan on a 40×8 cylinder with doping $x \sim 0.13$. No pair field is applied. A staggered magnetic pinning field of 0.03 is applied on both edges. For $t' > 0$ we see the AFM- $d/\pi p$ phase which becomes striped for smaller t' . In the negative t' region the stripes continue but without pairing.	36
2.8	A t' -varying scan on a 40×8 cylinder with doping $x \sim 0.19$. No pair field is applied. A staggered magnetic pinning field of 0.03 is applied on both edges. There are stripes across the whole system, but pairing only for larger positive t'	36
2.9	The AFM- $d/\pi p$ phase at fixed $t'=0.2$ and $x = 0.12$. (a) and (b) show spin, charge, and d -wave singlet pairing as in previous plots. In (c), we show triplet link pairing, where we find (π, π) p -wave order. For (d), we plot singlet and triplet pairing, as well as the spin expectation value (left-axis scale), for systems which have had a global staggered magnetic field h applied; each value of h is a different simulation. The singlet pairing is nearly independent of h while the triplet pairing and magnetization both increase with h , but the indicated ratio (black crosses, right axis) is nearly constant.	38
2.10	Higher doped positive t' phase with stripes and pairing. The doping is $x = 0.20$ and $t' = 0.2$. (a), (b), and (c) are as in the previous figure. In (c), we see that the p pairing is modulated by the domain walls in the antiferromagnetism. This is apparent in (d), which shows the singlet pairing and the triplet pairing multiplied by -1^{l_x} versus l_x . The singlet pairing has small modulations with peaks at the stripes, while the triplet pairing oscillates with nodes at the stripes.	40
2.11	W3 striped phase on a 32×8 cylinder at $x = 0.08$, $t' = -0.2$. In (a) only the local doping is shown; the local spin measurements are zero. The stripes are strongly associated with single columns. In (b) we show the nearest neighbor spin-spin correlations, which are much stronger in the undoped width-two "ladders". Longer distance spin-spin correlations are measured to decay rapidly. In (c) we show the link hopping, which is very strong along the stripes but also exhibits limited hops onto the ladders. The results together suggest significant decoupling between the chains and ladders.	42
2.12	Energy versus number of particles, from which one can read off various gaps. The overall curvature is the result of using a finite length cylinder (32×6); the orange curve shows a quadratic fit to the points touching it. The chemical potential has been set to make the slope at the midpoint zero. Left: AFM- $d/\pi p$ phase with $t'=0.2$ at $x \sim 0.08$. Middle: conventional striped phase with $t'=0$ at $x \sim 0.08$. Right: W3 striped phase with $t' = -0.2$ at $x \sim 0.07$. Here the W3 stripe runs horizontally on width 6, displayed in Fig. 2.11.	44
2.13	A doping-varying 50×6 cylinder with $t' = 0.2$ which simulates electron-doped cuprates. The numbers on middle axis indicate the averaged local doping. A staggered magnetic pinning field of 0.03 is applied on the left edge. No pair field is applied. At low doping there is AFM order which continuously transition to stripe and then uniform pattern at higher doping.	45

2.14	A doping-varying 50×6 cylinder with $t' = -0.2$ which simulates hole-doped cuprates. A staggered magnetic pinning field of 0.03 is applied on the left edge. A global pair field of 0.005 is applied to measure the pairing response. There's stripe pattern across all doping with pairing suppressed	46
2.15	(a) A conventional striped phase with two holes removed from the third stripe from the left. (b) A W3 phase with the stripes running horizontally in a width-6 cylinder at a doping of $x = 0.083$	47
2.16	A W3 striped phase with a defect.	47
2.17	Upper panel: Experimental phase diagram of a typical cuprate superconductor, following [4], with antiferromagnetic (AFM), charge ordered (CO) and superconducting (SC) phases. The vertical axis is temperature and horizontal axis indicates electron doping (left side) and hole doping (right side). Lower panel: Antiferromagnetic, superconducting and charge-density wave order parameters at zero temperature in the t - t' - J model from DMRG calculations. Solid lines are for width-8 (W8) cylinders and dashed lines are for width-6 (W6) cylinders.	48
2.18	Momentum space occupancy $n(\vec{k})$ for a single spin in the width-8 cylinder. The left figure shows $n(\vec{k})$ for the fermions in the t - t' - J model with $t' = -0.2$ and $n=0.88$ fermions per site. This corresponds to the momentum distribution for the electrons in a hole doped system. The center figure shows the momentum distribution of the fermions in the t - t' - J model with $n=0.88$ fermions per site and $t' = 0.2$. Under a particle-hole transformation, which includes a (π, π) shift of the origin, one obtains the figure on the right. Here $n(\vec{k})$ represents the momentum occupation of the electrons for an electron doped system with $t' = -0.2$ and $n=1.12$ electrons per site.	49
2.19	An approximate phase diagram in the $t' - t''$ plane at doping $x \approx 0.1$. The lines are "scans" with the blue/red color denoting the parameter range with/without pairing. The dotted green line shows the extrapolated pairing phase boundary based on the scans. The light/dark gray regions have AFM order with uniform/nonuniform hole density while the white background is striped. Square [5], diamond [6, 7] and circle [8] markers indicate the (t', t'') values proposed in several studies with solid markers for electron doped systems and hollow markers for hole doped systems.	51
3.1	(a): The three-band Hubbard model and our phase convention for the orbital basis. (b): Charge and spin structure on a 12×5 cylinder at a hole doping ~ 0.15 . The length of the arrows and the diameter of the circles represent $\langle S^z \rangle$ and local doping, respectively. The spins are colored to indicate different AFM domains. There are weak magnetic pinning fields applied on the boundary sites in the dotted boxes. (c): Average orbital-resolved local doping $p_{\text{Cu/O}}$ along the length of the cylinder with $p_{\text{tot}} = p_{\text{Cu}} + 2p_{\text{O}}$ (d) and (e): Pairing order $\langle \Delta_{ij}^\dagger + \Delta_{ij} \rangle$ between neighboring Cu sites i and j . The thickness/color of the bond indicates the magnitude/sign of the pairing. The pairing orders away from the edges are similar for (d) which has pairfields applied on the shaded left edge and (e) which spontaneously breaks symmetry.	56

- 3.2 At a hole doping of 0.15 (a): occupancies of the natural orbitals obtained by diagonalizing the single-particle correlation matrix $M_{\alpha\beta} = \sum_{\sigma} \langle C_{\alpha\sigma}^{\dagger} C_{\beta\sigma} \rangle$, with $C^{\dagger} = \{d^{\dagger}, p_x^{\dagger}, p_y^{\dagger}\}$. The natural orbital states/occupancies correspond to the eigenvectors/eigenvalues of $M_{\alpha\beta}$. The inset is a zoom-in of the region that shows a sharp drop at the second band beyond which occupancies are limited ($< 2\%$). (b) and (c): Cu-centered Wannier functions at two different locations constructed from the natural orbitals of the first band. Color/area of the circles indicate the sign/magnitude of the local orbital component. (e): overlap of Wannier functions (truncated to a 5×5 CuO₂ unit cell) with their centers shifted to the same site, showing they are almost translational invariant. 58
- 3.3 A Cu-centered Wannier function with the color/area of the circles denoting the sign/magnitude of the local orbital components. The coefficients of the orbitals in the lower-right quadrant are shown in the table, which have been averaged over the vertical and horizontal directions. The Wannier function here is from downfolding the case **h1** in the main text. 59
- 3.4 (a),(b) and (c): action of the t_n term, and resulting hopping strengths, depending on the occupations of the sites involved. (d) On a width-4 cylinder, mobility of a pair of holes/electrons (in unit of t) measured by the slope of pair energy versus $1/(L_{\text{eff}} + 1)^2$, for the t - t_n - U model and the t_{eff} - U model. . 64
- 3.5 Pairing response for the t - t_n - U model in a 10×4 cylinder at a hole doping ~ 0.11 ($n \approx 1.11$). Pair-fields have been applied to regions near both edges, denoted by the black boxes, with the phases on the two ends (a) being the same and (b) having a π shift. (c): extrapolation of the energies with the truncation errors for the two different pairfield boundary conditions in (a) and (b). The energy difference is a measurement of the superconducting phase stiffness. (d) Same as (c) for the t_{eff} - U model that incorporates the effect of the t_n term only in mean-field. 65
- 4.1 (a) The naïve h - J_2 phase diagram of model (4.1) based on the single spin-flip and pair-BEC h_{c1} and h_{c2} lines. Lines and symbols show analytical and DMRG results, respectively. (b) The actual phase diagram of the model (4.1) in the zoomed region of (a), with the first-order, multi-pair, and pair-BEC transitions emphasized. (c) The zoomed sector of (b) showing the extent of the nematic phase near pair-BEC field. 69
- 4.2 (a) Magnon energies $\varepsilon_{\mathbf{k}}$ at $h > h_{c2}$ for $J_2 = 0.7$ and 0.4 , schematics of magnon pairing, and gaps $\Delta_{\mathbf{Q}(0)}$. (b) The pairing gap Δ vs J_2 from theory (lines) and DMRG (symbols). (c) $\varepsilon_{\mathbf{k}}$ for $J_2 = 0.7$, nodes of the $d_{x^2-y^2}$ -wave harmonic (white lines), and schematics of the d -wave. (d) The h - J_2 phase diagram of the model (4.1) by DMRG, field h is relative to h_{c2} . Symbols mark the FM (black), nematic (red), and AFM (blue) phases. Phase boundaries are inferred from the midpoints between the data. Cyan circle marks a switch to the pair-attraction and green circle to the first-order transition (solid line). Inset: Schematics of the true h - J_2 phase diagram in Fig. 4.1(b). The nematic region and the deviation from the h_{c2} -line are exaggerated. 70

4.3	DMRG results in the 20×8 cluster for $J_2 = 0.55$ and $h = 0.445$. (a) Ordered moment $\langle S \rangle$ in the xz -plane with pairing field $0.1S_i^- S_{i+y}^-$ (spin-flip field $0.1S_i^-$) at the left (right) edge. (b) Nearest-neighbor component of the pair wave-function; thickness (color) of the bond corresponds to the value (sign) of $\langle S_i^- S_{i+x(y)}^- \rangle$. (c) z -axis magnetization $\langle S_i^z \rangle \approx \langle S \rangle$ (left axis), and nematic $\langle S_i^- S_{i+y}^- \rangle$ and spin-canting $\langle S_i^- \rangle^2$ order parameters (right axis) along the cylinder.	74
4.4	Long-cylinder scan in h from 0.85 to 1.05 for $J_2 = 0.7$, with (a) spin pattern of the ordered moments (field $0.1S_i^-$ at the left edge), and (b) magnetization $\langle S_i^z \rangle$ (left axis), and pair $\langle S_i^- S_{i+y}^- \rangle$ and spin-canting $\langle S_i^- \rangle^2$ order parameters (right axis). (c), (d) and (e) Fixed-parameter calculations as in Fig. 4.3(c) for $h = 0.9, 0.96,$ and 1.0 , respectively.	75
4.5	(a) and (b) Same as (a) and (b) in Fig. 4.4 for $J_2 = 0.45$ and h from 0.0 to 0.2. (c) Same as (b) for h from 0.12 to 0.16.	77
4.6	(a) The total energy of the system with n magnons relative to the magnon pairing energy in a pair per magnon, $\frac{1}{2}\bar{E}_2$, times n vs n in the 16×8 cluster with fixed total S^z for $J_2 = 0.7$ and n from 1 to 10. Red line is the even- n sector and blue line is the odd- n sector. (b) The single-magnon gap $\Delta E(n_{odd})$ vs n	78
4.7	(a) and (b) Schematic plots of the total energy $E(n)$ vs magnon number n without the magnetic field. The slope of the line connecting $E(0)$ and $E(n)$ is the multi-pair BEC instability field h_{cn} . The energy vs magnon number curve is concave (convex) for attractive (repulsive) interaction. (c) The total energy of the system with n magnons $\bar{E}(n)$ relative to the energy of $\frac{n}{2}$ non-interacting pairs $\frac{n}{2}\bar{E}(2)$ for $J_2 = 0.7$ and $J_2 = 0.5$ in a 16×8 cylinder. (d) The h - J_2 phase diagram for the states with fixed number of magnons $n = 2, 4, 6, 8$ in a 16×8 cylinder. For $J_2 > 0.61$, magnon pairs are repulsive and the leading instability is the single-pair-BEC ($n = 2$), while for $J_2 < 0.61$ the magnon pairs are attractive, which leads to the multi-pair instabilities with narrowing J_2 steps that resemble a devil's staircase.	81
4.8	DMRG non-scan results for $J_2 = 0.45$, see Fig. 5 in the main text. (a) The ground state at $h = 0.140$ is a strongly canted AFM state as is indicated by the magnetization $\langle S_i^z \rangle$ (left axis), and by the dipolar, $\langle S_i^- \rangle^2$, and quadrupolar, $\langle S_i^- S_{i+y}^- \rangle$, order parameters (right axis). (b) The $h = 0.143$ state is a fully saturated FM state. We apply small pairing and canting fields on the left and right edges, as is described in the main text.	83
5.1	The classical (a) and quantum (b) phase diagrams of the $XXZ J_1^\Delta$ - J_3 model (5.1) with the ferromagnetic (FM), zigzag (ZZ), spiral (Sp), double-zigzag (dZZ), and Ising- z (Iz) phases. The solid lines are phase boundaries interpolating transition points (diamonds) inferred from the DMRG scans along J_3 (red) and Δ (yellow). The vertical and dashed lines are classical and MAGSWT phase boundaries, respectively. Spins are in-plane for all phases except Iz, see also Fig. 5.2.	88

5.2	Long-cylinder scans of the J_1^Δ - J_3 model (5.1) vs J_3 in the (a) Heisenberg ($\Delta=1$) and (b) XY ($\Delta=0$) limit. The arrows show the local ordered moment $\langle \mathbf{S}_i \rangle$. FM, ZZ, and Iz phases are indicated and transitions are determined as described in text. The honeycomb lattice is in the xy plane while spins shown in the figure are in the xz plane.	91
5.3	(a) Ordered moments in the 16×16 non-scan cluster for $J_3=0.24$, showing dZZ pattern. (b) Energies of the three competing phases vs J_3 , crosses are DMRG results and higher-energy states are metastable. Lines are extrapolated energies, $\langle \psi_i H(J_3) \psi_i \rangle$, where ψ_i are the three states at $J_3=0.24$	92
5.4	Long-cylinder Δ -scans of the J_1^Δ - J_3 model (5.1) for (a) $J_3 = 0.25$ and (b) $J_3=0.4$. Notations are as in Fig. 5.2.	93
5.5	DMRG J_3 -scans for $\Delta=0.5, 0.4$, and 0.3 in the J_1^Δ - J_3 model. The scans for $\Delta=0.5$ and 0.3 are on the 12×32 cylinders while the $\Delta=0.4$ scan is on the 16×40 cylinder.	94
5.6	The quantum $S = \frac{1}{2}$ phase diagrams of the full XXZ J_1^Δ - J_3^Δ model (5.1), c.f. Fig. 5.1(b). See text.	97
5.7	DMRG J_3 -scans in the J_1^Δ - J_3^Δ model for $\Delta=0.5, 0.25$, and 0 on the 12×32 cylinders.	98
5.8	(a) and (b) 12×12 XC cylinder non-scans for $\Delta = 0.4$ and $J_3 = 0.3$ in the J_1^Δ - J_3 model showing: (a) nearly-zero ordered moment and nearest-neighbor $\langle \vec{S}_i \cdot \vec{S}_{i+\delta} \rangle$ (thickness of the bond), and (b) spin-spin correlation $\langle \vec{S}_{i_0} \cdot \vec{S}_j \rangle$, denoted by the length and direction of the arrow, with i_0 site shown by the green oval. The arrow on i_0 is of length 0.25 . (c) Same as (a) on the 16×16 cylinder. (d) Same as (b) on the 8×32 YC cylinder for $\Delta=0.25$ and $J_3=0.32$ in the J_1^Δ - J_3^Δ model. (e) Ordered moment in (d) under the Iz pinning field of 0.5 on both edges. (f) The $1/L_y$ -scaling of the Iz ordered moment in the center of the cylinder with the edge pinning fields from (e) and the XC and YC cylinders having the aspect ratio 2 , which mimics the 2D limit closely—see Ref. [3].	100
5.9	(a) Spin pattern in the 12×12 DMRG cylinder and (b) spin components in the ground state of the generalized XXZ $J_1^{\Delta_1}$ - $J_3^{\Delta_3}$ model from Ref. [9].	101
5.10	The quantum $S = \frac{1}{2}$ phase diagram of the K - J - Γ - Γ' - J_3 model in the J - J_3 plane with fixed $K = -7.567$, $\Gamma = 4.276$, $\Gamma' = 2.362$ (in unit of meV). Phases include ferromagnetism (FM), zigzag (ZZ), out-of-plane antiferromagnetism (z -AFM) and two non-collinear (NCO) out-of-plane counter-rotating spirals with different ordering vectors. The green region is the possible parameter region for α - RuCl_3 constrained by experimental observations including critical in-plane fields denoted by the dotted lines.	103

5.11 In a 12×12 XC cylinder with K, Γ, Γ' fixed as in Fig. 5.10 and $J=-3.0$ meV, $J_3=2.7$ meV, (a) the local ordered moments $\langle \mathbf{S}_i \rangle$ represented by the arrows. Spins in sublattice A and B are in red and blue, respectively. The honeycomb lattice is in the xy plane, and spins are in the yz plane that form an out-of-plane counter-rotating spiral with its \vec{Q} along the x direction. (b) Squared norm of the Fourier transform of S^y for spins in sublattice B, which has a maximum at \vec{Q} that is along the Γ - M direction. (c) Three components of the ordered moments for the spins in sublattice A, averaged over the y direction and plotted along the x direction. (d) S^y of spins in different sublattices averaged over the y direction and plotted along the x direction. Spins in two sublattices that have the same l_x are denoted by green ellipse in (a). For (c) and (d), the cross markers are the data points and lines are fitted sine functions. (e) The ordered moments of spins in the S^y - S^z plane (spins on edges are excluded). The straight arrows from the center point to the ordered moments of the spins in the rounded black rectangle in (a). The curved arrows indicate the rotating orientation of the spins along the propagation direction of the spiral \vec{Q} .

LIST OF TABLES

	Page
3.1 Parameters for the Wannier single-band model from downfolding the three-band model. \mathbf{h} and \mathbf{e} correspond to hole and electron doping of 0.15. t_{pd} is nominally 1.5eV.	62

ACKNOWLEDGMENTS

Reflecting on this unforgettable journey of PhD studies, first and foremost I would like to express my profound gratitude towards my advisor, Steve White. Steve's insights into physics and simulations have been vastly inspiring throughout my graduate career, and set a role model for how a computational physicist should approach problems. I am also exceedingly thankful to Steve for offering exceptional support and flexibility in research, which enables me to explore my own interests and establish collaborations across a variety of topics. I cannot imagine attaining my current status as an independent researcher in physics without Steve's inspiration, guidance and support.

I am indebted to my long-time collaborators and mentors, Doug Scalapino and Sasha Chernyshev, from whom I have learned an abundance of physics and beyond. Doug's dedication to the problem of high temperature superconductivity has largely inspired me, and I can hardly quantify how much I have gained from daily conversation with Sasha. They have supported me through the ups and downs in my graduate studies with their kind mentorship and advice. Undoubtedly, their roles in my PhD studies have ascended to the equivalent of co-advisors.

I would also like to extend my gratitude to my collaborators: Judit Romhányi, Mike Zhitomirsky, Marius Möller, Zheting Jin, Sohrab Ismail-Beigi, Thomas Scaffidi, Rafael Magaldi, Zhiyu Dong and César Gallegos. I have acquired a plethora of knowledge from each of these fabulous and fruitful collaborations.

My office life has been enriched by a great extent because of the daily interactions with the office mates I have had: Marius Möller, Jielun (Chris) Chen and César Gallegos. I also enjoyed the time spent with my group members: Mingru, Randy, Yifan, Yiheng, Rafael, Max and Cody, as well as with friends from other condensed matter groups and the physics department: Pavel, Steven, Matt, Hana, David, Omid, Amin, Davis, Wenhao and Wenlu.

This PhD journey could not have started without all the teachers and professors who taught me physics at different stages in my life. I am especially thankful to my undergraduate advisor, Wei Ku, who guided me with a hands-on approach into the field of condensed matter theory, a career that I did not envision but now I deeply enjoy and cherish. I appreciate the undergraduate training I received in his group that paved the way for a smooth start in my PhD career.

Finally, I wish to convey my wholehearted gratitude to my parents for their unwavering support to my academic pursuit over the many years. I am grateful to my father for nourishing my interest in physics and science from my childhood. During my PhD, it has always been a pleasure to visit my cousin's place in Los Angeles, which created many unforgettable memories for my stay in southern California.

The text of this dissertation contains reprints of the materials as they appear in Refs. [10–14], used with permissions from the National Academy of Sciences and the American Physical Society.

I acknowledge the support from the National Science Foundation under grant no. DMR-2110041.

VITA

Shengtao Jiang

EDUCATION

Doctor of Philosophy in Physics
University of California, Irvine

2024
Irvine, CA, USA

Bachelor of Science in Physics
Shanghai Jiao Tong University

2017
Shanghai, China

RESEARCH EXPERIENCE

Graduate Research Assistant
University of California, Irvine

2019–2024
Irvine, CA, USA

Undergraduate Research Assistant
Shanghai Jiao Tong University

2016–2018
Shanghai, China

TEACHING EXPERIENCE

Teaching Assistant
University of California, Irvine

2018–2019
Irvine, CA, USA

REFEREED JOURNAL PUBLICATIONS

- Quantum phases in the honeycomb-lattice J_1 - J_3 ferro-antiferromagnetic model** **2023**
S. Jiang, S. R. White and A. L. Chernyshev, Phys. Rev. B **108**, L180406
- Density-matrix-renormalization-group-based downfolding of the three-band Hubbard model: the importance of density-assisted hopping** **2023**
S. Jiang, D. J. Scalapino and S. R. White, Phys. Rev. B **108**, L161111
- Where is the Quantum Spin Nematic?** **2023**
S. Jiang, J. Romhányi, S. R. White, M. E. Zhitomirsky and A. L. Chernyshev, Phys. Rev. Lett. **130**, 116701
- Pairing properties of the t - t' - t'' - J model** **2022**
S. Jiang, D. J. Scalapino and S. R. White, Phys. Rev. B **106**, 174507
- Ground-state phase diagram of the t - t' - J model** **2021**
S. Jiang, D. J. Scalapino and S. R. White, Proc. Natl. Acad. Sci. U.S.A., **118** (44) e2109978118
- Non-Fermi liquid scattering against an emergent Bose liquid: manifestations in the kink and other exotic quasiparticle behaviors in the normal-state cuprate superconductors** **2019**
S. Jiang, L. Zou and W. Ku, Phys. Rev. B **99**, 104507

ABSTRACT OF THE DISSERTATION

Density-Matrix Renormalization Group and Model Reduction Studies of Two-Dimensional Doped and Frustrated Systems

By

Shengtao Jiang

Doctor of Philosophy in Physics

University of California, Irvine, 2024

Professor Steven R. White, Chair

The density-matrix renormalization group (DMRG) invented by Steven R. White is a variational algorithm to search for the ground states of quantum many-body systems. Using the entanglement entropy as its organizing principle, DMRG stands as one of the most powerful methods in simulating two-dimensional (2D) quantum systems, and is especially useful for investigating strongly correlated systems that are otherwise challenging for analytical approaches. This thesis presents the applications and developments of DMRG and related tensor network methods in studying a variety of 2D doped and frustrated systems as well as their model reductions. Chapter 1 lays out the fundamentals of DMRG and tensor network states, along with multiple techniques for studying 2D systems. Chapter 2 presents our DMRG studies of the ground state phase diagram of the extended t - J models. We found that while the models are consistent with the cuprates in antiferromagnetism and charge order, superconductivity nevertheless appears absent or marginal in hole-doped systems. Motivated by this discrepancy between the models and the cuprates, in Chapter 3 we carried out a DMRG-based downfolding of the parental three-band Hubbard model, seeking possible fixes to the previously studied single-band models. An effective model was derived via Wannier construction, which includes novel density-assisted hopping terms that appear to be important in enhancing hole-doped superconductivity. In Chapter 4, we examined the quantum

spin nematic phase in the paradigmatic $S = 1/2$ square-lattice J_1 - J_2 ferro-antiferromagnetic Heisenberg model, employing a combination of DMRG and analytics. Our findings revealed that many-body effects induce significant contraction of the nematic phase compared to the naïve expectation. Chapter 5 presents a study of the anisotropic J_1^Δ - J_3 model on the honeycomb lattice, which is believed to be the fundamental model for many Kitaev material candidates upon adding bond-dependent terms. This chapter also includes my contribution to a study of the generalized Kitaev- J_3 model for α - RuCl_3 .

Chapter 1

Introduction

1.1 Simulating strongly correlated many-electron problems

Strong interaction among electrons can lead to a plethora of novel emergent phenomena that are fundamentally different from the behaviors of individual particles. The most prominent example is perhaps the high temperature superconductivity in the cuprates, which has not been fully resolved thirty years after its discovery [15, 16]. Another related area is frustrated magnetism [17], where strong interaction between electrons results in effective frustrated spin exchanges, and the quantum fluctuation induced thereof gives rise to exotic phases such as the quantum spin liquid [18]. Other celebrated cases of strong correlation include the fractional quantum hall effect [19] and the recently discovered twisted bilayer graphene [20].

The richness of the phenomena is intrinsically associated with the buildup of entanglement among electrons due to strong interactions, which alters its behavior from the weak coupling picture of individual quasiparticles. On the other hand, entanglement also complicates the

representations of wavefunctions. This poses a challenge to analytical approaches, and increases the importance of numerical simulations to provide unbiased pictures of the strongly correlated physics.

In the 1980s and early 1990s, much of the best numerical work on strongly correlated systems utilized exact diagonalization or quantum Monte Carlo [21–23]. Exact diagonalization (ED) seeks to determine the state vector within the entirety of the Hilbert space. Although the computational cost of ED inevitably involves exponential scaling relative to the system size, it imposes almost no restrictions on the form of Hamiltonian. Usually only the ground state or the low-energy spectrum is of interest, and thus iterative algorithms such as the Lanczos algorithm [24] are most useful. The Lanczos algorithm solves the eigenvalue problem iteratively within the Krylov subspace that is generated by the Hamiltonian and an initial guess. Its accuracy improves as the Krylov subspace enlarges. As an example, state-of-the-art ED is able to simulate the low-energy spectrum of a frustrated Heisenberg model on a triangular cluster of $N = 48$ sites [25]. Quantum Monte Carlo is also numerically exact and features only polynomial scaling with respect to the system size, if only the notorious sign problem is absent. The sign problem occurs when the integral has positive and negative parts largely cancelling each other, which prohibits its efficient evaluation through Monte Carlo sampling. This happens in doped fermionic systems at low temperature as well as in many frustrated spin systems. It is important to note that the sign problem is **NP-hard** [26] and can not be circumvented for some types of problems¹.

In the early 1990s, Steven White invented the density-matrix renormalization group (DMRG) as a variational algorithm for finding ground states of quantum many-body systems [29]. Using entanglement as the organizing principle, DMRG effectively reduces the computational cost by one dimension compared to exact diagonalization, i.e., the cost scales linearly

¹There are techniques to mitigate the sign problem such as the constrained-path auxiliary field Quantum Monte Carlo. However one needs to ensure that the constraint imposed is unbiased, which often requires a benchmark from other methods. See Ref. [27, 28] for related studies.

with the system size for one-dimensional (1D) systems and scales exponentially only to the width of 2D systems. It is also free of the sign problem. Because of these exceptional advantages, DMRG has demonstrated unparalleled computational power for 1D problems, and also stands as one of the most powerful methods in simulating 2D systems [2]. The key to the success of DMRG is that the ground states of local Hamiltonians are subject to the “area-law” for entanglement entropy [30] and are only moderately entangled. Therefore, it is highly efficient to search for these ground states using DMRG in the tensor network framework.

The remaining of this chapter is organized as follows: Sec. 1.2 provides a historical overview of the development of DMRG and tensor network methods. Sec. 1.3 introduces the concept of entanglement entropy and the way to represent a quantum many-body wavefunction with Matrix Product State (MPS). Sec. 1.4 lays out the basics of the DMRG algorithm. Sec. 1.5 introduces the fundamentals of studying 2D systems with DMRG. In Sec. 1.6 we argue that DMRG spontaneously breaks symmetry in a way that mimics the 2D systems, and the method to obtain 2D order parameter using finite-size scaling with edge pinning field is described in Sec. 1.7. Finally, Sec. 2.4 presents the DMRG scan calculations as an efficient way to obtain the ground phase diagram.

1.2 Historical development of DMRG and tensor network states

The density-matrix renormalization group was invented by Steven R. White at UC Irvine in 1992 [29] as a variational algorithm to find the ground states of quantum many-body systems. DMRG surpasses the limitations of Wilson’s numerical renormalization group [31] by taking the environment into account and truncating the system’s degrees of freedom

according to its reduced density matrix in the renormalization group process. Its power was first demonstrated by solving the ground state of the 1D Heisenberg chain to unprecedented precision [29].

After the invention of DMRG, people began to realize the connection of the algorithm to tensor network states (TNS) [32]. The concept of TNS was initially employed in classical systems [33, 34]. The precursor of the application of TNS in quantum systems emerged in the context of numerical renormalization group for the Kondo problem [31, 35]². It was not until the 1990s that TNS began to be recognized as an efficient representation of quantum many-body wavefunctions, partially propelled by the invention of DMRG [36]. The essence of TNS is to organize and compress wavefunctions based on the entanglement entropy, and DMRG can be viewed as a variational algorithm to optimize a specific type of TNS called a Matrix Product State [37]. From this point of view, it becomes evident that the DMRG’s success lies in the fact that the ground states of local Hamiltonians only have a limited entanglement that obeys the “area-law” for entanglement entropy [30, 32, 38, 39]. Consequently, these wavefunctions can be efficiently represented and optimized using TNS and alleviates the exponential computational cost of general quantum problems.

It is worth mentioning that there have been development of tensor-network methods in several other directions beyond DMRG, such as time evolution [40–42] and finite temperature [43–45] algorithms, as well as other types of tensor network ansatz including projected entangled pair states (PEPS) for 2D systems [46] and multi-scale entanglement renormalization ansatz (MERA) for critical systems [47].

²In this case, the derivation of the wavefunction when enlarging the system size in the renormalization group process resembles a Matrix Product State.

1.3 Entanglement entropy and matrix product state representation of quantum many-body wavefunctions

Entanglement entropy is a measure of the degree of entanglement in a quantum system. A commonly used one is the Von Neumann entanglement entropy, which quantifies the level of entanglement between the two subsystems partitioned from an entire quantum system. Specifically, for a system divided into parts A and B , its wavefunction $|\psi\rangle$ can be written in the following way using the Schmidt decomposition:

$$|\psi\rangle = \sum_{i=1}^m c_i |u_i\rangle_A \otimes |v_i\rangle_B, \quad (1.1)$$

where $|u_i\rangle_A$ and $|v_i\rangle_B$ are orthonormal states defined on subsystem A and B , respectively. The Von Neumann entanglement entropy S in this case is defined as:

$$S(A|B) = - \sum_{i=1}^m c_i^2 \ln(c_i^2). \quad (1.2)$$

Another equivalent way to calculate the Von Neumann entanglement entropy is through the reduced density matrix of the subsystem A computed by tracing out the other subsystem B :

$$\rho(A) = \text{Tr}_B |\psi\rangle\langle\psi|. \quad (1.3)$$

$\rho(A)$ can be expressed by its eigenvalues c_i and corresponding eigenvectors $|u_i\rangle$:

$$\rho(A) = \sum_{i=1}^m c_i^2 |u_i\rangle\langle u_i|, \quad (1.4)$$

which are essentially the same c_i and $|u_i\rangle$ as in Eq. 1.1. The the Von Neumann entanglement entropy is calculated using the same equation Eq. 1.2.

It becomes evident that if A and B are unentangled, then $|\psi\rangle$ is merely a product state of $|u_1\rangle_A$ and $|v_1\rangle_B$, in which case the entanglement entropy is zero. (Note that $|u_1\rangle_A$ and $|v_1\rangle_B$ themselves can be entangled and are not necessarily product states). Entanglement entropy lies at the core of tensor network states, as will be exemplified below in the MPS representation of wavefunctions.

Any quantum many-body wavefunction $|\psi\rangle$ on a lattice of N sites can be expressed as a superposition of basis states made from a tensor product over the local basis,

$$|\psi\rangle = \sum_{s_1, s_2, \dots, s_N} \psi_{s_1, s_2, \dots, s_N} |s_1\rangle |s_2\rangle \dots |s_N\rangle, \quad (1.5)$$

where $|s_i\rangle$ denotes the local basis states, e.g., $|s_i\rangle \in \{|\uparrow\rangle, |\downarrow\rangle\}$ for a spin-1/2 system. The wavefunction $\psi_{s_1, s_2, \dots, s_N}$ can be regarded as a rank- N tensor with a graphical representation shown in the left part of Fig. 1.1:

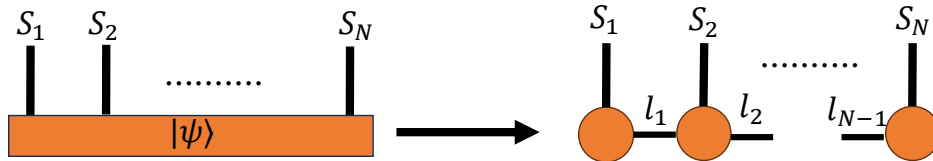


Figure 1.1: Decomposition of a rank- N tensor $\psi_{s_1, s_2, \dots, s_N}$ that represents a wavefunction into a MPS made of $N-2$ rank-3 tensors in the bulk and two rank-2 tensors on the edges:

$$\psi_{s_1, s_2, \dots, s_N} = \sum_{l_1, l_2, \dots, l_{N-1}} A_{l_1}^{s_1} A_{l_1, l_2}^{s_2} \dots A_{l_{N-1}}^{s_N}.$$

The MPS representation decomposes the rank- N tensor into a network made of $N-2$ rank-3 tensors in the bulk and two rank-2 tensors on the edges, with the internal indices to be

contracted over, as shown in Fig. 1.1:

$$\psi_{s_1, s_2, \dots, s_N} = \sum_{l_1, l_2, \dots, l_n} A_{l_1}^{s_1} A_{l_1, l_2}^{s_2} \dots A_{l_{N-1}}^{s_N}, \quad (1.6)$$

The biggest dimension of the internal indices $l_1, l_2 \dots l_{N-1}$ is called the bond dimension of the MPS and denoted by m . Usually a more entangled wavefunction requires a larger bond dimension for its MPS representation, and any wavefunction can be accurately represented given large enough m .

As has been mentioned before, “area-law” for the entanglement entropy states that for the ground states of local Hamiltonians, the leading term in the Von Neumann entanglement entropy is proportional to the area of the boundary between the two partitions [30, 46]. Therefore for gapped 1D systems, where the gap eliminates any log corrections, the entanglement entropy is a constant, implying a constant bond dimension m for its MPS representation, if smaller correction terms are ignored. As a result, MPS facilitates a significant reduction in the data storage of the ground states, from exponential scaling in system size $O(d^N)$ (d is the local degrees of freedom) to a polynomial scaling $O(Ndm^2)$.

1.4 Formulating the DMRG algorithm using matrix product states

While the original formulation of DMRG did not discuss matrix product states, it was later pointed out by Ostlund and Rommer [37] that the wavefunction implicitly used by DMRG is an MPS. It is more straightforward to formulate DMRG using MPS [48]. Later, McCulloch introduced matrix product operators (MPOs) [49], which generalize MPS to operators such

as the Hamiltonian. The MPS-MPO formulation of DMRG is more straightforward than the original formulation.

The MPO representation of the Hamiltonian is

$$H_{s_1, s_2, \dots, s_N}^{s'_1, s'_2, \dots, s'_N} = \sum_{l_1, l_2, \dots, l_n} B_{l_1}^{s_1, s'_1} B_{l_1, l_2}^{s_2, s'_2} \dots B_{l_{N-1}}^{s_N, s'_N}, \quad (1.7)$$

as shown in the following diagram:

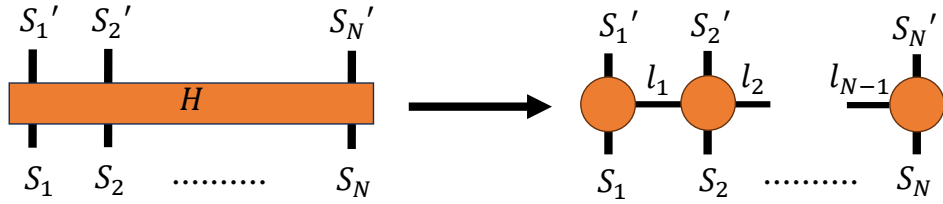


Figure 1.2: Decomposition of the Hamiltonian H as a rank- $2N$ tensor to a MPO whose bulk is made of rank-4 tensor.

The MPO representation of Hamiltonians for 1D systems with only local interactions has a very small bond dimension which does not depend on length.

The goal of DMRG is to optimize the individual tensors in the MPS $|\psi\rangle$ to reach the lowest variational energy $\langle\psi|H|\psi\rangle$. Despite being in the compressed tensor network form, it remains costly trying to optimize all the tensors simultaneously. Instead, DMRG optimizes two neighboring tensor at a time while holding all the other tensors fixed, which is equivalent to solving the ground state problem in a reduced basis. For example as shown in Fig. 1.3, when optimizing the tensors i and $i+1$, one forms the reduced basis of $\{|L_{i-1}\rangle|S_i\rangle|S_{i+1}\rangle|R_{i+2}\rangle\}$. $|S_i\rangle$ and $|S_{i+1}\rangle$ include the full local degrees of freedom, while the “left (right)” $|L_{i-1}\rangle$ ($|R_{i+2}\rangle$) are states previously kept in the MPS that are projected from the Hilbert space corresponding to sites 1 to $i-1$ ($i+2$ to N). The reduced Hamiltonian H_{reduced} is formed by projecting the original Hamiltonian H onto this reduced basis. In the tensor network language, this corresponds to contracting the MPO H with the MPS $|\psi\rangle$ on both sides but leaving out

the two tensors to be optimized. After that, exact diagonalization such as the Lanczos algorithm is used to obtain the eigenvector with the lowest eigenvalue of H_{reduced} . The eigenvector is reshaped into a rank-four tensor, then split and truncated into two rank-three tensors through singular-value decomposition, which subsequently updates updates the MPS. DMRG proceeds to optimize the subsequent two tensors, sweeping through the MPS back and forth (“DMRG sweep”) until convergence is achieved.

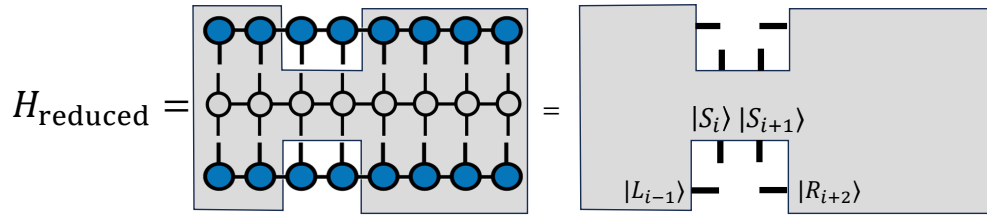


Figure 1.3: Construction of the reduced Hamiltonian H_{reduced} by projecting the original H on the basis of $\{|L_{i-1}\rangle|S_i\rangle|S_{i+1}\rangle|R_{i+2}\rangle\}$.

The cost of DMRG scales as $o(Nm^3)$, where N is the system size and m is the bond dimension of the MPS. Therefore, the efficiency of DMRG largely depends the m required to accurately represent the ground state wavefunction. Several factors can help reach the convergence of DMRG calculations. If the Hamiltonian possesses certain symmetry such as particle number conservation, then quantum numbers (QN) can be implemented in DMRG, which turns the tensors into a sparse block-diagonal form, substantially accelerating the computation. In some cases, one may also choose not to use quantum numbers in order to target spontaneously symmetry-breaking states, the details of which will be discussed later in Sec. 1.6. Typically the initial state can be set as a classical or meanfield solution of the Hamiltonian, such as the Néel state for the Heisenberg antiferromagnet or a Hartree-Fock state for the Hubbard model. For a Néel state, the initial state is a product state, corresponding to bond dimension 1. A Hartree-Fock state is only a product state in momentum space, so its real-space representation may require a significant bond dimension. If QNs are used, one needs to ensure the initial state lies in the desired QN sector. This also provides a convenient way to compute ground states as well as excited states that have definite QNs. The accuracy

of DMRG calculations improves upon increasing the number of states m kept. It is more efficient to increase m in a gradual fashion, since DMRG sweeps at small m are capable of directing the state into the right direction without large computational cost. The risks of getting stuck in metastable states—a key issue in 2D calculations—can be alleviated in many ways, including comparing calculations with different initial conditions, applying external fields and performing DMRG scans. The details of these methods will be discussed in the following sections.

1.5 Studying two-dimensional systems with DMRG

The DMRG algorithm is most natural for 1D problems, not just because of the structure of the algorithm that sweeps through the 1D MPS, but more importantly, because 1D ground state only has a constant or nearly constant bond dimension. As will be discussed below, although DMRG encounters more challenges in 2D, other algorithms also face various limitations. Therefore, DMRG has become one of the most powerful approaches for simulating 2D quantum systems.

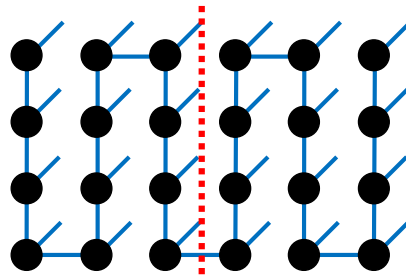


Figure 1.4: Mapping a 2D square lattice to a 1D MPS using the snake path. The leading bipartite entanglement entropy of the ground state is linear to the system width as illustrated by the red cut.

The first step for 2D DMRG is to map the 2D system onto a 1D MPS path. A common approach is to use the “snake path” as shown in Fig. 1.4. Because of the area-law for entanglement entropy [30], the bipartite entanglement entropy of the ground state is no

longer a constant, instead it scales linearly with the width of the 2D system (potentially with logarithmic corrections [46]). As a result, the bond dimension required to approximate the ground state scales exponentially with the system width. On the other hand, the constant scaling of the required bond dimension with respect to the length of the system is retained, similar to the 1D case. Such geometrical dependence of the entanglement entropy motivates the usage of cylindrical or rectangular clusters with the width longer than the length in 2D DMRG.

While this exponential scaling with the system width is indeed a limitation, other methods also face similar or even more severe challenges in 2D. Exact diagonalization scales exponentially with the total number of sites, not just the width in DMRG. Sign problems still exist for many systems of interest when using Quantum Monte Carlo. Recent advancements in 2D tensor network methods, most notably the projected entangled pair state (PEPS) [46], in principle allow for the representation of ground states with a constant bond dimension D typically around 10. However, its optimization is more complicated compared to DMRG. The computational cost has a somewhat large exponent on D ranging from D^7 [50] to D^{12} [2] depending on the network and algorithm used ³, as opposed to the m^3 scaling in DMRG.

Over the past decade, DMRG has been applied to studying a variety of 2D systems, yielding many significant results. One of the most active areas is simulating strongly correlated electronic systems such as the doped Hubbard model or the t - J model, which unveils a delicate interplay of charge order, magnetic order and superconductivity. More details will be presented in Chapter. 2. Another area where DMRG has been extensively used is frustrated magnets that potentially host exotic phases such as the quantum spin liquid [18, 53]. A celebrated example is the discovery of the spin liquid ground state for the nearest-neighbor Heisenberg model on the Kagome lattice [54–56]. Other notable systems include the J_1 - J_2

³For example, the isometric tensor network [50] has a relatively small D^7 scaling, but the isometric constraint may limit its expressiveness and additional errors can occur when gauging the network. There are other methods with smaller exponent, such as D^5 for the simple update introduced in Ref. [51] and D^6 by combining Monte Carlo sampling [52], with extra check on convergence needed.

model on the square lattice [57–59] and triangular lattice [60, 61], as well as more generalized models with real material correspondences [62–64].

When carrying out 2D DMRG, many useful techniques can be employed to ensure convergence and to mitigate finite size effects. A comprehensive review of these techniques are laid out in Ref. [2]. In the following sections, several concepts and methods that are frequently invoked throughout this thesis will be presented.

1.6 Spontaneously broken symmetry in DMRG calculations

In the limit of a bond dimension of $m = 1$, a MPS is a simple product state, and DMRG represents a simple sort of mean field theory. The resulting state breaks symmetry, like mean-field techniques in general. As the bond dimension increases, the MPS approaches the result of an exact diagonalization. Thus it is useful to think of DMRG as interpolating in some sense between mean field theory and exact diagonalization. In 1D systems, one is often very close to the exact diagonalization side of this, so one can usually ignore questions of broken symmetry. For 2D systems, it is important to be aware of how DMRG may or may not break symmetries.

How DMRG can break symmetry depends on what quantities are conserved in the calculation. Consider the antiferromagnetic Heisenberg model on a square lattice. Say we use $U(1)$ symmetry, i.e. we conserve total S^z . To get the ground state, we choose the $S^z = 0$ sector, and for $m = 1$, DMRG gives one of the two Néel states oriented in the spin z direction. A Néel state oriented in another direction does not have definite S^z . Now suppose we increase m , but not too much. The system then tries to reduce the energy subject to having low

entanglement, since m controls the entanglement that can be captured when one splits the system in two.

The easiest way to decrease the energy is to build in local spin fluctuations, but to stay close to one Néel state. Any superposition of Néel states would produce larger entanglement with little benefit in energy. These effects increase with system size. Thus, a $U(1)$ DMRG calculation will show a broken spin orientation symmetry along the z direction. As one increases m , at first the local spin fluctuations become better and better, and one may approach a plateau near $|\langle S_0^z \rangle|$ or $\tilde{M} \approx 0.307$, where M is the bulk magnetization. The accuracy of this plateau depends on system size. As one increases m farther, eventually the energy optimization notices that different directions of the order can be mixed, and one tends to $\langle S_i^z \rangle \rightarrow 0$, the exact diagonalization result for an even number of sites, satisfying the Lieb-Mattis theorem.[65]. Figure 1.5 shows $\langle S_z^{\text{center}} \rangle$ at a center site for 6x6, 8x8 and 10x10 clusters as a function of the number of states (or bond dimension m). One can see that $\langle S_z^{\text{center}} \rangle$ has a plateau around $\langle S_z^0 \rangle$ before approaching the exact solution of a spin-singlet. The bond dimension required to form the overall spin-singlet increases rapidly with the width of the system.

If one does not use $U(1)$ symmetry, the system could form a Néel state in any direction. Using $U(1)$ speeds up the calculation considerably, so we avoid leaving it out except in special cases, such as applying a spin-twist boundary condition. Some DMRG programs conserve $SU(2)$, but not ITensor, the library used here. In an $SU(2)$ calculation, the ground state calculation is constrained to the singlet sector and it cannot break spin symmetry. Keeping $SU(2)$ means that one keeps more states for the same computational cost, but this is offset to a varying extent, in terms of how low the energy is, by having to construct a superposition of Néel states. Thus either $SU(2)$ or $U(1)$ calculations are more effective depending on what one is studying.

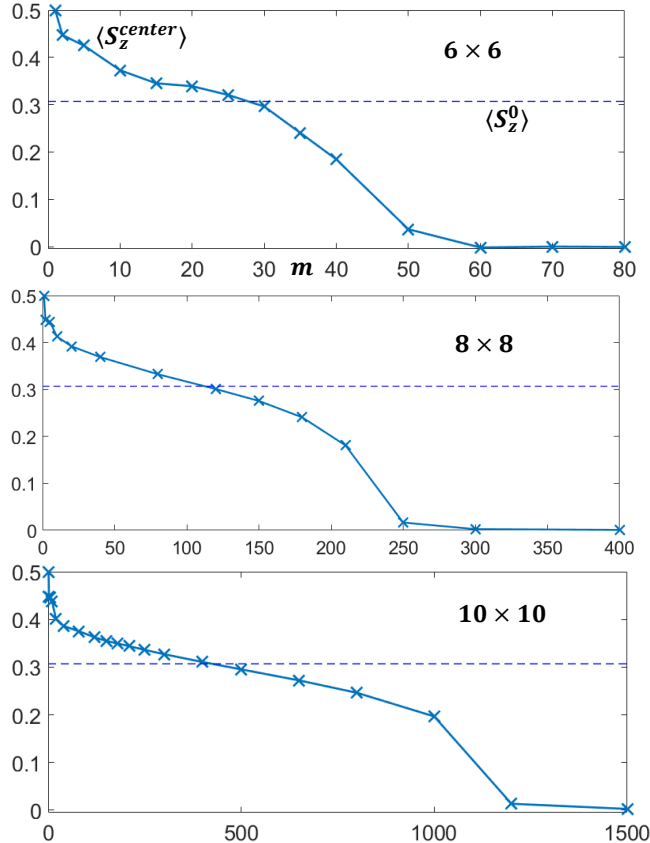


Figure 1.5: For the Heisenberg model, well-converged spin moment $\langle S_z^{center} \rangle$ for the center spin as a function of bond dimension m in 6×6 , 8×8 and 10×10 systems, using S_z conservation ($U(1)$ symmetry). The blue dashed line is $\langle S_z^0 \rangle = 0.307$, the known broken symmetry magnetization for an infinite system[1]. At bond dimension 1, DMRG mimics a simple mean field theory, and gives a perfect Néel order parameter of 0.5. At very large bond dimension, DMRG gives the exact result of zero (overall spin singlet) for any finite system with an even number of sites. In between, we see a plateau around the 2D broken symmetry value which sharpens with increasing system size.

If symmetry is not broken, then determining the order parameter requires measuring a correlation function. Correlation functions tend to converge slowly with the bond dimension in DMRG, compared to local quantities. Correlation functions also produce the square of the order parameter, which, if the order parameter is small, causes further inaccuracy. It can be much more effective to measure order parameters by strongly pinning the edges of a cylinder and measuring the local order parameter in the center[3]. This can be very accurate if one adjust the aspect ratio of the cylinder to cancel leading finite size effects[3]. However,

if one is not trying for a quantitative determination of the 2D order parameter, one gets good results from measuring the local order due to the self-pinning of limited symmetry DMRG.

For a potentially superconducting system, one may or may not conserve the number of fermions modulo 2. One cannot turn off the number conservation completely, since this breaks the fermion parity and interferes with putting in the right statistics. We refer to these two choices as conserving or not conserving particle number. If the system is superconducting, a mean field theory such as BCS would break symmetry to give a definite phase, making a superposition of different numbers of particles. If one conserves particle number, one cannot have a definite phase. In this case, in order to measure pairing, one would have to use correlation functions. Since the order parameters tend to be small, measuring its square with DMRG is inaccurate, both because of the small quantity being measured and the inaccuracy of correlation functions. If one turns off number conservation, then one can have a phase. However, usually, for efficiency, we use only real wavefunctions. In this case the allowed broken symmetry reduces from $U(1)$ (the phase) to Z_2 (+ or -). The advantages associated with measuring local quantities rather than correlation functions makes the non-particle-conserving approach highly preferred. Indeed, recently it has been reported that turning off particle number conservation is more efficient in probing d -wave superconductivity [66].

In contrast to the magnetic case, a system which is superconducting may not break number symmetry at low bond dimension, particularly if the pairing is relatively weak. The system may get stuck in a particle-conserving state, even if non-particle conserving states are allowed and are lower in energy for a fixed bond dimension. However, one can turn on a pairing/proximity-effect field $\Delta + \Delta^\dagger$ for a few sweeps to get it unstuck, and then see if the local pairing grows in subsequent sweeps, approaching an approximate plateau. Alternatively, one can apply pairing fields on the edges and measure the response in the center. If the

pairing is quite strong, then one is very likely to see a robust spontaneous broken-symmetry pairing without applying any temporary or edge fields.

1.7 Finite-size scaling of local order parameters

Since 2D systems tend to spontaneously break symmetry, an important goal for 2D DMRG is to obtain the 2D order parameter with a systematic finite-size scaling. While the spontaneous symmetry breaking described in the previous section provides a convenient estimation, a more precise way is through applying strong pinning fields on the edges of the clusters [3]. Using cylinders of different sizes with an appropriate aspect ratio, the order parameter in the center provides an excellent agreement with the 2D order parameter after $1/L_y$ scaling. This section provides a brief overview of this method described in Ref. [3].

The application of edge pinning fields mimics the spontaneous symmetry breaking in 2D. One can imagine embedding the finite cylinder in a 2D system with a finite order. In this scenario, interactions between the cylinder edges and the surrounding environment act as effective pinning fields on the edges. It is often useful to apply strong pinning fields. For example, in the case of square-lattice Heisenberg antiferromagnet, the magnitude of the pinning field is chosen to be $0.5J$, equivalent to interacting with classical AFM spins. Further increasing the pinning fields has saturating effect since they only affect the edges.

The importance of choosing an appropriate aspect ratio for the finite size scaling is demonstrated in Fig 1.6, using square-lattice Heisenberg antiferromagnet as an example. The ordered moment can be overestimated if the aspect ratio (length over width) is too small as in Fig. 1.6(a), in which case the proximity to the strong pinning fields leads to excessive effects. On the other hand, if the aspect ratio is too big as in Fig. 1.6(b), the system becomes quasi-1D and the central spins hardly feel the symmetry-breaking field. The appropriate

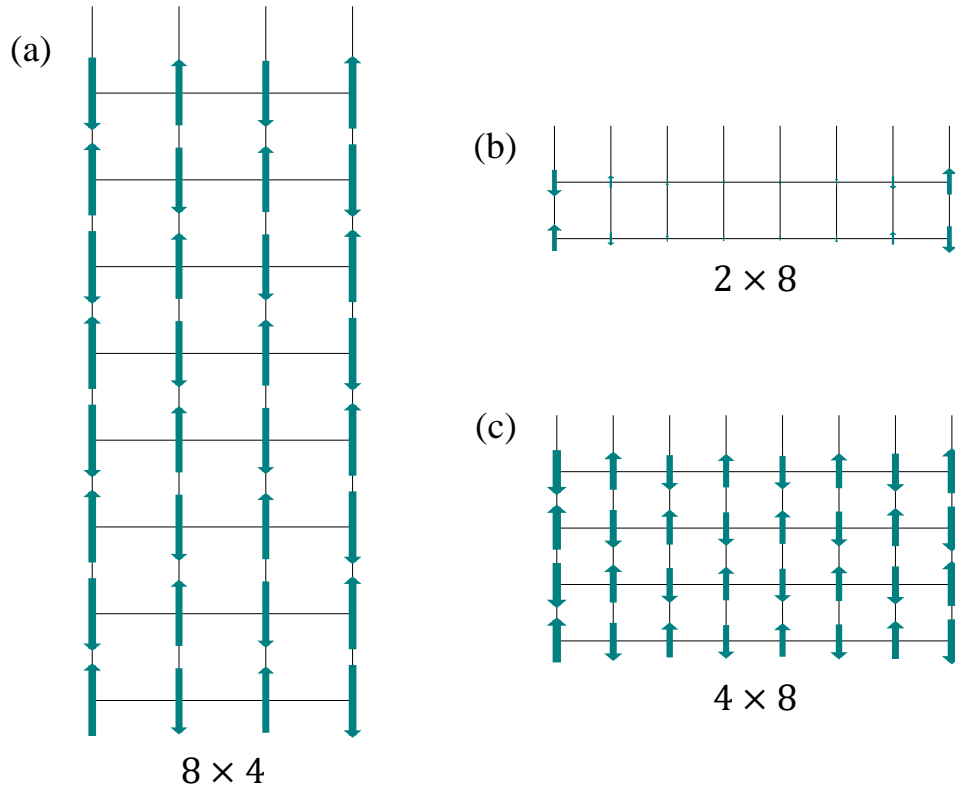


Figure 1.6: Ground states of the $S=1/2$ Heisenberg antiferromagnetic model on (a) 8×4 , (b) 2×8 , and (c) 4×8 cylinders. The length of the arrow is proportional to the local magnetization $\langle S_i^z \rangle$. There is a staggered pinning field of magnitude $J/2$ applied on both edges. Figure is reproduced from Fig.7 in [2].

aspect ratio in this case is around 2 as shown in Fig. 1.6(c), where the ordered moment in the center $\langle S^z \rangle \approx 0.28$ is already close to the actual 2D value of 0.307 [1] even without $1/L_y$ finite-size scaling. While the optimal aspect ratio depends on the specific model, setting it to two usually yields a reasonable estimation.

After choosing the appropriate aspect ratio, one can proceed with finite-size scaling by extrapolating the order in the center of the cylinder with $1/L_y$. This is shown below in Fig. 1.7. In this aspect ratio of $L_x/L_y = 2$, the ordered moment approach the 2D value from below in a slightly curved line. The optimal aspect ratio according to spin-wave theory is 1.67 [3]. Indeed, using aspect ratio of 1.5 provides a better extrapolation with an almost flat curve, i.e., the ordered moment is already very close to 2D value on small cylinders. One can

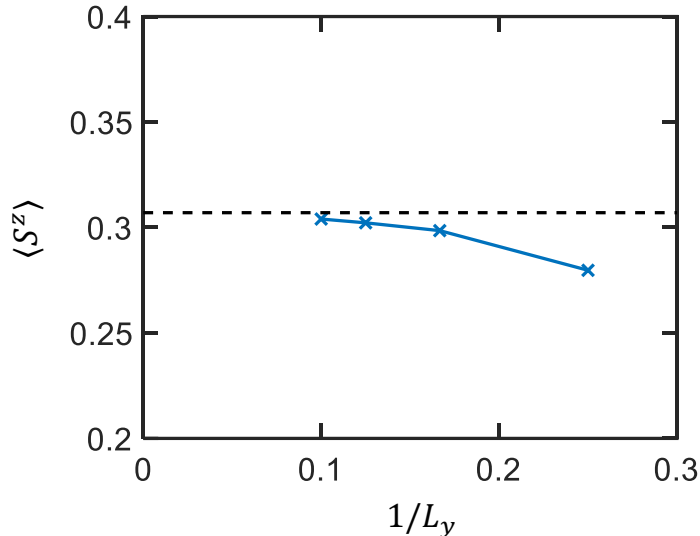


Figure 1.7: Finite-size scaling for the square-lattice Heisenberg AFM using different cylinders with aspect ratio $L_x/L_y = 2$. The $\langle S^z \rangle$ is extracted from the center of the cylinder with staggered pinning field of $0.5J$ on both edges. The finite-size scaling converges to the AFM order in 2D [1] denoted by the dashed line. Figure is reproduced from Ref. [3].

also estimate the order by comparing results using different aspect ratios. A more detailed analysis is presented in the original paper Ref. [3].

This method of finite-size scaling of order parameter with applied edge fields has been frequently utilized throughout the thesis: for the magnetic order in the electron-doped t - t' - J model in Fig. A.1; for the nematic order in the square-lattice J_1 - J_2 ferro-antiferromagnetic model in Fig. C.3; as well as for detecting the narrow Ising- z phase in the honeycomb-lattice J_1^Δ - J_3^Δ ferro-antiferromagnetic model in Fig. 5.8.

1.8 DMRG scan calculations

One of the generic problems studied in condensed matter physics is the ground state phase diagram. The conventional approach is to carry out a series of DMRG calculations, each with a set of parameters corresponding to a data point in the phase diagram. Near the phase

boundaries where different phases compete, comparing calculations with different initial configurations is necessary to determine the true ground state.

An efficient alternative approach to map out the phase diagram is DMRG scan calculations [60, 62, 67–69]. Utilizing the fact that the computational cost of DMRG scales only linearly with the length of the system, a long cylindrical system is used wherein the Hamiltonian gradually varies along the length the cylinder. For a cylinder with length L_x , the Hamiltonian takes the form:

$$H(l_x) = H(\vec{\lambda}_1) + [(H(\vec{\lambda}_2)) - H(\vec{\lambda}_1)] \frac{l_x - 1}{L_x - 1}, \quad (1.8)$$

where $\vec{\lambda}_1$ and $\vec{\lambda}_2$ correspond to two points in the phase diagram, and $l_x = 1, 2 \dots L_x$. In this setup, a line in the phase diagram connecting points $\vec{\lambda}_1$ and $\vec{\lambda}_2$ is scanned through with a single DMRG calculation. One often encounters two or more phases in the scan, and the phase boundaries are automatically adjusted with DMRG sweeps, which reduces the risk of metastable states. After convergence is reached, the phases and their boundaries can be directly extracted from their positions on the cylinder.

In Fig 1.8 we show an example of using DMRG scans to construct the phase diagram (detailed studies are presented in Chapter. 5). Here the parameters for the phase diagram are Δ and J_3 . In Fig. 1.8(b) we show a scan calculation with J_3 varying from 0.1 to 0.7 at fixed $\Delta=0$. One can directly read the three phases and their boundaries along the cylinder, which becomes the $\Delta=0$ line in the phase diagram Fig. 1.8(a). With multiple DMRG scans including some with fixed J_3 and varying Δ , we eventually map out the 2D phase diagram as shown in Fig. 1.8(a).

The DMRG scans are very powerful and efficient as the first exploratory measures to investigate the phase diagram. They can be followed up with either zoom-in scans (focusing on a narrower range of parameters) or conventional non-scan calculations for more precise

1.9 Organization of the thesis

This thesis is a collection of several self-contained projects that apply and adapt DMRG for studying a variety 2D systems as well as their model reductions. It is organized as follows: Chapter 2 presents our DMRG studies of the ground state phase diagram of the extended t - J models. We found that while the models are consistent with the cuprates in antiferromagnetism and charge order, superconductivity nevertheless appears absent or marginal in hole-doped systems. Motivated by this discrepancy between the models and the cuprates, in Chapter 3 we carried out a DMRG-based downfolding of the parental three-band Hubbard model, seeking possible fixes to the previously studied single-band models. An effective model was derived via Wannier construction, which includes novel density-assisted hopping terms that appear to be important in enhancing hole-doped superconductivity. In Chapter 4, we examined the quantum spin nematic phase in the paradigmatic $S = 1/2$ square-lattice J_1 - J_2 ferro-antiferromagnetic Heisenberg model, employing a combination of DMRG and analytics. Our findings revealed that many-body effects induce significant contraction of the nematic phase compared to the naïve expectation. Chapter 5 presents a study of the anisotropic J_1^Δ - J_3 model on the honeycomb lattice, which is believed to be the fundamental model for many Kitaev material candidates upon adding bond-dependent terms. This chapter also includes my contribution to a study of the generalized Kitaev- J_3 model for α -RuCl₃.

Chapter 2

Ground state phase diagram of the extended t - J models

2.1 Introduction

There has been considerable recent progress in numerical simulations of the models associated with the cuprate superconductors—the 2D Hubbard and t - J models, and their variants [27, 70–89]. Like the materials themselves, these models have been found to exhibit a rich variety of phenomena, ranging from uniform antiferromagnetism (AFM) and d -wave superconductivity (SC) to charge and spin stripes. Some previously controversial issues have been mostly resolved, such as the existence of stripes. Striped states were first found as a Hartree Fock solution to the doped Hubbard model [90–93], and in the late 1990’s two of us used the density matrix renormalization group [94, 95] and found stripes as the ground state of the t - J model [96]. At that time this result was controversial, since other powerful simulation methods, such as variational Monte Carlo, could not confirm our results [97, 98]. In the last few years, with progress in a variety of methods combined with the use of several

simulation methods together, striped ground states have been confirmed not just in the t - J model [76, 81, 82, 99], but also the Hubbard model [70, 73–75, 83, 100, 101].

While d -wave singlet pairing has consistently been favored over other types of pairing in many approaches, it has been less clear in both the t - J and Hubbard models whether the ground state is superconducting or not. The role of stripes in competing against or enhancing pairing has also been difficult to determine. It has long been clear, however, that next nearest neighbor hopping t' has a crucial influence on the pairing. With a $-t_{ij}$ sign convention for hopping, our early DMRG for the t - J model found that a positive t' stabilizes the commensurate (π, π) antiferromagnetic correlations and enhances the d -wave pairing correlations, whereas a negative t' seemed to disfavor these correlations [84, 102]. Other work has suggested instead that a negative t' is important in destabilizing stripes so that SC can occur [73].

While DMRG has not changed fundamentally since the 1990's, there has been steady improvements in techniques, software, and computers since then. Here we have used these developments to return to a study of the t - t' - J model. We report here a detailed description of the ground state phase diagram as a function of t' and doping x , based on $L \times 8$ cylinders with L up to 50, with confirmation of the qualitative features using width 6 cylinders. Note that this model can be used to describe both the hole and electron doped cuprates: for $t'/t < 0$ it describes a hole doped system with electron filling $n_e = 1 - x$, while for $t'/t > 0$, based on a particle-hole transformation, one has an electron doped system with $n_e = 1 + x$.

Two important results of our study are (1) the finding of a coexistent antiferromagnetic d -wave SC and induced π -triplet p -wave SC regime in the electron doped system and (2) the lack of long range SC order in the hole doped case.

This paper is organized as follows: in Sec. 2.2 we introduce the t - t' - J model, the DMRG methods used, and the main observables that we study. In Sec. 2.3 we show the $t' - x$ ground

state phase diagram for $J/t = 0.4$ obtained from the $8 \times L$ cylinder calculations. Here the spin, charge and d -wave pairing strength for $t'/t = \pm 0.2$ are shown as the doping x varies slowly along the length of the cylinder. Combined with similar calculations with doping x fixed and t' slowly varying along the length of the cylinder, these results (details shown in Sec. 2.4) are used to determine the $t' - x$ ground state phase diagram.

The resulting phase diagram exhibits four distinct regions. In Sec. 2.5 we examine the lightly ($x \lesssim 0.14$) electron doped region in which there is coexisting AFM and strong d -wave pairing order. In addition there is necessarily also a p -wave triplet pairing component with center of mass momentum (π, π) . This order parameter does not depend upon a p -wave pairing interaction, but is dynamically generated by coexisting AFM and d -wave SC order parameters [103–107]. While it has the same form as the generator of infinitesimal rotations between AFM and SC order parameters in the $SO(5)$ theory [104], it appears here as an additional order parameter. Its strength relative to the AFM and d -wave order will be discussed. In the more heavily doped electron region discussed in Sec. 2.6 we find stripes with local AFM, and weaker d -wave and p -wave triplet pairing. In Sec. 2.7 we discuss the $t' < 0$ part of the phase diagram where we find conventional stripes and an unconventional width-3 stripe phase (W3 stripe) region but negligible pairing. In Sec. 2.10 we discuss the relationship of the sign of t' to the electron and hole doped cuprates and compare our results to experiments. Sec. 2.12 contains our conclusions.

2.2 Model and method

We study the t - t' - J model on a square lattice, with Hamiltonian

$$\begin{aligned}
 H = & \sum_{\langle ij \rangle \sigma} -t(c_{i\sigma}^\dagger c_{j\sigma} + h.c.) + \sum_{\langle\langle ij \rangle\rangle \sigma} -t'(c_{i\sigma}^\dagger c_{j\sigma} + h.c.) \\
 & + J \sum_{\langle ij \rangle} (\vec{S}_i \cdot \vec{S}_j - \frac{1}{4} n_i^{tot} n_j^{tot}) - \mu \sum_i n_i^{tot}
 \end{aligned} \tag{2.1}$$

here $n_i^{tot} = n_{i\uparrow} + n_{i\downarrow}$ is the total particle density on site i . $\langle ij \rangle$ denotes nearest neighbor pairs of sites and $\langle\langle ij \rangle\rangle$ denotes next nearest neighbor pairs of sites. Doubly occupied states are specifically excluded in the Hilbert space. For all calculations we set $t=1$ and $J=0.4$. A chemical potential μ is used to control the doping level in some of the calculations; in others the number of particles is fixed. We study cylinders, with open boundary conditions in the x direction and periodic boundary conditions in the y direction. We study width-6 and width-8 cylinders with lengths up to 50. Our primary focus is on the width-8 systems. Behavior in width 6 is similar and provides an indication that our width 8 results are relevant for 2D.

We use finite system DMRG using the ITensor library[108]. For this size system, keeping about 3000-4000 states is sufficient to measure local properties, provided that the calculation is not stuck in a metastable state. To control this issue, we perform a variety of simulations with different starting states and temporary pinning fields, comparing energies and convergence of different states, to gain an understanding of the low energy states and their orders. Some of the details of this process in subtle cases are discussed below. In many cases, such as a conventional striped state, starting in a product state with the holes near where they end up is all that is necessary, but one should try different fillings and spacings of the stripes. For example, 8 holes in a striped state might make either two 4-hole stripes or four 2-hole stripes. In such a case we would try both possibilities and compare energies.

We focus on local measurements of the density, the magnetization, and pairing. The hole density and magnetization are measured using $S_z = \frac{1}{2}(n_{i\uparrow} - n_{i\downarrow})$ and $n_{hole} = 1 - n_{i\uparrow} - n_{i\downarrow}$. To detect the superconducting order and structure in the grand canonical ensemble, we use the singlet (s) and triplet (t) link pairing operators

$$\Delta_{s,t}^\dagger(l) = \frac{1}{\sqrt{2}}(c_{l_1,\uparrow}^\dagger c_{l_2,\downarrow}^\dagger \pm c_{l_2,\uparrow}^\dagger c_{l_1,\downarrow}^\dagger) \quad (2.2)$$

where the + and - are for singlet and triplet, respectively, and l_1 and l_2 are the two sites of link l .

The expectation value $\langle \Delta^\dagger + \Delta \rangle$ gives the local pairing strength. For a d -wave superconductor, $\langle \Delta_s^\dagger + \Delta_s \rangle$ switches sign between bonds in the x and y directions[109].

2.3 Phase diagram

We begin by presenting the approximate phase diagram of the model in the doping (x)–nearest neighbor hopping (t') plane, the detailed features of which are explained later. A key distinction is the difference between positive and negative t' . The t - J model cannot be doped above half-filling, so it does not appear that one can simulate electron-doped cuprates. However, a particle-hole transformation of the single band Hubbard model maps electron doping to hole doping, but with a change in the sign of t' . One can then view the t - J model as a low energy description of this particle-hole transformed Hubbard model. We discuss this in more detail in Sec. 2.10. The key point is that we can view $t' \approx -0.2$ as applicable to the hole-doped cuprates, while $t' \approx 0.2$ is applicable to the electron doped cuprates. We will refer to the regions of the phase diagram using this terminology.

Our most useful tool in determining the phase diagrams are scan calculations, where in a long cylinder we slowly vary one parameter of the model, either t' or the chemical potential

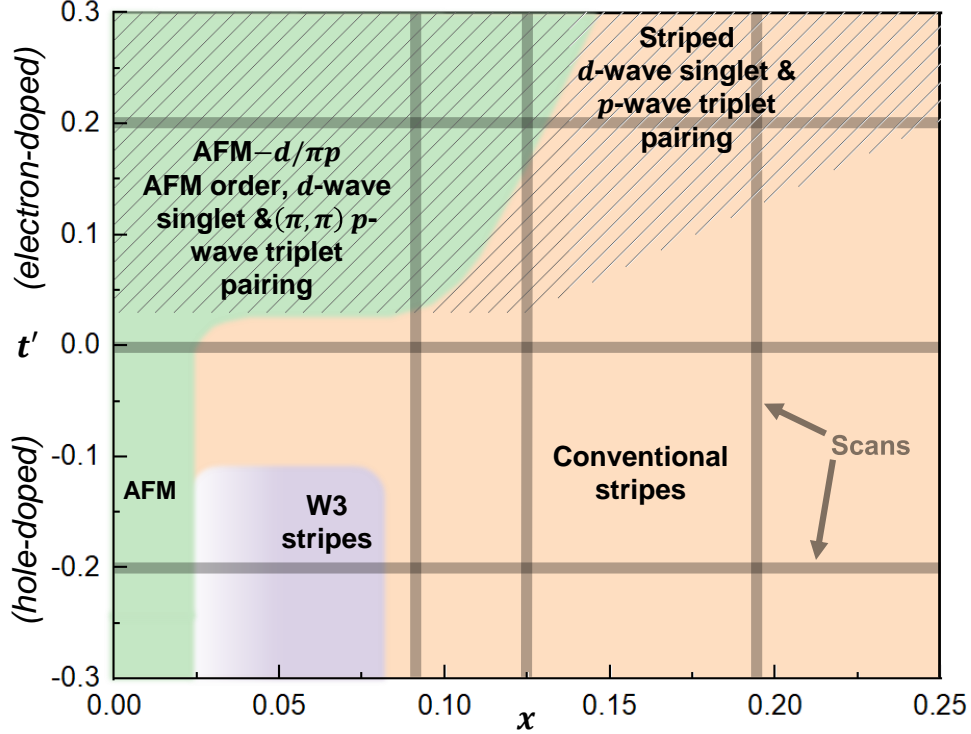


Figure 2.1: Approximate phase diagram in the $x - t'$ plane, where x is the doping and t' is the next-nearest neighboring hopping, for width-8 cylinders. The six gray lines indicate the location of parameter-varying “scan” calculations on long cylinders which were the main tool to determine the phase diagram. The green indicates commensurate AFM order; the beige represents conventional stripes, which modulate π -phase shifted domain walls in the AFM order. The slanted lines indicate d -wave pairing order. The simultaneous presence of d -wave pairing and AFM correlations induces weaker momentum- (π, π) p -wave order.

μ , to scan a whole line of the phase diagram. These lines are shown in gray in Fig. 2.1. These scans are detailed in the next section. Much of the phase diagram is taken up by a phase with conventional stripes. These stripes are lines of increased hole density two or three sites wide which act as domain walls to π -phase shifted AFM (or at least significant local AFM correlations). Although the holes in these stripes correlate into pairs, the pairs tend to lack phase coherence, and pairing correlations are weak. Significantly, negative t' is found to decrease the pairing correlations. This phase makes up most of the $t' < 0$ side of the diagram.

There is also a novel type of striped phase in a small region of the phase diagram with $t' < 0$. In this W3 striped phase, the stripes are predominately one site wide with exactly

two rows of mostly undoped sites between them acting as a spin-ladder. The holes within stripes are unpaired with a spacing of about 4 between holes. The Heisenberg two-leg ladder is spin-gapped, with very short range spin correlations[110], and the “ladders” in the W3 phase behave similarly. The stripes in W3 do not induce a π phase shift to the spins on either side, probably due to the combination of low doping within the stripe and the short range spin correlations. Instead of acting as a domain walls, they decouple the spin ladders. The W3 phase appears to have substantial decoupling between the undoped ladders and the doped chains, and the transverse period is locked at 3 lattice spacings. The W3 phase (like a t - J chain[111]) does not exhibit pairing. For $t' < 0$, commensurate AFM order is present only very close to zero doping; stripes break up the AFM order very quickly on doping.

For t' positive above a small threshold, one enters a very different low-doped phase. This phase has three types of order simultaneously. The two dominant forms of order are AFM and d -wave superconductivity, which have also been found in recent studies of the Hubbard model with positive t' [85]. There are no signs of stripes at low doping, and the magnetic order is commensurate at $Q = (\pi, \pi)$. The d -wave order is robust; unlike in previous studies at $t' = 0$ where determining whether the system is superconducting or not requires careful scaling, here its presence is very clear. These two dominant orders, d -wave pairing and AFM, combine to form a weaker triplet p -wave order at wavevector $Q = (\pi, \pi)$ [103, 112–115, 115–117]. This order comes about because the AFM order breaks $SU(2)$ symmetry, so that singlet and triplet pairing are no longer distinct, and the nonzero wavevector reflects the wavevector of the AFM order. There is no separate attractive conventional interaction in the p channel; this derivative order is purely a consequence of the other two orders.

In the higher-doped $t' > 0$ region, a superconducting striped phase appears. This phase looks locally much like the lower doped phase, but with stripes. The stripes look like conventional stripes in most respects, but they exhibit significant d -wave pairing, unlike the $t' < 0$ striped phase. The stripes act as domain walls to the AFM order, and locally one sees derivative

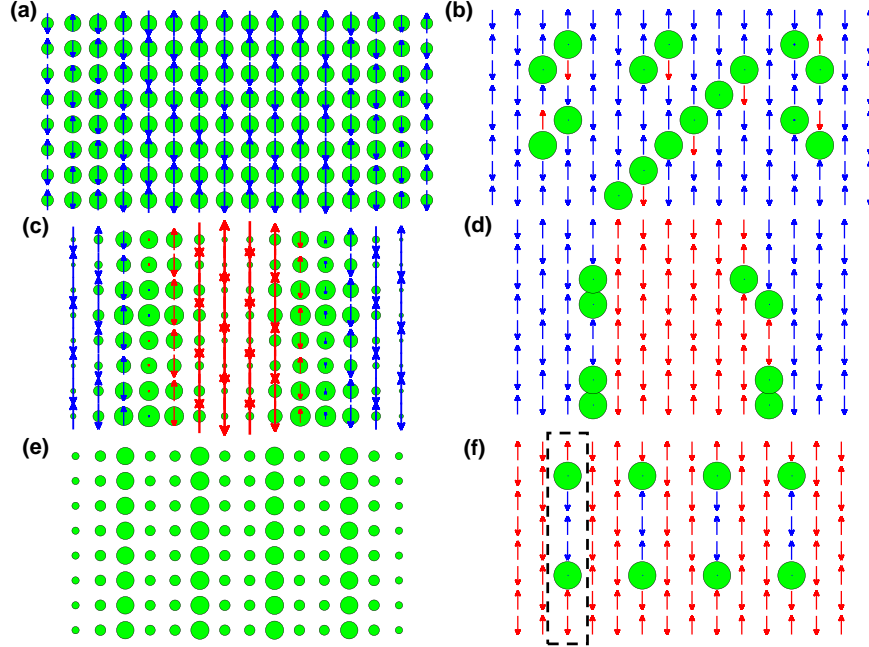


Figure 2.2: Local properties (left) and a high-probability product state (right) of systems in different phases. The left panels show conventional local measurements for ground states in three different phases. The length of the arrows and the area of the circles represent $\langle S_z \rangle$ and local doping respectively. The spins are colored to indicate different AFM domains. The right panels show particular product states which occurred with maximum probability in a particular search within the corresponding state (see text). (a) and (b): electron low doped phase with $t' = 0.2, x = 0.12$, with simultaneous pairing and AFM order. The highest probability configuration of a pair of holes is diagonal-next-nearest neighbor. (c) and (d): Conventional stripe phase at $t' = 0, x = 0.07$, where half-filled stripes form, and pairing is visible within the stripes, but lacking phase coherence. (e) and (f): W3 striped phase at $t' = -0.2, x = 0.07$, with holes unpaired within the stripes.

πp triplet order as well, modulated by the stripes. The pairing overall is somewhat weaker in the higher doped phase, probably because of the stripes. But while the stripes somewhat compete with superconductivity, the main driver against pairing appears to be negative t' itself, rather than t' acting through stripe formation. A likely mechanism for this is that positive t' directly increases the mobility of pairs[118], making it easy for them to phase cohere and to avoid becoming locked into stripes.

In Fig. 2.2 we show non-scan simulations of three of the phases, emphasizing their differences. An alternate view is given by the high-probability product state plots shown in the right

panels. These product states are determined from the ground state by a limited search for the most probable product state. One way to search for a probable spin configuration is to sequentially go through the sites of the lattice, and at each site, pick the most probable spin state. After each spin is picked, the wavefunction is projected to reflect this, just as a physical measurement of spin i (say finding the up state) would leave the wavefunction projected into the associated up- i space. However, this approach fails in the presence of holes, since at low doping there are far fewer holes than spins, and the holes end up appearing at the end of the search path, i.e. mostly on the right side of the system, which is a low probability configuration. Instead, here we will search for the hole positions separately, finding the most probable position for a hole over all sites at each step, using the hole density of the projected wavefunction. After the holes are found, then we perform a determination of the spin configuration with a fixed path through the rest of the sites, optimizing each spin and projecting.

This gives a view of the states that is hard to see in local measurements or correlation functions. In particular, in the d -wave phase in panel (a)-(b), one sees the holes grouped in pairs, with the most probably configuration of a pair being diagonally next-nearest neighbor, as found in earlier work[119]. In panel (b) one sees an apparent diagonal stripe, but there is no sign of this in the ordinary measurements of panel (a). It may be that this is only slightly more likely than many other different configurations.

In the conventional striped state shown in panels (c)-(d), pairs of holes appear as the most probable state, but the state has only short ranged pairing correlations and the small hole probability between the stripes suggests that the binding of the pairs to the stripes is suppressing superconductivity. In the W3 striped state shown in panels (e) and (f), the most probable state has the holes at their maximum separation within the stripes, with domain walls visible in the vertical direction across the holes, instead of the horizontal. This con-

figuration is consistent with the idea that the stripes here imitate the 1D $t - J$ chain [111], and that one can view the holes as holons living in a squeezed Heisenberg chain of spins.

2.4 Scans varying doping and t'

We now discuss the scan calculations which were used in constructing the phase diagram. As shown in Fig. 2.3, in one set of scans, t' was fixed and the doping x was slowly varied along the length of the cylinder while in another set x was fixed and t' was varied. A linear variation of the chemical potential with the length l_x down the cylinder gave an essentially linear increase of the doping x . A similar application of a gradient in the chemical potential has also been utilized in cold-atom experiments[120]. However, for the $t'=0.2$ scan, it was necessary to vary the chemical potential slowly in the low doping region where AFM, d -wave and $\pi - p$ -wave triplet pairing appeared. In the t' varying case, the chemical potential also needed to be adjusted to keep the doping approximately constant across the system¹.

A key feature of the scan calculations is to reduce the problem of metastable states. For fixed parameters (i.e. a non-scan calculation) one may happen to be near a phase boundary, and determining which side one is on may involve small energy differences. In contrast, using a scan one is likely to pass through the phase boundaries, and the system will automatically adjust the location of the boundaries to account for the energies. The calculations are stabilized by the parts of the cylinder where the system is well within one phase or another.

In non-scan calculations where one is looking for a particular order, it is common to “pin the edges” with a corresponding field applied to the edge sites. This is not so clear-cut a procedure for a scan going through different phases, but, in fact, often in a DMRG calculation

¹The chemical potential is of form $\mu(l_x) = \mu_0 + a\sqrt{1 + (b|2l_x - L_x|/L_x)^2}$ with a and b to be adjusted and different for left and right half. This form of chemical potential varies slower and connects smoothly in the middle.

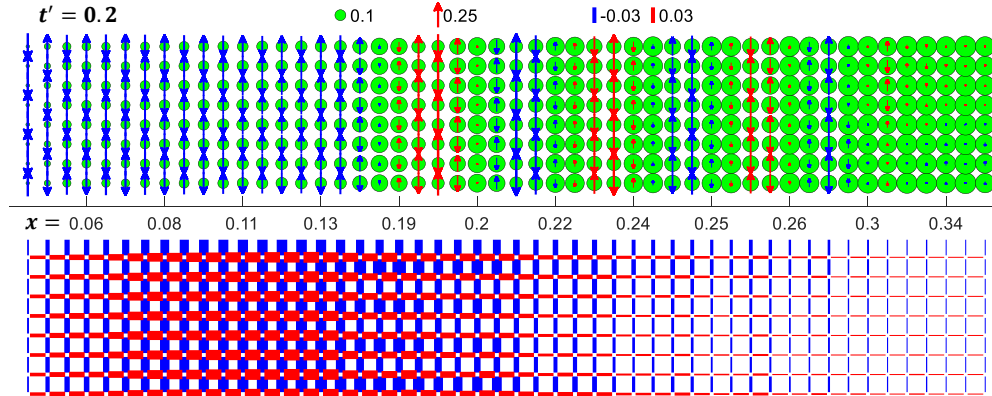


Figure 2.3: A doping-varying scan on a 50×8 cylinder with $t'=0.2$, appropriate for electron-doped cuprates. Spin, charge are shown in the upper plot in the same way as in Fig. 2.2. The lower plot shows the d -wave singlet pairing with its sign/amplitude indicated by the color/thickness of bonds. The numbers on the middle axis indicate the approximate local doping. No pair field is applied. In the underdoped region ($x \lesssim 0.13$) the system exhibits AFM with strong d -wave pairing. In the overdoped region ($x > 0.13$) stripes are present, with pairing persisting to about $x \approx 0.25 - 0.3$.

pinning fields are not necessary. Instead, DMRG can self-pin in a large 2D system. This aspect of DMRG calculations is well-known among DMRG experts, but less so by others, so we give a detailed explanation of this effect in Sec. 1.6. The gist is that DMRG tends to break a continuous symmetry and develop an order parameter just as a real experimental sample does. The broken symmetry goes away in the limit of large bond dimension, but for a range of moderate bond dimensions the system develops an order parameter similar in magnitude to that of the 2D thermodynamic limit. The required bond dimension to eliminate the broken symmetry increases rapidly with system size. Attempts to converge beyond this broken symmetry plateau can be counter-productive, since in the symmetric phase the order can only be seen through correlation functions, and one can miss unexpected orders. In addition, correlation functions are inherently much less accurate than local measurements [3]. In our scans, we use this effect to our advantage: in systems where there does appear to be robust d -wave superconductivity(SC), we do not pin it with an external field but rather we allow the system to self-pin. In systems where d -wave SC is suppressed, we apply a weak global pairing field. In this case, we may get some false positive signals of SC, but its absence is

a clear sign that a superconducting state is not a low energy state. In some cases we also apply a magnetic pinning field on one or both edges to reduce edge effects [2]. It should be pointed out that such fields have almost no effect on the magnetic order in the bulk which appear as long as we are in the “broken symmetry plateau”.

Figure 2.3 shows an x -varying scan with a fixed $t' = 0.2$ corresponding to electron-doped cuprates. In the underdoped region we find coexisting uniform AFM, strong d -wave singlet pairing and (π, π) p -wave triplet pairing (detailed discussion later in Sec. 2.5). As one increases doping away from half-filling, the pairing increases rapidly and $|\langle S_z \rangle|$ decreases slowly. When the doping is further increased beyond $x \sim 0.14$, conventional-looking stripes emerge. The transition to stripes is rather sharp. The stripes still have robust pairing, but the magnitude of the order parameter is reduced. The point of optimal doping, where pairing is maximum, is near $x = 0.14$, in the uniform phase. Within the striped phase, pairing decreases with higher doping. It eventually disappears in a smooth way near $x \sim 0.25 - 0.3$

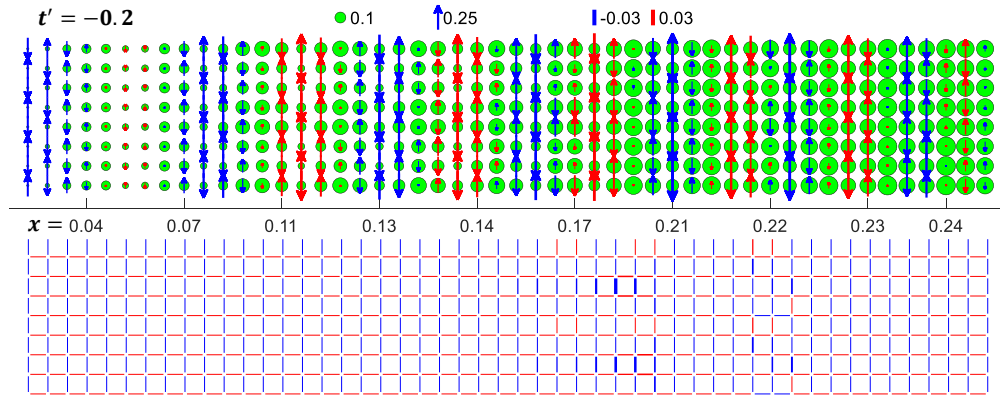


Figure 2.4: A doping-varying scan on a 50×8 cylinder with $t' = -0.2$, appropriate for hole-doped cuprates. A staggered magnetic pinning field of 0.03 is applied on the left edge. A global d -wave pair field of 0.005 is applied to measure the pairing response. The system exhibits stripes across the whole doping range shown here with minimal pairing response to the applied pairing field.

Figure 2.4 shows a similar x -varying scan but with $t' = -0.2$, corresponding to hole-doped cuprates. Other than a small region showing signs of the W3 striped phase around $x \sim 0.06$, the whole scan shows conventional stripes. As one increases doping, the magnitude of the

density oscillations first increases until around $x = 0.2$, and then decreases. Pairing is almost completely suppressed despite a global d -wave pairfield of 0.005. Pairing remains weak even if the pairfield is made rather strong, say, 0.03. In terms of the pairing response and the applicability of the t - t' - J model to the cuprates, Figure 2.3 and Fig. 2.4 indicate a clear contradiction: pairing is much stronger in the hole doped cuprates than we find in the t - t' - J model.

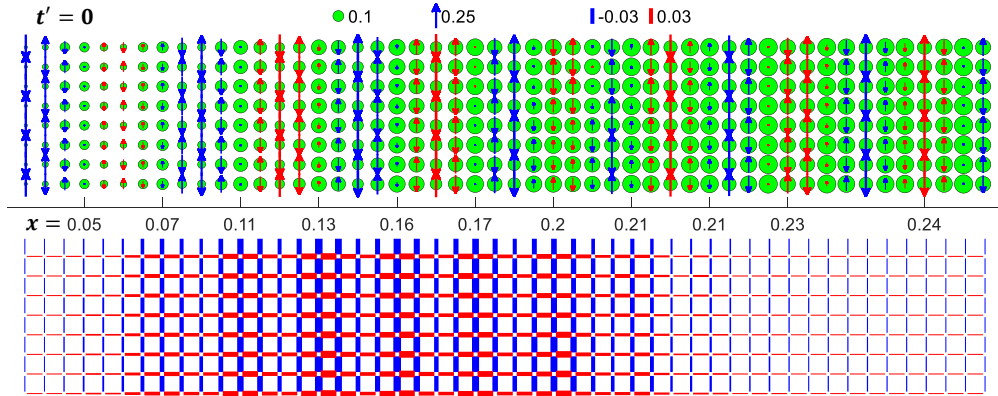


Figure 2.5: A doping-varying scan on a 50×8 cylinder with $t' = 0$. A staggered magnetic pinning field of 0.05 is applied on the both edges. A global d -wave pairfield of 0.005 is applied to measure the pairing response. The system is striped and pairing response peaks near $x = 0.15$, but in non-scan calculation without applied field the system shows no local pairing and the pair-pair correlations die rapidly with separation.

Figure 2.5 shows an x -varying scan with $t' = 0$. While this case does not directly map to the cuprates, it has been studied often because of its simplicity. We find a hole density and spin pattern similar to the $t' = -0.2$ scan. Around $x \sim 0.07$ there are again some signs of a W3 striped phase, but separate calculations with fixed doping find this W3 stripe is metastable and higher in energy ($\mathcal{O}(0.001t)$ per site) than the conventional striped phase at $t' = 0$. Despite a similar striped structure, the pairing response with $t' = 0$ is much stronger than at $t' = -0.2$. Under a global d -wave pairfield of 0.005, the pairing peaks around $x = 0.15$ with a value $\langle \Delta^\dagger + \Delta \rangle \sim 0.06$. If the pairfield is turned off, pairing decays slowly. We find that at $t' = 0$, the paired state is not the ground state when comparing its energy with the non-paired state. In the global phase diagram, the boundary line where pairing appears is

at slightly positive t' . This closeness of the boundary helps explain why in previous studies at $t' = 0$, it has been very difficult to determine if the ground state is superconducting.

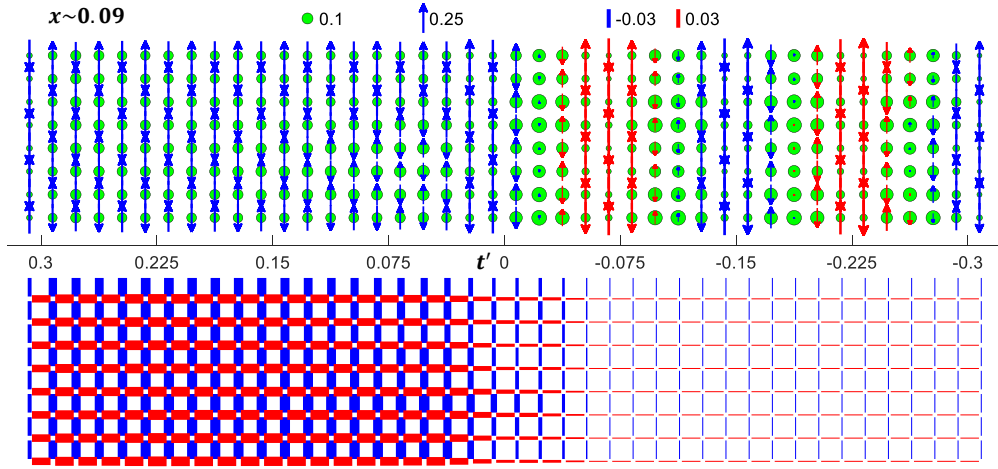


Figure 2.6: A t' -varying scan on a 42×8 cylinder with doping $x \sim 0.09$. A staggered magnetic pinning field of 0.03 is applied on both edges. No pair field is applied. For $t' > 0$ we see the AFM- $d/\pi p$ phase, while in the region with negative t' we find a conventional stripe phase and pairing is suppressed.

We now show another three scans where we keep x approximately constant and vary t' from 0.3 to -0.3. Figure 2.6 shows a low doping case, $x \sim 0.09$. The contrast between positive and negative t' is striking. For $t' > 0$ we find the AFM- $d/\pi p$ phase with uniform AFM and strong pairing. For $t' < 0$ we find conventional stripes and a rapid and strong suppression of the pairing response.

Figure 2.7 shows a medium doping $x \sim 0.13$. Here the boundary of uniform density versus stripe order has shifted to $t' \sim 0.1$. The striped state for $t' > 0$ has pairing, although it is weaker than in the AFM- $d/\pi p$ phase.

Figure 2.8 shows a high doping case with $x \sim 0.19$. In this case there are stripes for the whole range of t' . However, pairing order is only present for $t' \gtrsim 0.1$.

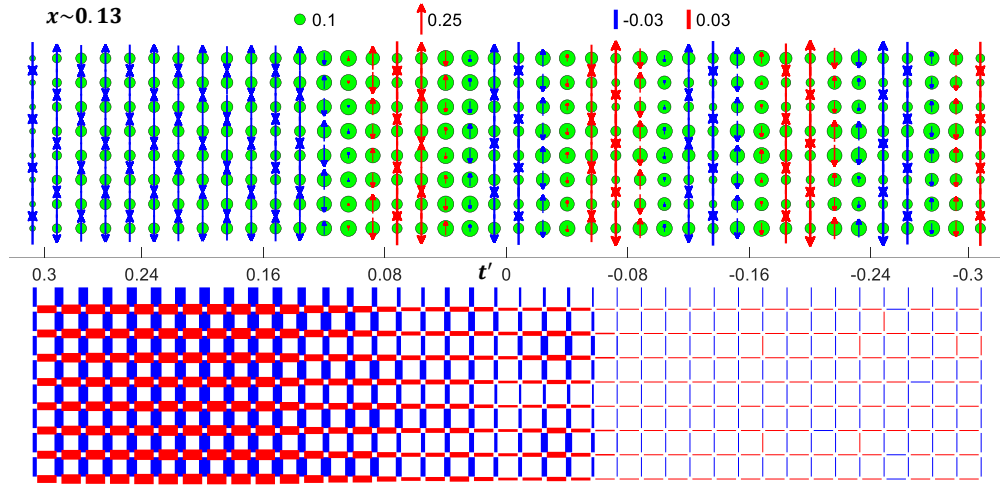


Figure 2.7: A t' -varying scan on a 40×8 cylinder with doping $x \sim 0.13$. No pair field is applied. A staggered magnetic pinning field of 0.03 is applied on both edges. For $t' > 0$ we see the AFM- $d/\pi p$ phase which becomes striped for smaller t' . In the negative t' region the stripes continue but without pairing.

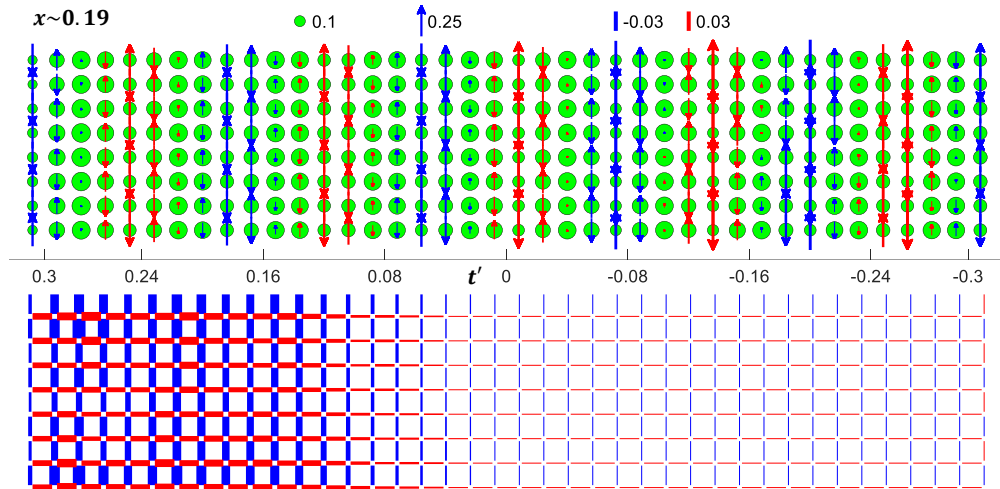


Figure 2.8: A t' -varying scan on a 40×8 cylinder with doping $x \sim 0.19$. No pair field is applied. A staggered magnetic pinning field of 0.03 is applied on both edges. There are stripes across the whole system, but pairing only for larger positive t' .

2.5 Electron low-doped phase with coexisting uniform AFM, d -wave singlet and (π, π) p -wave triplet pairing (AFM- $d/\pi p$)

We now consider the individual phases in detail, starting with the phase with three order parameters at low doping and $t' > 0$. This region corresponds to electron-doped cuprates. There are two dominant orders: uniform AFM and a strong d -wave singlet pairing. As a result of these two orders there is also a (π, π) p -wave triplet pairing. We call this phase AFM- $d/\pi p$, and it exists in a broad region defined roughly by $t' > 0$ and $x < 0.14$. Details of this phase for a non-scan calculation at $x = 0.12$ and $t' = 0.2$ are shown in Fig. 2.9. In parts (a) and (b) we show the doping, spin, and singlet pairing expectation values. All these quantities are uniform across the system. No applied pairing field was used. The presence of nonzero pairing order helps the density become more uniform, counteracting any oscillations due to the open boundaries. The magnitude of the pairing order is $\langle \Delta_s^\dagger + \Delta_s \rangle = 0.081$, and the difference in sign between vertical and horizontal bonds signifies d -wave order. We judge the size of the order parameter to be quite large; in particular, if one does apply a pairing field, one cannot readily make it much larger. Also, the simulations are clear and unambiguous; there do not appear to be any other competing states. Starting from a non-pairing initial product state, the system spontaneously breaks particle-conservation symmetry and produces the pairing order. As mentioned before, Sec. 1.6 has a detailed discussion for spontaneously broken symmetry in DMRG.

As shown in Fig. 2.9(c) we also observe a smaller (π, π) p -wave triplet pairing in addition to the strong d -wave singlet pairing. It is uniform in amplitude and has (π, π) $p_x - p_y$ form:

$$\langle \Delta_t(l_x, l_y) \rangle = e^{i\pi(l_x+l_y)} [\langle \Delta_t(l_x, l_y, x) \rangle - \langle \Delta_t(l_x, l_y, y) \rangle] \quad (2.3)$$

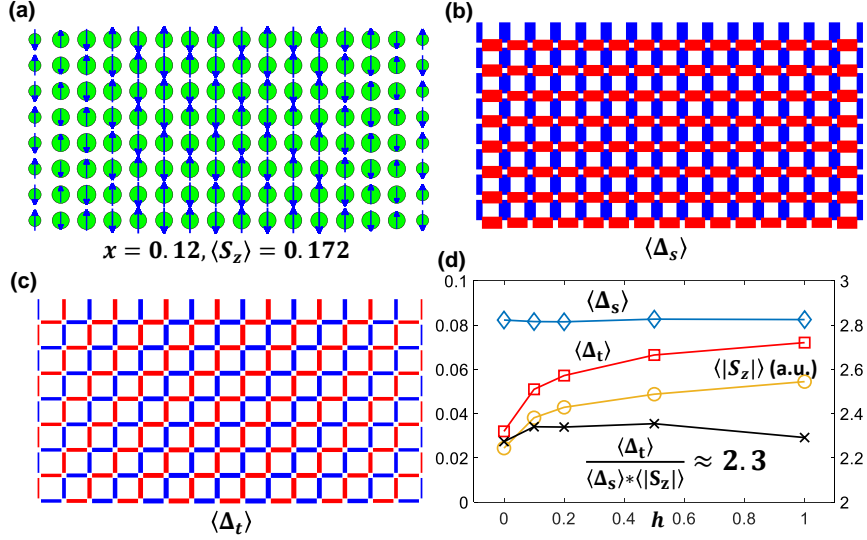


Figure 2.9: The AFM- $d/\pi p$ phase at fixed $t'=0.2$ and $x=0.12$. (a) and (b) show spin, charge, and d -wave singlet pairing as in previous plots. In (c), we show triplet link pairing, where we find (π, π) p -wave order. For (d), we plot singlet and triplet pairing, as well as the spin expectation value (left-axis scale), for systems which have had a global staggered magnetic field h applied; each value of h is a different simulation. The singlet pairing is nearly independent of h while the triplet pairing and magnetization both increase with h , but the indicated ratio (black crosses, right axis) is nearly constant.

with $\Delta_t(l_x, l_y, x/y)$ being a triplet pairing on a horizontal/vertical link with left/lower site (l_x, l_y) .

The overall phase of triplet pairing is determined by the overall phase of the AFM order and d -wave pairing. This triplet order is a consequence of the other two orders, not a competing order. As mentioned before, The existence of AFM order breaks $SU(2)$ spin symmetry, so that singlet and triplet pairing are no longer distinct, making the d -wave pairing have a triplet component. The nonzero wavevector reflects the wavevector of the AFM order. The magnitude of the triplet pairing is roughly proportional to the singlet pairing: $\langle \Delta_t \rangle / \langle \Delta_s \rangle \approx 0.4$, if no magnetic field is applied, and this ratio is mostly t' independent.

To further study the interplay of AFM, singlet and triplet pairing, we applied a global staggered magnetic field to the system which directly enhances the AFM order. Figure 2.9(d) shows that under this field, both magnetization and triplet pairing are enhanced while singlet pairing is mostly unchanged. It is interesting that there is no competition between strong

AFM order and d -wave pairing; they happily coexist, but as a consequence of increased AFM order the triplet order gets larger. Defining $A(x)$ through the following relation between these three quantities:

$$\langle \Delta_t \rangle = A(x) \langle \Delta_s \rangle \langle S_z \rangle, \quad (2.4)$$

we find that $A(x)$ varies slowly with doping (2.3 for $x = 0.12$, 2.0 for $x = 0.065$). We further verify that this relation holds when a global d -wave singlet pairfield is applied. This relation is qualitatively consistent with several studies where there is coexistence of AFM, d -wave singlet pairing and (π, π) p -wave triplet pairing[106, 107, 113]. This further implies that this (π, π) p -wave triplet pairing is purely parasitic and relies on the existence of both AFM and d -wave singlet pairing.

2.6 Higher electron doping phase: stripes with d -wave singlet and striped p -wave pairing

In the electron overdoped, $t' > 0$ region of the phase diagram we observe a striped phase with roughly uniform d -wave singlet pairing and modulated p -wave triplet pairing. In Fig. 2.10(a-c) we show local expectation values for a point in this phase at $x = 0.20$ and $t' = 0.2$. The striped phase looks like stripes at $t' < 0$ if one only looks at the charge and spin. Unlike that case, here we have clear d -wave pairing, although not as strong as at lower doping. In this case, starting in a product state, the system can get stuck in an unpaired state, but applying a pairfield for a few sweeps allows it to go to the lower energy (by about $o(0.001t)$ per site) paired state with a singlet pairing order $\langle \Delta_s^\dagger + \Delta_s \rangle = 0.044$. (In a width 6 system, the unpaired state is not metastable; starting from a product state, the DMRG sweeps readily find the paired state. More comparisons with width 6 systems are made in Sec. 2.9. The

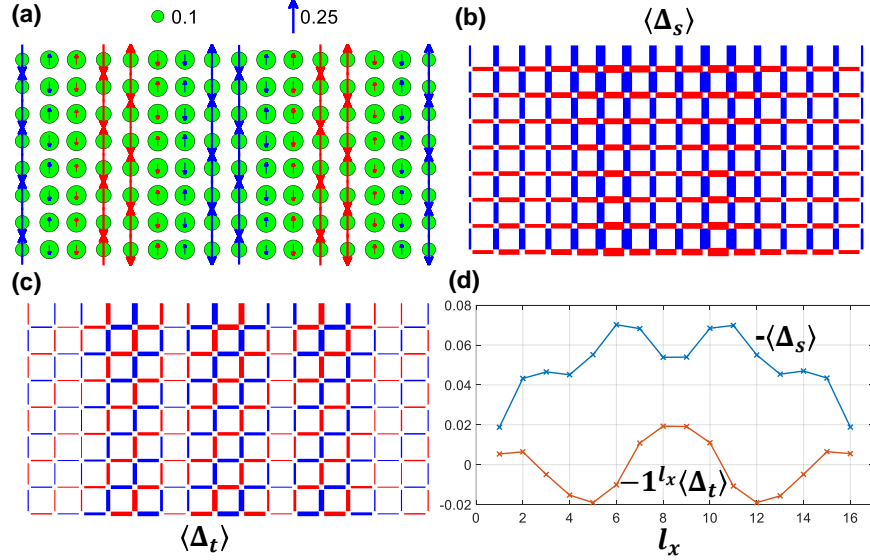


Figure 2.10: Higher doped positive t' phase with stripes and pairing. The doping is $x = 0.20$ and $t' = 0.2$. (a), (b), and (c) are as in the previous figure. In (c), we see that the p pairing is modulated by the domain walls in the antiferromagnetism. This is apparent in (d), which shows the singlet pairing and the triplet pairing multiplied by $-\mathbf{1}^{l_x}$ versus l_x . The singlet pairing has small modulations with peaks at the stripes, while the triplet pairing oscillates with nodes at the stripes.

pairing is only slightly larger on the domain walls compared to the region in-between them, as shown in Fig. 2.10(d).

Because there are local AFM regions between the stripes, one would expect also a triplet pairing component to appear. Figure 2.10(c) shows the p -wave triplet pairing for this system. Interestingly, the p -wave triplet pairing $\langle \Delta_t \rangle$ which is modulated by stripes shows a wave-like amplitude as one can see more clearly in Fig. 2.10(d). In contrast to the Δ_s which is only slightly bigger at the domain walls, the Δ_t order has nodes at the domain walls, reflecting its parasitic dependency on the AFM order.

2.7 Conventional stripe phase and low-doped W3 stripe phase

While the striped phase described in the previous section has a ground state with pairing, in a broader parameter region which includes the whole $t' < 0$ part except for extreme low doping, stripes still form but the ground state has no pairing. This phase is the conventional striped phase.

The hole and spin pattern of conventional stripes without pairing is very similar to stripes with pairing. One small difference, which one can see by comparing Fig. 2.3 and Fig. 2.4, is that the stripes at $t' = 0.2$ are homogeneous in hole density and spin along the stripes, while at $t' = -0.2$ there is a small modulation along each stripe. The difference in pairing is much more significant: the conventional striped state is non-superconducting. A state with pairing is nearby for t' near 0, and it can be seen as a metastable state in DMRG, but its energy rises as t' is made more negative and it is no longer metastable. For $t' = -0.2$, even a strong global pairfield triggers only a weak pairing response and the pair-pair correlation function shows exponential decay.

The W3 striped phase is distinct from the conventional striped phase, although both occur for $t' < 0$. Figure 2.11 shows non-scan results for the W3 phase, at a doping of 0.08, at $t' = -0.2$. The key to understanding the W3 phase is a Heisenberg two-leg ladder. A two leg ladder has a spin gap of about $J/2$, and we can think of this gap not just as the raising of excited state energies, but also the lowering of the ground state energy, making width two undoped ladder regions favored. The two-leg Heisenberg spin ladder has short-range spin correlations, with a correlation length of about 3.19[110]. This is in contrast to, say, a three leg ladder which is gapless with power law spin correlations. We do not find a W4 phase similar to the W3 phase but with 3-leg ladders; the two-leg ladder W3 configuration is the only such phase found. The stripes themselves resemble t - J chains, with one hole

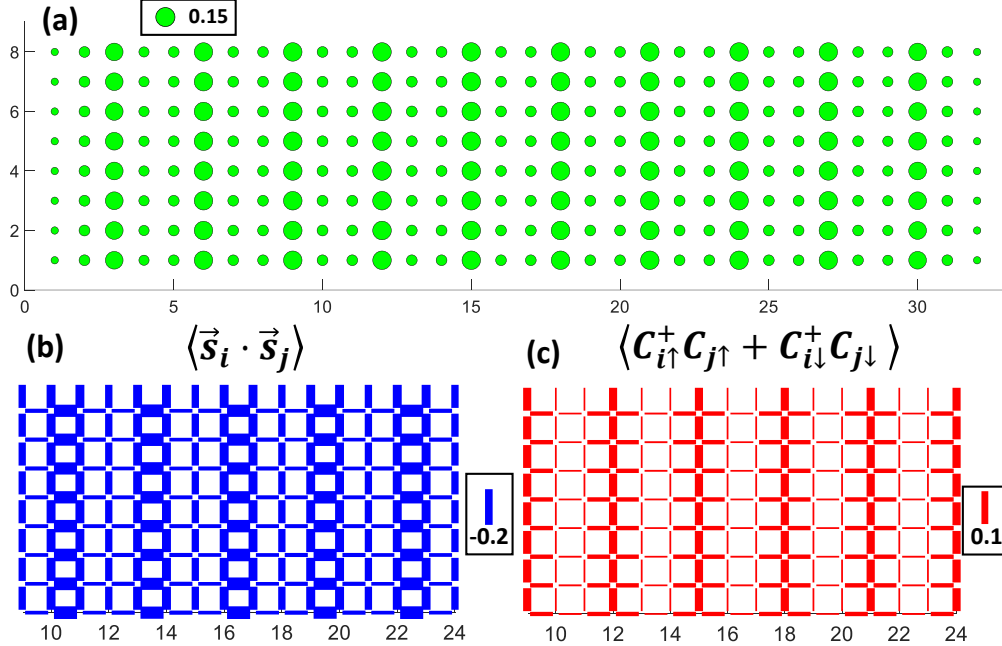


Figure 2.11: W3 striped phase on a 32×8 cylinder at $x = 0.08$, $t' = -0.2$. In (a) only the local doping is shown; the local spin measurements are zero. The stripes are strongly associated with single columns. In (b) we show the nearest neighbor spin-spin correlations, which are much stronger in the undoped width-two “ladders”. Longer distance spin-spin correlations are measured to decay rapidly. In (c) we show the link hopping, which is very strong along the stripes but also exhibits limited hops onto the ladders. The results together suggest significant decoupling between the chains and ladders.

per about four lattice spacings; holes are unbound, and there is strong hopping along the chain. There is also transverse hopping onto the ladders but this seems predominantly a single hop away from the chains. In the spin-squeezed picture of the t - J chain[111], the holes act as mobile domain walls in a Heisenberg chain; thus, for example, instantaneous singlet spin correlations are present across each hole. There is no attraction between holes. All these features seem to also describe the stripes in the W3 phase. The W3 phase seems even farther from superconducting than the conventional striped phase: there is no sign of paired holes(see also Fig. 2.2(f)).

In the W3 phase the spin correlations are short ranged in both directions. The low doping of each stripe and the weak transverse hopping make them unable to create π phase shifts in the local AFM correlations. There are negligible spin correlations between the ladders.

Within the ladders, vertical-separation spin-spin correlations are also short ranged, with a much more rapid decay compared to the conventional striped phase.

The W3 stripe shown in Fig. 2.11 is at its ideal filling for a width 8 cylinder: two holes per three columns or a doping of $x = \frac{2}{24} = 0.0833$. If we decrease the doping the phase does not change in a smooth way on width 8. Two holes per stripe and two-leg-ladder undoped regions are both favored in a quantized way. Decreasing the doping on width 8 causes defects (see Fig. 2.16) : limited regions which have wider spacing so that most of the cylinder can maintain a spacing of 3 between stripes. If the two-leg Heisenberg ladder picture is correct for the W3 phase, then the spacing of 3 would hold on any width cylinder. However, there is nothing in this picture that says the spacing of holes along a stripe must be exactly 4. We do not expect an odd number of holes per stripe, as that would require a spin excitation. But one might have different spacings on a much wider cylinder: for example, one might find four-hole stripes not just on a width-16 cylinder, but also, say, 14 and 18.

Another system where we can see the W3 phase is a width 6 cylinder, where the stripes run along the length of the cylinder. This is shown in Fig. 2.15(b). In this case two stripes and two ladders just fit. In the width 6 cylinder, we do find the spacing of holes on each stripe can be varied away from 4 slightly by adjusting the doping, consistent with the discussion above for wide cylinders.

2.8 Energy gaps

We can get further insight into the nature of the phases by studying their energy gaps associated with adding or removing particles. A generic formula for this sort of energy gap is

$$\Delta E_n = [E(N_0 + n) + E(N_0 - n) - 2E(N_0)]/2, \quad (2.5)$$

for adding or removing n particles at a time, where $E(N)$ is the ground state energy with N particles. This formula exhibits finite size effects due to the finite size of the system. The finite length manifests as an overall curvature of $E(N)$, which can be viewed as a shift in the chemical potential with N . In an infinite system, the chemical potential would not shift when adding a finite number of particles.

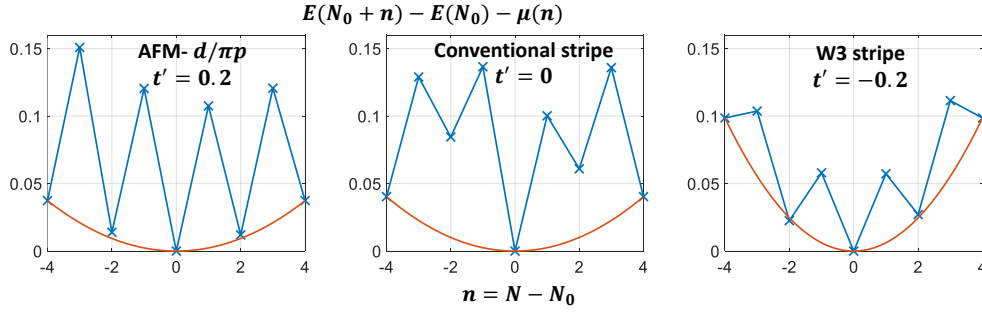


Figure 2.12: Energy versus number of particles, from which one can read off various gaps. The overall curvature is the result of using a finite length cylinder (32×6); the orange curve shows a quadratic fit to the points touching it. The chemical potential has been set to make the slope at the midpoint zero. Left: AFM- $d/\pi p$ phase with $t'=0.2$ at $x \sim 0.08$. Middle: conventional striped phase with $t'=0$ at $x \sim 0.08$. Right: W3 striped phase with $t' = -0.2$ at $x \sim 0.07$. Here the W3 stripe runs horizontally on width 6, displayed in Fig. 2.11.

Rather than extrapolations in system size, we find it more convenient to plot $E(N)$ directly, and fit the lower envelope of points to a quadratic function. This is shown in Fig. 2.12. The gaps are then measured by how many points rise above the quadratic fit. These calculations were done on a width 6 system for higher accuracy. For the W3 stripe calculations on width 6, two stripes run in the horizontal direction as shown in Fig. 2.15(b). Changing the number of particles changes the filling of these two stripes.

In the AFM- $d/\pi p$ phase, we see that an odd number of particles is higher in energy. This is because in this superconducting phase, an odd- N system has an extra quasiparticle, and we interpret the associated gap as the superconducting gap. Here, this is about 0.12. There is no sign of gaps associated with higher numbers of particles. In contrast, in the conventional stripe phase, we see two gaps involved. Systems with odd N exhibit the highest energies, corresponding to broken pairs. However, we also see that in the even- N sector, multiples of

four are lower in energy than non-multiples of four. This is because the stripes in this system have four holes, composed of two pairs, which are bound. A non-multiple of four must have an isolated pair (see Fig. 2.15(a)) , with an energy higher by about 0.05.

In the right panel showing a W3 striped phase, we see a smaller single particle gap compared to the previous two cases. This state is unpaired but the energy is still sensitive to having half-integer total spin. One would expect an extra hole mainly living in a stripe, since a t - J chain is gapless but a Heisenberg ladder has a large spin gap. It is not clear whether the finite gap seen is a consequence of the finite length, the even circumference of the cylinder, or some other effect.

2.9 Comparisons with width-6 cylinders

In this section we report results for two doping-varying scans in width-6 cylinders which support the qualitative features of the ground state phase diagram in Fig. 13. We also show some details on the higher energy states which determine the energy gaps in Sec. 7.

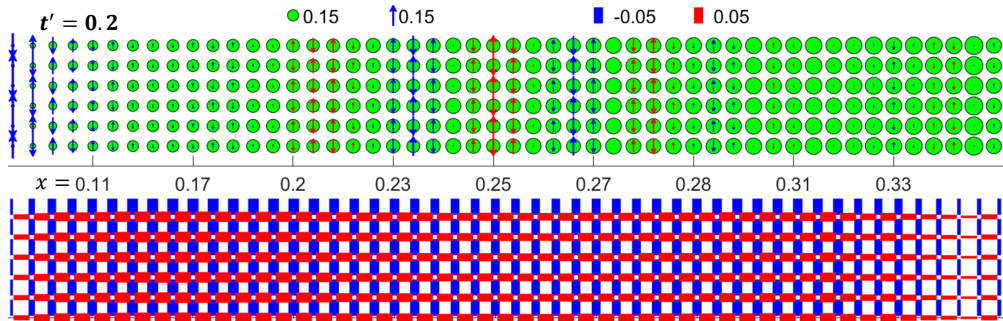


Figure 2.13: A doping-varying 50×6 cylinder with $t' = 0.2$ which simulates electron-doped cuprates. The numbers on middle axis indicate the averaged local doping. A staggered magnetic pinning field of 0.03 is applied on the left edge. No pair field is applied. At low doping there is AFM order which continuously transition to stripe and then uniform pattern at higher doping.

Figure 2.13 shows a doping-varying scan with fixed $t' = 0.2$, corresponding to the electron-doped cuprates. Similar to what is seen on width-8 cylinders, there is a coexisting AFM- $d/\pi p$ phase at low doping, and a striped phase with pairing at higher doping. Quantitatively there are several differences. The AFM- $d/\pi p$ phase has a narrower doping range with weaker AFM order compared to the width-8 system. The transition between the AFM- $d/\pi p$ phase and the striped phase is less sharp in the width-6 system. Pairing in the width-6 system exists over a wider doping range than in the width-8 system.

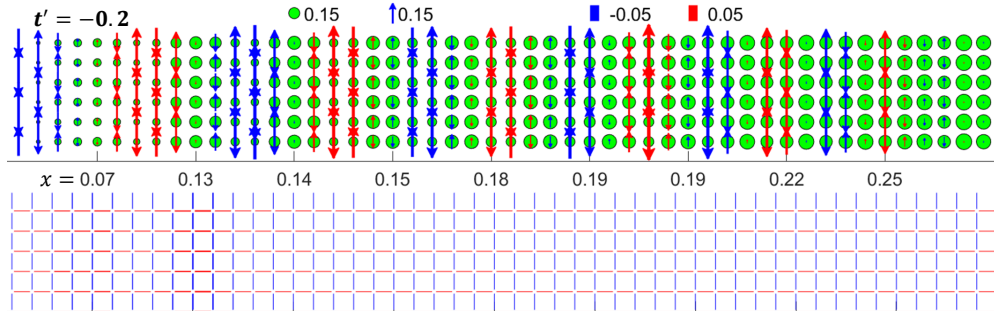


Figure 2.14: A doping-varying 50×6 cylinder with $t' = -0.2$ which simulates hole-doped cuprates. A staggered magnetic pinning field of 0.03 is applied on the left edge. A global pair field of 0.005 is applied to measure the pairing response. There's stripe pattern across all doping with pairing suppressed

Figure 2.14 shows a doping-varying scan with fixed $t' = -0.2$. This is similar to the width-8 results other than the lack of the W3 striped phase at low doping. A single vertical W3 stripe with two holes on width 6 has a substantially different doping per unit length than on width 8, where we do see the W3 stripes.

In determining the energies shown in Fig. 12, some of the states have unusual configurations, such as defects in the stripe pattern. For example, when one removes two holes from a striped calculation, the missing holes are likely to be removed from one particular stripe. Figure 2.15(a) shows an example of this, with two holes removed from the third stripe from the left. The state is higher in energy because of the binding of pairs into stripes. We expect there to be other similar states at nearly the same energy, and a more precise calculation would show superpositions of these configurations.

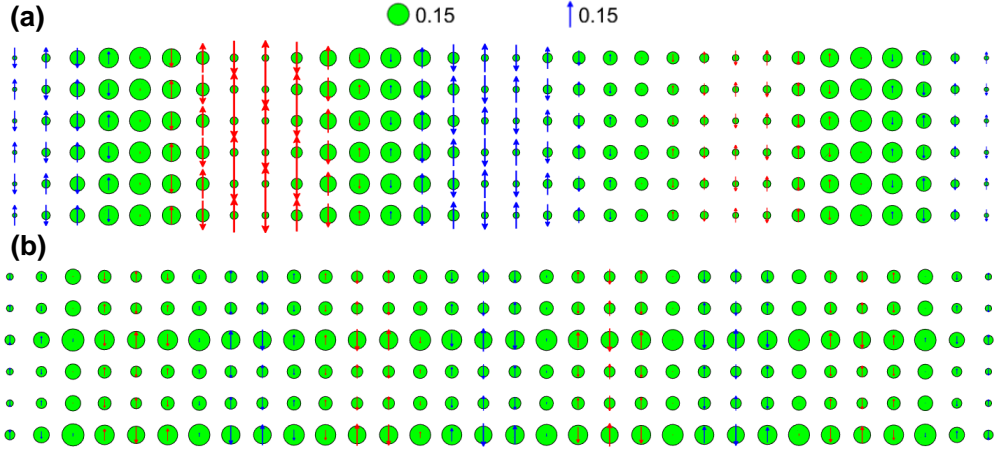


Figure 2.15: (a) A conventional striped phase with two holes removed from the third stripe from the left. (b) A W3 phase with the stripes running horizontally in a width-6 cylinder at a doping of $x = 0.083$.

Figure 2.15(b) shows a W3 phase with the stripes running horizontally in a width-6 cylinder. This configuration allows one to vary the number of holes to get the energies in Fig. 12. On this width, there are some noticeable spin moments and a slight charge variation along the stripes due to the open boundaries.

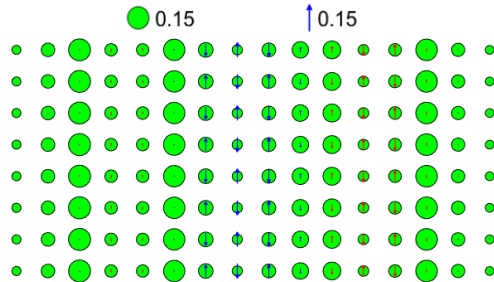


Figure 2.16: A W3 striped phase with a defect.

Figure 2.16 shows a W3 striped phase on width 8, where changing the doping has produced a defect. Each of the four stripes shown has two holes, but the overall length of the cylinder is too long for a perfect W3 configuration. In the figure, the third stripe from the left has increased its width and the ladder in between it and the second stripe has increased to width 3. The width-3 region shows longer spin-spin correlations, as expected.

2.10 Comparison to the cuprates

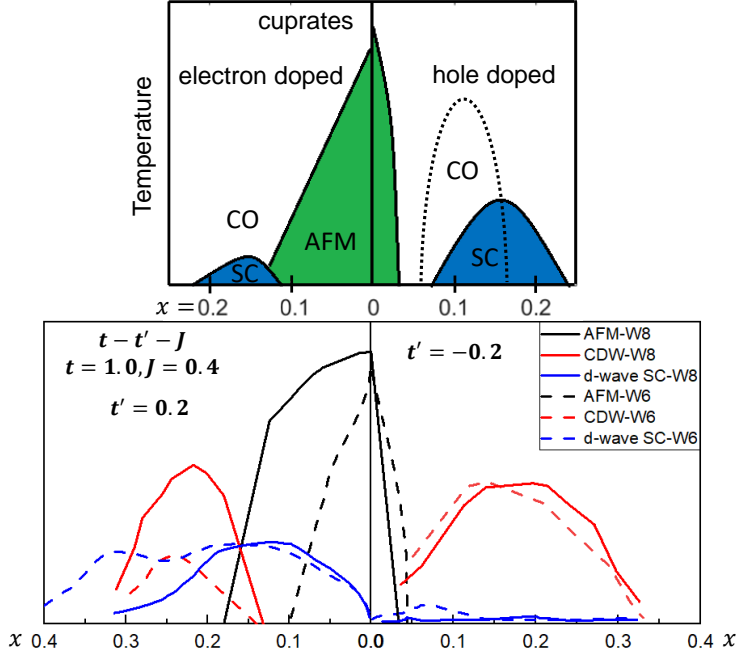


Figure 2.17: Upper panel: Experimental phase diagram of a typical cuprate superconductor, following[4], with antiferromagnetic(AFM), charge ordered(CO) and superconducting(SC) phases. The vertical axis is temperature and horizontal axis indicates electron doping (left side) and hole doping (right side). Lower panel: Antiferromagnetic, superconducting and charge-density wave order parameters at zero temperature in the t - t' - J model from DMRG calculations. Solid lines are for width-8(W8) cylinders and dashed lines are for width-6(W6) cylinders.

To test the applicability of our model to cuprates, we first look at the momentum distribution function $n(\vec{k})$ by measuring the single-particle Green's function in real space and Fourier transforming it. The results are shown in in Fig. 2.18. Both cases are for a fermion doping of $x \approx 0.125$ of the t - t' - J model. In the left figure with $t' = -0.2$, x represents the hole doping and $n(\vec{k})$ is the momentum occupation of the electrons for a hole doped system with $n = 1 - x \sim 0.875$ electrons per site. This Fermi surface is similar to what is seen in the hole-doped cuprates. In the right part of Fig. 2.18 with $t' = 0.2$, the fermions occupy a circular region centered at the origin. Under a particle-hole transformation, \vec{k} is shifted by (π, π) and these fermions represent holes in a region centered about (π, π) . In this case, the

system is electron doped with $n = 1 + x \sim 1.125$ electrons per site, and has a Fermi surface that is similar to what is seen in the electron-doped cuprates.

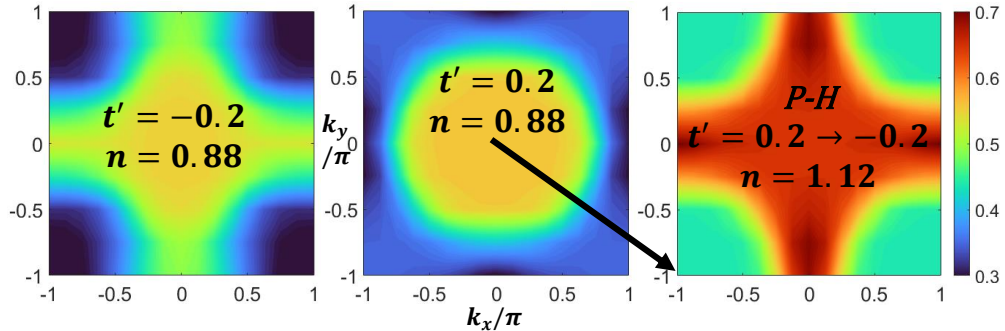


Figure 2.18: Momentum space occupancy $n(\vec{k})$ for a single spin in the width-8 cylinder. The left figure shows $n(\vec{k})$ for the fermions in the t - t' - J model with $t' = -0.2$ and $n=0.88$ fermions per site. This corresponds to the momentum distribution for the electrons in a hole doped system. The center figure shows the momentum distribution of the fermions in the t - t' - J model with $n=0.88$ fermions per site and $t' = 0.2$. Under a particle-hole transformation, which includes a (π, π) shift of the origin, one obtains the figure on the right. Here $n(\vec{k})$ represents the momentum occupation of the electrons for an electron doped system with $t' = -0.2$ and $n=1.12$ electrons per site.

If we collect the antiferromagnetic (AFM), charge ordered (CO) and superconductivity (SC) pairing from the various scans with $t' = 0.2$ and $t' = -0.2$, we can construct a zero-temperature order parameter diagram as shown in the lower panel of Fig. 2.17. This can be compared to the nominal cuprates phase diagram in the upper panel taken from [4], where here the vertical axis is temperature. We see several similarities: a much broader AFM dome on the electron doped side than the hole doped side and a charge ordered region at intermediate doping on both sides. However, contrary to the cuprate phase diagram, the SC pairing is significantly suppressed on the hole doped side with $t' = -0.2$, whereas in the hole doped cuprates there is a broad SC dome. Moreover, on the electron doped side with $t' = 0.2$, we find that the t - t' - J model exhibits a broad range of doping over which there is coexisting AFM, d -wave SC and π -triplet- p -wave SC order, contrary to what is observed in the cuprate phase diagram.

In this paper we have set $J = 0.4$. However, for $J = 1/3$ we have checked four key points in the phase diagram, and find the same four phases: the AFM- $d/\pi p$ phase at low electron doping ($t' = 0.2, x = 0.0625$), the stripes with pairing at high electron doping ($t' = 0.2, x = 0.19$), the W3 stripe phase at low hole doping ($t' = -0.2, x = 0.0833$), and the conventional stripe without pairing phase at high hole doping ($t' = -0.2, x = 0.19$).

Thus we conclude that one must go beyond the t - t' - J model to understand superconductivity in the cuprates. This immediately suggests an important question: would a Hubbard model with t' do better? In renormalizing away the two particle states to go from the Hubbard to the t - t' - J model, there are terms that are of the same order as J that are omitted[121]. It could be that these terms are important for representing the physics of the cuprates. Alternatively, it may be that other interactions are needed to represent superconductivity properly.

2.11 Inclusion of the third nearest neighbor hopping t''

The first thing we checked that beyond the t - t' - J model is the inclusion of the third nearest neighbor hopping t'' , which is thought to be roughly the same size as t' in the cuprates [5–8]. For the case of the hole-doped cuprates, it reflects the extended nature of the orthogonalized Zhang-Rice singlet [122] of the 3-band CuO_2 model [121]. Can the addition of t'' fix the discrepancy?

We use DMRG to investigate pairing properties of the t - t' - t'' - J model at a doping level $x \approx 0.1$. Our main conclusion is that t'' does not resolve the discrepancy. As shown in Fig. 2.19, we find that the parameters used for the electron-doped cuprates ($t' > 0, t'' < 0$) enhance superconductivity, both individually and in combination. However the ones used for the hole-doped cuprates ($t' < 0, t'' > 0$) suppress it. In most of the region with pairing

there is coexisting antiferromagnetic (AFM) order and uniform electron/hole density, i.e. an absence of charge stripes. These results imply that the extended t - t' - t'' - J model fails to capture the superconducting phase of the hole-doped cuprates.

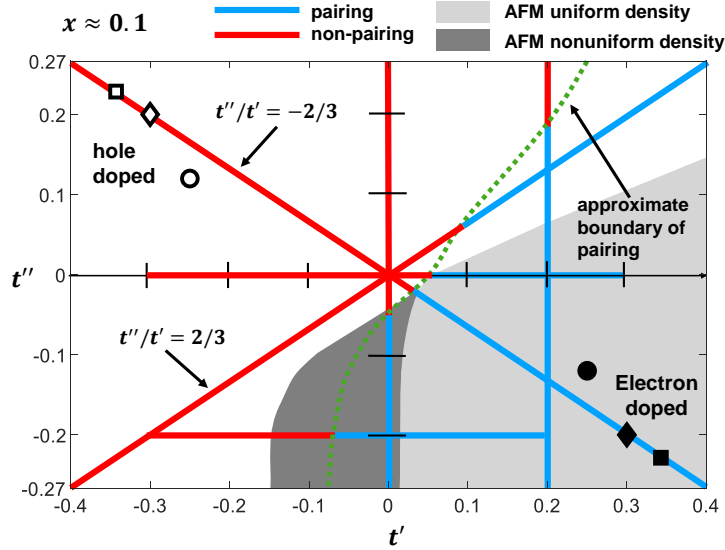


Figure 2.19: An approximate phase diagram in the $t' - t''$ plane at doping $x \approx 0.1$. The lines are “scans” with the blue/red color denoting the parameter range with/without pairing. The dotted green line shows the extrapolated pairing phase boundary based on the scans. The light/dark gray regions have AFM order with uniform/nonuniform hole density while the white background is striped. Square [5], diamond [6, 7] and circle [8] markers indicate the (t', t'') values proposed in several studies with solid markers for electron doped systems and hollow markers for hole doped systems.

2.12 Summary

In summary, we have carried out large scale ground state DMRG calculations for the extended t - J cylinders with width six and eight which approximate the behavior of 2D systems. We have established an approximate phase diagram for this model.

In the parameter region that corresponds to electron doped cuprates, at low doping we find an AFM- $d/\pi p$ phase with coexisting uniform AFM and strong d -wave singlet pairing. As a result of these two orders, there also exists (π, π) , p -wave triplet pairing. Pairing in

this electron low-doped region is strong and unambiguous. At higher doping there is a striped phase with relatively weaker d -wave singlet pairing, as well as triplet pairing with an amplitude modulated by the stripes.

In the parameter region corresponding to hole doped cuprates, there is a broad striped phase. States with pairing go from being meta-stable and only slightly higher in energy near $t' = 0$ to significantly suppressed with $t' = -0.2$. At low doping, near $x = 0.08$, we find a novel width-3 stripe phase that has chains of unpaired holes separated by two-leg spin ladders. The hole chains behave like 1D t - J chains while spins on two-leg ladders mimic the short-ranged spin correlations seen in two-leg Heisenberg ladders. For $t' < 0$, AFM order only exists for a very narrow doping range near half-filling.

Despite the fact that the extended t - J model manages to capture several aspects of the electron and hole-doped cuprates, including the broad AFM dome on the electron side and a much more narrow one on the hole side, as well as charge order on both sides, the superconducting properties exhibit significant discrepancies with respect to the cuprates. The hole doped cuprates exhibit strong superconductivity while the corresponding region of the model does not. In contrast, for the electron doped region of the model we find strong superconductivity over a broader doping range than in the cuprates, and for a substantial range of doping this pairing coexists with AFM and triplet p -wave superconductivity.

Note added. After the publication of this paper [10], there have been other studies on the ground state phase diagram of both the t - t' - J model and the t - t' Hubbard model [28, 66, 123, 124]. While studies have converged regarding the existence of superconductivity on the electron-doped side, superconductivity on the hole-doped side appears to be more complicated.

Chapter 3

DMRG-based downfolding of the three-band Hubbard model:

Importance of density-assisted hopping

3.1 Introduction

What is the minimal model that captures the important physics of the high-temperature cuprate superconductors? This has been a central question ever since the discovery of the cuprates. It has been argued that the single-band Hubbard and t - J models, in their simplest forms, are sufficient to describe the physics of high T_c superconductivity. Unexpectedly, recent numerical simulations find that superconductivity in the ground state of these single-band models appears to be quite delicate. For example, in the pure Hubbard and t - J models ($t', t'' = 0$), superconductivity is found to be absent [10, 27]. While the presence

of a $t' > 0$ can induce superconductivity [10, 123–127], this corresponds to electron doping and the question regarding the presence of hole-doped superconductivity ($t' < 0$) is not completely resolved [10, 28, 123, 124, 126]. The greatest delicacy appears to be associated with the superconductivity; other aspects of the models, including antiferromagnetism (AFM) as well as intertwined spin and charge order, appear to be in qualitative agreement with the cuprates [10, 11, 72, 75, 128–131].

This subtleness of pairing in the single-band models calls for a re-examination of the downfolding process used to derive them, since modest errors could have significant effects. This downfolding is a two-step process, where first one constructs from density functional methods the intermediate-level three-band Hubbard (or Emery) model [132], which includes Cu $d_{x^2-y^2}$, O p_x and O p_y orbitals. Since the three-band model is closer to an all-electron Hamiltonian of the cuprates, one expects it to be more reliable than a one-band model—but also more difficult to simulate. There is evidence that the three-band model captures various aspects of the cuprates, particularly magnetic and charge density wave properties [133–140], with greater uncertainty about the pairing properties. To downfold to a single band model, Zhang and Rice argued that holes on oxygen sites bind to holes on copper sites to form local singlets [122]. The Zhang-Rice singlet picture has gained support from experiments [141–143] as well as calculations [134, 135, 144, 145], and motivated studies of various single-band Hubbard [70, 74, 79, 80, 83, 86, 87, 92, 100, 101, 112, 123, 146–153] and t - J models [11, 76, 78, 81, 82, 99, 125, 127, 154–156].

Here we demonstrate an alternative way to downfold the three-band Hubbard model based on a density-matrix renormalization group (DMRG) [29] construction of Cu-centered Wannier functions. The general idea of constructing effective models using *ab initio* calculations has been explored in various contexts [157–161]. Our approach uses DMRG to compute the natural orbitals of the three-band model, and from those construct Wannier functions, similar to a recent work that downfolds hydrogen chains into Hubbard-like models [162]. The

resulting single-band model includes additional two-site density-assisted hopping terms t_n whose magnitude is comparable to t . On a mean-field level, these new terms simply reduce the ratio U/t_{eff} , with $t_{\text{eff}} = t + t_n \langle n \rangle$, where $\langle n \rangle$ is the average number of holes per CuO_2 unit cell. However, beyond mean-field, the t_n terms capture the doping-asymmetric carrier mobility, and, as revealed by a measurement of the superconducting phase stiffness, further enhance the pairing in the hole-doped single-band model.

3.2 The three-band Hubbard model

We present the lattice structure and the terms in the three-band Hubbard model in Fig. 3.1(a). Each CuO_2 unit cell consists of three orbitals: Cu $d_{x^2-y^2}$, O p_x and O p_y . We study clusters with cylindrical boundary conditions. For an L_x by L_y cylinder, there are $N_{\text{Cu}}=L_x L_y$ Cu sites and $N_{\text{O}}=(2L_x + 1)L_y$ O sites. In the undoped insulator at half-filling, there is one hole per unit cell, and the model is written in the hole picture with $d_{i\sigma}^\dagger$ or $p_{j\sigma}^\dagger$ creating a hole with spin σ on a Cu site i or O site j . Hole doping corresponds to $\langle n \rangle > 1$ while electron doping corresponds to $\langle n \rangle < 1$. The three-band Hamiltonian is:

$$\begin{aligned}
H^{TB} = & -t_{pd} \sum_{\langle ij \rangle \sigma} (d_{i\sigma}^\dagger p_{j\sigma} + h.c.) - t_{pp} \sum_{\langle\langle ij \rangle\rangle \sigma} (p_{i\sigma}^\dagger p_{j\sigma} + h.c.) \\
& + U_d \sum_i n_{i\uparrow}^d n_{i\downarrow}^d + U_p \sum_i n_{i\uparrow}^p n_{i\downarrow}^p + \Delta_{pd} \sum_{i\sigma} p_{i\sigma}^\dagger p_{i\sigma}
\end{aligned} \tag{3.1}$$

where t_{pd}/t_{pp} hops a hole between nearest-neighbor Cu-O/O-O sites, and the summation $\langle ij \rangle / \langle\langle ij \rangle\rangle$ runs over all relevant pairs of sites. We have chosen a gauge for the orbitals as shown in Fig. 3.1(a) so that all hoppings are negative; U_d and U_p are the on-site repulsion term on the Cu and O sites; $\Delta_{pd} = \epsilon_p - \epsilon_d$ is the energy difference for occupying an O site compared to occupying a Cu site. We set the energy scale with $t_{pd} = 1.0$, and take $t_{pp} = 0.5$, $U_d = 6.0$, $U_p = 3.0$, and $\Delta_{pd} = 3.5$, unless otherwise noted, which appropriately describes

a charge-transfer system where $U_d > \Delta_{pd}$ and $\Delta_{pd} > 2t_{pd}$. Estimates for t_{pd} range from 1.1eV [163] to 1.5eV [164]. Comparing with previously used parameters [137, 164], here we increase Δ_{pd} to incorporate the effect of V_{pd} , and choose a somewhat smaller U_d for a stronger pairing response (see Appendix. B). Systems **h1** and **e1** have hole and electron dopings of 0.15. Another hole-doped case **h2** with $U_d=3.5$ and $\Delta_{pd}=5.0$ describes a Mott-Hubbard rather than charge-transfer system ¹. The calculations are carried out using the ITensor library [108]. We typically perform around 20 sweeps and keep a maximum bond dimension of 7000 to ensure convergence with a maximum truncation error of $\mathcal{O}(10^{-5})$.

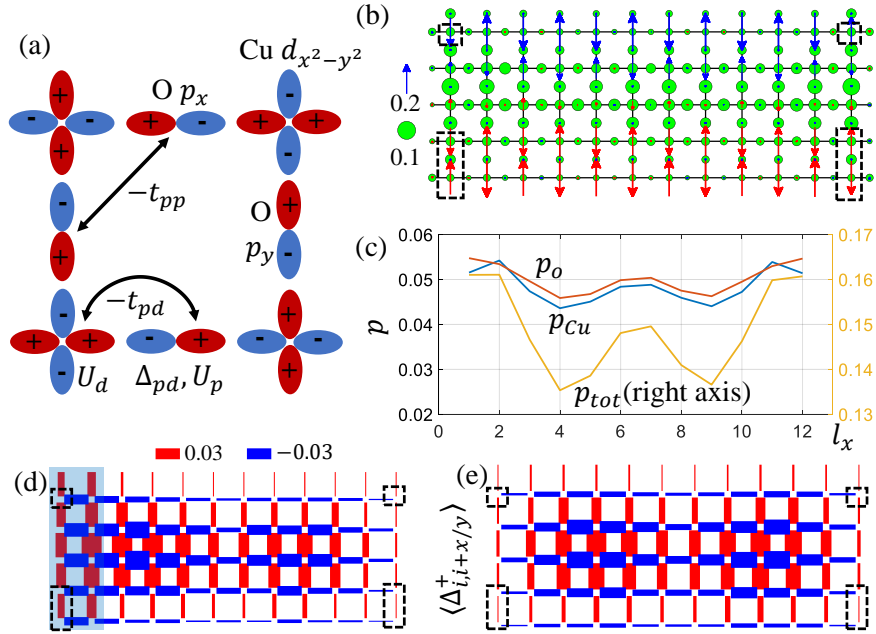


Figure 3.1: (a): The three-band Hubbard model and our phase convention for the orbital basis. (b): Charge and spin structure on a 12×5 cylinder at a hole doping ~ 0.15 . The length of the arrows and the diameter of the circles represent $\langle S^z \rangle$ and local doping, respectively. The spins are colored to indicate different AFM domains. There are weak magnetic pinning fields applied on the boundary sites in the dotted boxes. (c): Average orbital-resolved local doping $p_{\text{Cu/O}}$ along the length of the cylinder with $p_{\text{tot}} = p_{\text{Cu}} + 2p_{\text{O}}$ (d) and (e): Pairing order $\langle \Delta_{ij}^\dagger + \Delta_{ij} \rangle$ between neighboring Cu sites i and j . The thickness/color of the bond indicates the magnitude/sign of the pairing. The pairing orders away from the edges are similar for (d) which has pairfields applied on the shaded left edge and (e) which spontaneously breaks symmetry.

¹See Ref.[165] for detailed definitions of a charge-transfer insulator and Mott-Hubbard insulator.

Previous studies of the three-band model have identified features consistent with the cuprates, including doping asymmetry, formation of stripes on the hole doped side and commensurate AFM on the electron-doped side [136, 137]. There is evidence for d -wave pairing for both electron and hole doping, with the dominant component between nearest neighbor Cu sites [134, 135, 139, 166, 167].

Of particular concern for finite size effects is the quantization of stripe filling around a short cylinder [137]; here we choose a width-5 cylinder so that one stripe can form lengthwise; see Fig. 3.1(b). The Cu-Cu pairing is shown in Fig. 3.1(e). Along the stripe an additional pairing modulation reflects an edge-induced charge density oscillation, as shown in Fig. 3.1(c). Similar pairing occurs whether it is pinned by edge pair fields [Fig. 3.1(d)] or allowed to arise spontaneously as a finite bond dimension broken symmetry [10] [Fig. 3.1(e)]. The existence of pairing for a hole-doped three-band model has also been reported in a recent infinite projected entangled-pair states study [168].

3.3 Downfolding into a Wannier single-band model

The occupied bands in the DMRG wavefunctions are identified by measuring the single-particle correlation matrix $M_{\alpha\beta} = \sum_{\sigma} \langle C_{\alpha\sigma}^{\dagger} C_{\beta\sigma} \rangle$, with $\{C^{\dagger}\} = \{d^{\dagger}, p_x^{\dagger}, p_y^{\dagger}\}$, whose eigenvectors and eigenvalues define the natural orbitals (NOs) and their occupancies, respectively. In a non-interacting system, the NO occupancies make a step function at the Fermi level. Here, this step near $i \sim 35$ is completely smeared out [Fig. 3.2(a)], reflecting the strong correlation in the system. However, there is a sharp drop in occupancies at $i = 60$, the total number of Cu sites, indicating the end of the first band. Beyond the first band, the total occupancy is $< 2\%$, and for the electron doped case, $< 0.4\%$. This provides a strong justification for downfolding into a single-band, which would be exact if the higher-band occupancies were zero. We observe similar sharp drop-offs for narrower width 2 and 4 systems. This indicates

that the drop-off is due to short-range physics involving the Cu and surrounding O orbitals, which can be seen clearly on small systems. We observe a similar sharp drop-off for a range of three-band parameters, including in the Mott-Hubbard regime.

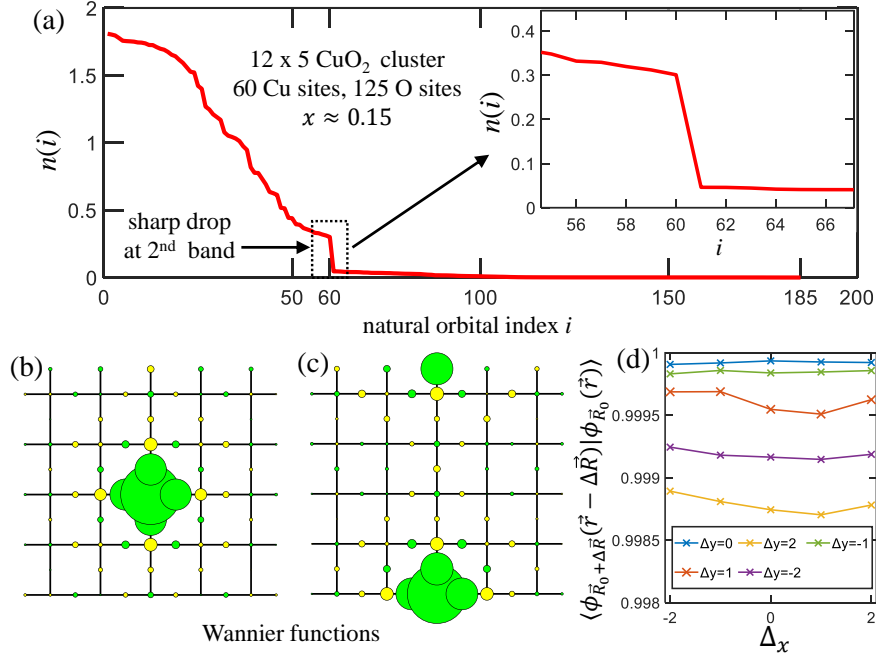


Figure 3.2: At a hole doping of 0.15 (a): occupancies of the natural orbitals obtained by diagonalizing the single-particle correlation matrix $M_{\alpha\beta} = \sum_{\sigma} \langle C_{\alpha\sigma}^{\dagger} C_{\beta\sigma} \rangle$, with $C^{\dagger} = \{d^{\dagger}, p_x^{\dagger}, p_y^{\dagger}\}$. The natural orbital states/occupancies correspond to the eigenvectors/eigenvalues of $M_{\alpha\beta}$. The inset is a zoom-in of the region that shows a sharp drop at the second band beyond which occupancies are limited ($< 2\%$). (b) and (c): Cu-centered Wannier functions at two different locations constructed from the natural orbitals of the first band. Color/area of the circles indicate the sign/magnitude of the local orbital component. (e): overlap of Wannier functions (truncated to a 5×5 CuO_2 unit cell) with their centers shifted to the same site, showing they are almost translational invariant.

Given the accuracy of the truncation to a single band, we can derive an effective single-band model through the standard Wannier construction with a simple single-particle transformation. We first localize the functions of this band into Cu-centered Wannier functions (WFs).

Our construction of the Wannier functions and subsequent downfolding is patterned after Ref. [162], with the key difference being that in our study we start with a three band model rather than a continuum all electron calculation described by sliced basis functions.

The goal is to form Wannier functions centered at Cu site j $\{\phi_j(\vec{r})\}$ by linearly combining the natural orbitals of the first-band $\{\psi_i(\vec{r})\}$, with both i and j ranging from 1 to the total number of Cu sites. We would like the Wannier functions to be: (1) orthonormal, (2) translationally invariant, and (3) localized around Cu sites. These properties ensure the downfolded Wannier Hamiltonian has short-ranged interactions with site-independent magnitudes. While the translational invariance cannot be completely achieved because we are dealing with cylindrical systems with open edges, we expect the Wannier functions in the bulk to almost satisfy the above properties.

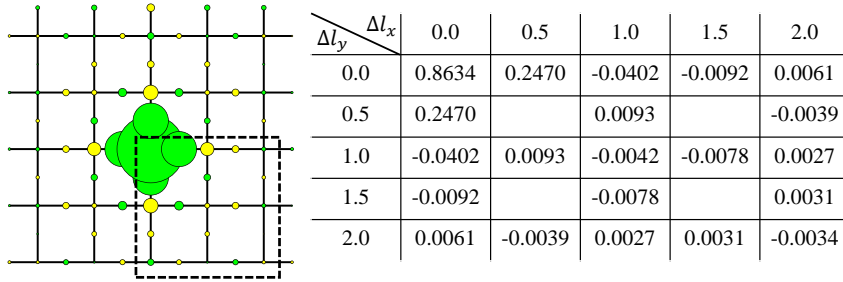


Figure 3.3: A Cu-centered Wannier function with the color/area of the circles denoting the sign/magnitude of the local orbital components. The coefficients of the orbitals in the lower-right quadrant are shown in the table, which have been averaged over the vertical and horizontal directions. The Wannier function here is from downfolding the case **h1** in the main text.

First we construct functions $\{\delta_j(\vec{r})\}$ localized around each Cu site j by superposing the natural orbitals $\{\psi_i\}$ with coefficients being their respective weight on Cu site j :

$$\delta_j(\vec{r}) = \sum_i \psi_i(\vec{r} = \vec{r}_j) \psi_i(\vec{r}) \quad (3.2)$$

where \vec{r}_j is the position vector corresponding to Cu site j . The functions $\{\delta_j(\vec{r})\}$ are localized, but not orthonormal. We orthonormalize them while preserving their locality using Löwdin symmetric orthogonalization [169], which minimally orthonormalizes these functions (note

O is a matrix):

$$\phi_j(\vec{r}) = \sum_{j'} [O^{-\frac{1}{2}}]_{jj'} \delta_{j'}(\vec{r}), \quad (3.3)$$

with $O_{jj'} = \langle \delta_j(\vec{r}) | \delta_{j'}(\vec{r}) \rangle$.

The resulting Wannier functions $\{\phi_j(\vec{r})\}$ are guaranteed to be orthonormal and are almost translational invariant, as we show in Fig. 2(e) in the main text. We plot the structure of the resulting Wannier function in Fig. 3.3. It is localized around one Cu site with its tail decaying rapidly with the distance away from the center Cu site. Due to the width-5 cylinder used, there are differences between the coefficient of orbitals in vertical and horizontal directions at long distance. While we do not further modify the Wannier functions, so as to preserve orthonormality, we do later average the terms over the two directions in the downfolded Hamiltonian.

We show two representative WFs in Fig. 3.2(b) and (c), which are evidently highly localized. Functions on different sites are almost identical; evidence for this translational invariance is shown in Fig. 3.2(d).

To construct the effective Hamiltonian in the WF space, we first organize the WFs into a N_{Cu} -by- $(N_{\text{Cu}} + N_{\text{O}})$ real isometric matrix \mathbf{A} ($\mathbf{A}\mathbf{A}^\dagger = \mathbf{1}$), with entry A_{ij} being the weight of the three-band orbital j in the Wannier function centered at Cu site i (The matrix elements of \mathbf{A} are listed in Fig. 3.3). The matrix \mathbf{A} defines a single-particle transformation from the three-band basis $\{C^\dagger\} = \{d^\dagger, p_x^\dagger, p_y^\dagger\}$ to the WF basis $\{c^\dagger\}$:

$$c_i^\dagger = \sum_j A_{ij} C_j^\dagger \quad (3.4)$$

We invert this relationship, taking:

$$C_j^\dagger = \sum_i A_{ij} c_i^\dagger + \text{higher bands} \quad (3.5)$$

where we omit the higher bands. The Wannier Hamiltonian is obtained by inserting Eq. 3.5 into the three-band Hamiltonian [Eq. 3.1]. The single-particle terms $k_{\alpha\beta}$, which include the t_{pd} , t_{pp} and Δ_{pd} terms, become

$$k_{\alpha\beta} C_{\alpha\sigma}^\dagger C_{\beta\sigma} \rightarrow k_{\alpha\beta} \sum_{ij} A_{i\alpha} A_{j\beta} c_{i\sigma}^\dagger c_{j\sigma}. \quad (3.6)$$

The two-particle terms U_α , which include the U_d and U_p terms, become

$$U_\alpha n_{\alpha\uparrow} n_{\alpha\downarrow} \rightarrow U_\alpha \sum_{ijkl} A_{i\alpha} A_{j\alpha} A_{k\alpha} A_{l\alpha} c_{i\uparrow}^\dagger c_{j\uparrow}^\dagger c_{k\downarrow}^\dagger c_{l\downarrow}. \quad (3.7)$$

Although the Wannier Hamiltonian has $\mathcal{O}(N^2)$ single particle and $\mathcal{O}(N^4)$ two particle terms, both the single-particle and two-particle terms decay quickly with the distance between sites. Magnitudes of the single-particle hoppings beyond third-nearest neighbors are smaller than $0.01t$ and are truncated. The largest two-particle term is the onsite repulsion U . The second largest is the nearest-neighbor density-assisted hopping $t_n c_{j,\sigma}^\dagger c_{i,\sigma} n_{i\bar{\sigma}}$. We also keep the second and third nearest-neighbor density-assisted hoppings (t'_n and t''_n). All other two-particle terms are less than $0.05t$ and are truncated. After these simplifications, we obtain a *truncated Wannier model*:

$$\begin{aligned} H = & \sum_{i,\delta,\sigma} -t^\delta c_{i+\delta,\sigma}^\dagger c_{i,\sigma} + \sum_i U n_{i,\uparrow} n_{i,\downarrow} \\ & + \sum_{i,\delta_i,\sigma} -t_n^\delta (c_{i+\delta,\sigma}^\dagger c_{i,\sigma} + c_{i,\sigma}^\dagger c_{i+\delta,\sigma}) n_{i\bar{\sigma}}. \end{aligned} \quad (3.8)$$

Here $i + \delta$ is the first, second, or third nearest neighbor of site i , with conventional hopping amplitudes t , t' , and t'' , and with density-assisted hopping amplitudes t_n, t'_n, t''_n . The resulting model parameters are summarized in Table. 3.1 for downfolding based on three different three-band systems ².

Table 3.1: Parameters for the Wannier single-band model from downfolding the three-band model. **h** and **e** correspond to hole and electron doping of 0.15. t_{pd} is nominally 1.5eV.

case (U_d, Δ_{pd})	t/t_{pd}	t_n/t	t'/t	t'_n/t	t''/t	t''_n/t	U/t
h1 (6.0, 3.5)	0.27	0.60	0.07	0.05	-0.04	-0.09	12.6
e1 (6.0, 3.5)	0.28	0.52	0.08	0.08	-0.05	-0.04	13.7
h2 (3.5, 5.0)	0.21	0.33	0.08	0.05	-0.03	-0.04	11.8

Note that the nearest-neighbor t_n coefficients are almost twice the size of an effective exchange coupling $J \sim 4t^2/U \sim 0.32$. Given their substantial magnitude, it is surprising how rarely these terms have been considered [170–173]. The existence of the t_n term is guaranteed by a finite component of the nearest-neighbor Cu orbitals in the Wannier function, which is robust since regular Wannier functions must have those components to satisfy orthogonality. Its magnitude is substantial mainly because of the large value of U_d . The t_n term is much larger for the cuprate-relevant charge-transfer case **h1**, compared with the Mott-Hubbard case **h2** that has a similar U/t ratio. This is directly tied to the higher O-occupancy in the charge-transfer case, which makes the WFs more extended.

We also note that the WFs and thus the model parameters are similar for the hole and electron doped cases, even if their parental three-band states are quite different in spin and charge order, indicating that the downfolding is determined by the local physics. Just as the sharp drop in occupancy after the first band shows little dependence on system size, we find the Wannier Hamiltonian also exhibits little dependence on cluster size.

Two key questions now arise: (1) does the Wannier model Hamiltonian give the same properties as the three band model? Given the straightforward and robust nature of our down-

²The hopping coefficients are averaged over horizontal and vertical directions, which typically differ by $\sim 10\%$, but somewhat more (-0.07 and -0.11) in the case of t''_n in system **h1**.

folding, we expect this to be so, and comparisons detailed in Appendix. B for moderate system sizes support this. (2) Does a mean-field treatment of the t_n terms, reducing the system to a standard Hubbard model, also match the properties of the three-band model? Although this may be largely true for the spin and charge degrees of freedom, we will argue that the delicate nature of the pairing is not correctly captured by the mean field/standard Hubbard treatment. In any case, the large magnitude of t_n poses a potential difficulty for a mean-field treatment since any deviations could be significant.

3.4 Effects of t_n

We find that the t_n terms have two primary effects: first, they reduce the effective interaction strength U/t_{eff} ; and second, they enhance hole hopping, reducing the effective mass of pairs on the hole-doped side and promoting phase coherence. The reduction of U/t_{eff} can be understood from a mean-field treatment of t_n where one replaces $t_n c_{j\sigma}^\dagger c_{i\sigma} (n_{i\bar{\sigma}} + n_{j\bar{\sigma}})$ by $t_n c_{j\sigma}^\dagger c_{i\sigma} \langle n \rangle$, with $\langle n \rangle$ being the average density of holes per Cu site, adding to the conventional hopping. This changes $U/t \sim 13$ to $U/t_{\text{eff}} \sim 7.5$ (for $t_n=0.6$, $n=1.15$), close to $U/t = 8$, which is often used for the cuprates.

Beyond mean-field, we consider specific hopping processes in Fig. 3.4(a-c), written in the hole-picture. For a doped hole (i.e. a doublon) we expect process (a) to be relevant, where the t_n acts with magnitude $2t_n$. For undoped regions with AF particle-hole virtual hoppings, process (b) acts with magnitude t_n . On the electron doped side, process (c), t_n has no effect. It does not seem possible to capture these various properties correctly with a mean field treatment.

We find that the resulting hole-pair mobility is enhanced with the $t_n c_{j,\sigma}^\dagger c_{i,\sigma} n_{i\bar{\sigma}}$ term versus its mean-field $t_n c_{j,\sigma}^\dagger c_{i,\sigma} \langle n_{i\bar{\sigma}} \rangle$, $2.75t$ versus $2.27t$. In contrast, the mobility of a pair of electrons

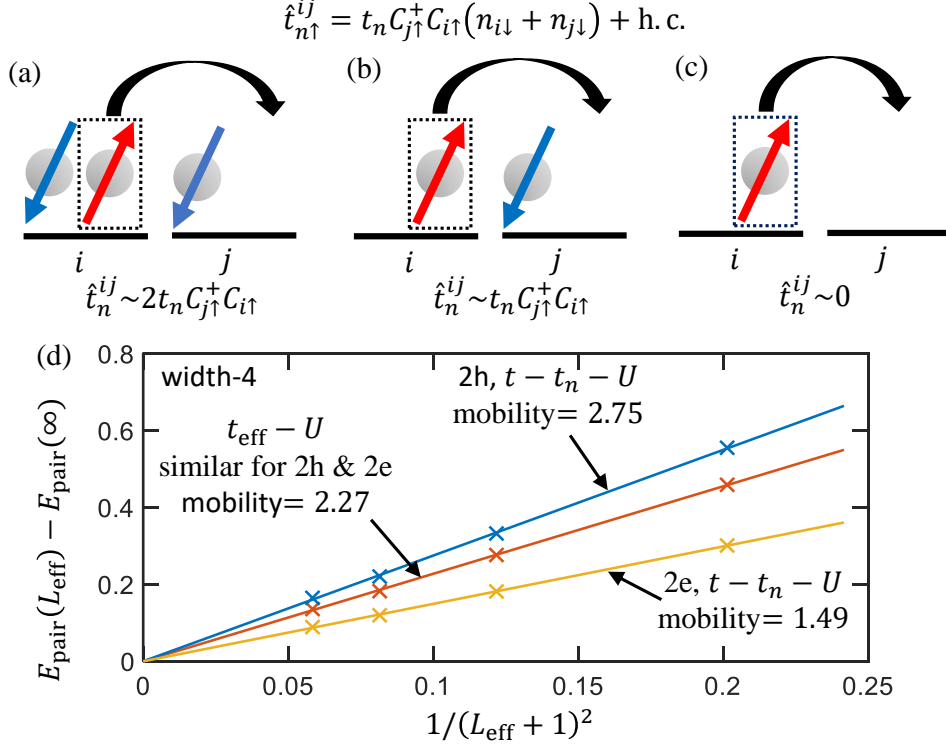


Figure 3.4: (a),(b) and (c): action of the t_n term, and resulting hopping strengths, depending on the occupations of the sites involved. (d) On a width-4 cylinder, mobility of a pair of holes/electrons (in unit of t) measured by the slope of pair energy versus $1/(L_{\text{eff}} + 1)^2$, for the $t-t_n-U$ model and the $t_{\text{eff}}-U$ model.

with t_n is much smaller, $1.49t$, and reduced comparing to its mean-field $2.27t$. Thus, the increased mobility of a single pair hints at the possibility of enhanced pairing due to t_n on the hole doped side.

To probe for superconductivity, we apply edge pairfields to a 10×4 cylinder with and without a π phase shift between the two edges, to measure the superconducting phase stiffness α . The results are shown in Fig. 3.5. Note that $\alpha = 0$ indicates the absence of superconductivity. The applied fields make α proportional to an energy difference, $\alpha \propto \frac{L_x}{L_y} \Delta E$, where ΔE can be extrapolated using DMRG. At a hole doping of 0.11 ($\langle n \rangle \approx 1.11$), the $t-t_n-U$ model gives a stiffness α that is five times larger than the $t_{\text{eff}}-U$ model³. The pure Hubbard model (without t' terms) is thought to be non-superconducting [27]; our results hint that the t_n

³In Appendix. B, we vary t_n from 0 to 1.6 and find that the superconducting phase stiffness gets bigger as t_n increases, and the phase stiffness is greater compared to using a mean-field t_{eff} .

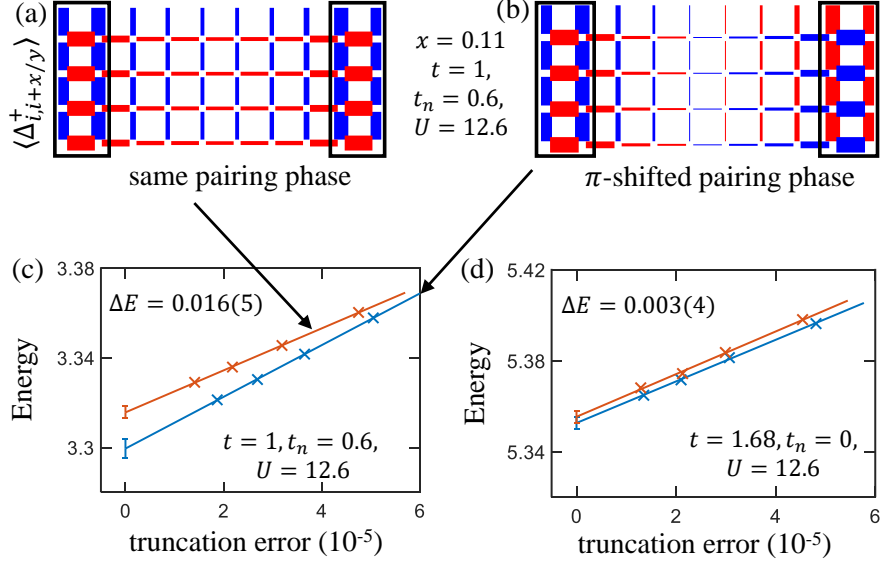


Figure 3.5: Pairing response for the t - t_n - U model in a 10×4 cylinder at a hole doping ~ 0.11 ($n \approx 1.11$). Pair-fields have been applied to regions near both edges, denoted by the black boxes, with the phases on the two ends (a) being the same and (b) having a π shift. (c): extrapolation of the energies with the truncation errors for the two different pairfield boundary conditions in (a) and (b). The energy difference is a measurement of the superconducting phase stiffness. (d) Same as (c) for the $t_{\text{eff}}-U$ model that incorporates the effect of the t_n term only in mean-field.

terms, even without t' , might tip the balance towards superconductivity. In a more realistic model where t' and t'_n from Table. 3.1 are included, we also find a larger phase stiffness, $\Delta E = 0.012(4)$ with t_n versus $0.002(4)$ with t_{eff} , for a system at a hole doping of 0.11.

3.5 Summary and discussion

We have revisited the Zhang-Rice downfolding of the three-band Hubbard model to a single-band model, basing the downfolding on a DMRG simulation of the three band model. Our results give strong support to the applicability of the one band approach, where the small occupancy of higher natural orbital bands shows their irrelevance. However, our Wannier function downfolding also shows that a density-assisted hopping term which is usually neglected has a large coefficient. This term renormalizes the hopping in mean field, but mean

field treatments are inadequate to capture the effects of this term on pairing. The density-assisted hopping enhances hole mobility and hole-pair mobility. This leads to enhanced superconducting pairing on the hole-doped side on width-4 cylinders.

Our results do not *imply* that the t_n term is necessary for superconductivity—but it clearly seems to help, and is directly generated by the three-band downfolding. Recent simulations of the t - t' - U Hubbard model, combining auxiliary-field quantum Monte Carlo and DMRG and extrapolating to the thermodynamic limit, indicate that the hole-doped Hubbard model is superconducting [28]. However, the extrapolations are delicate, and it seems that this system must be close to the boundary between pairing and non-pairing phases. The addition of a t_n term may push the model well into the pairing regime, both easing the difficulties of simulating the model, and improving its applicability to the cuprates.

Chapter 4

Quantum Spin Nematic in the Square-Lattice J_1 - J_2 Ferro-antiferromagnetic Heisenberg Model

4.1 Introduction

Liquid crystals—which combine properties of a liquid and a solid that seem mutually exclusive—were considered an exotic state of matter for nearly a century before becoming ubiquitous in technology [174, 175]. Their quantum analogues have been hypothesized and pursued in several contexts, such as electronic nematic states in strongly correlated materials [176–179], spin nematics in frustrated magnets [180–190], and supersolids in He^4 and cold atomic gases [191–194]. Quantum spin nematics are particularly elusive, as they should interpolate between a magnetically ordered spin solid and a spin liquid, another exotic and elusive

state [53, 195]. Like spin liquids, spin nematics lack conventional dipolar magnetic order, but instead break spin-rotational symmetry with quadrupolar or higher-rank multipolar ordering [196–198], making their experimental detection challenging [17].

An earlier study has proposed an intuitive view of the nematic states as of the Bose-Einstein condensates (BECs) of *pairs* of spin excitations with a gap in the single-particle sector [198]. In a nutshell, a nematic state occurs if a conventional order due to a BEC of single spin flips [199] is preempted by a BEC of their pairs. Since the bound states (BSs) of magnons in ferromagnets (FMs) do not Bose-condense [200, 201], it was suggested that magnetic frustration can facilitate nematic pair-BEC [198], a concept explored in several classes of frustrated magnets theoretically [202–217] and experimentally [181–190].

One of the simplest paradigmatic models for this scenario is the J_1 – J_2 ferro-antiferromagnetic (AFM) $S=1/2$ Heisenberg model on a square lattice in external field,

$$H = J_1 \sum_{\langle ij \rangle_1} \mathbf{S}_i \cdot \mathbf{S}_j + J_2 \sum_{\langle ij \rangle_2} \mathbf{S}_i \cdot \mathbf{S}_j - h \sum_i S_i^z, \quad (4.1)$$

where $\langle ij \rangle_{1(2)}$ denotes the first (second) nearest-neighbor bonds, the field $h = g\mu_B H$, $J_1 = -1$ is set as the energy unit, and $J_2 > 0$. The FM is a ground state for small J_2 ; for large J_2 it is a stripe AFM [218]; see Fig. 4.1(a).

Prior studies on this model [202–204] have proposed the nematic state to intervene between FM and AFM phases in a broad region similar to the one shown in Fig. 4.1(a). However, this contradicts the robust numerical evidence of a direct FM-AFM transition in zero field [218], highlighting a common pitfall of claiming the nematic state based on correlations that are subsidiary to a prevalent dipolar order. It also shows that the nematic state of BEC pairs may be superseded by other instabilities.

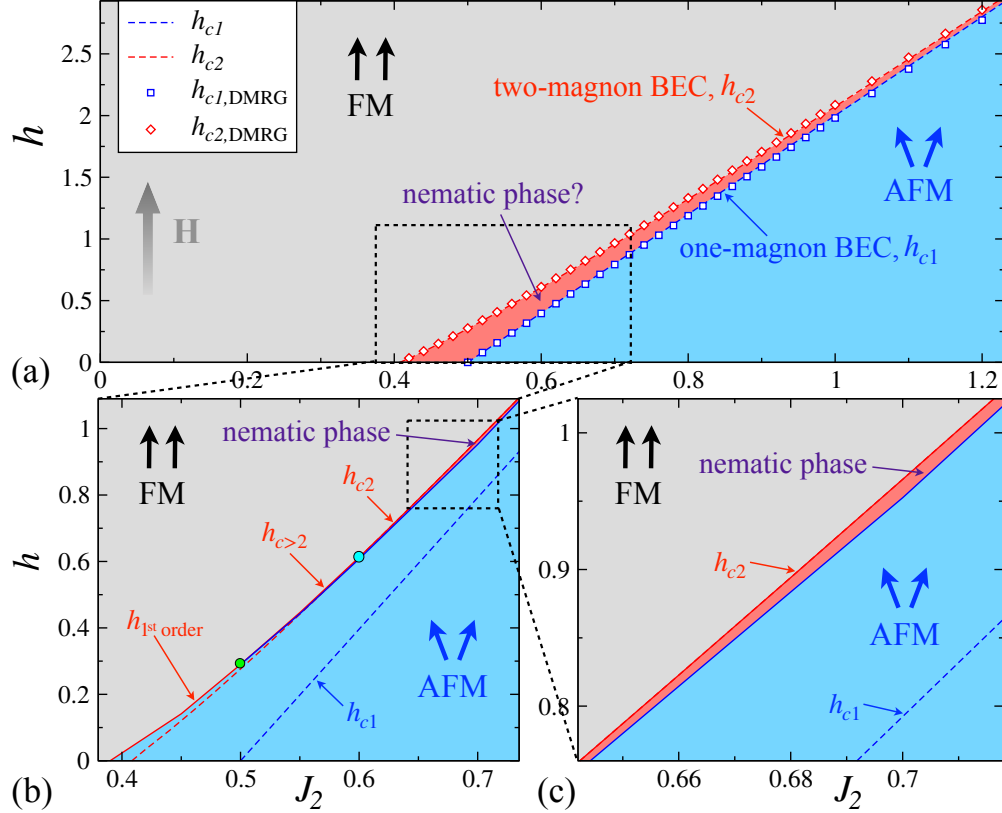


Figure 4.1: (a) The naïve h - J_2 phase diagram of model (4.1) based on the single spin-flip and pair-BEC h_{c1} and h_{c2} lines. Lines and symbols show analytical and DMRG results, respectively. (b) The actual phase diagram of the model (4.1) in the zoomed region of (a), with the first-order, multi-pair, and pair-BEC transitions emphasized. (c) The zoomed sector of (b) showing the extent of the nematic phase near pair-BEC field.

In this chapter, we combine analytical and numerical density-matrix renormalization group (DMRG) approaches to provide unambiguous conclusions on the nematic state in the J_1 - J_2 square-lattice model.

4.2 d -wave pair-BEC

Pairing is ubiquitous in physics [219, 220]. In model (4.1), the pairing of two spin flips sharing an attractive FM J_1 -link occurs in the polarized state. Since the model is 2D, one expects a BS in the s -wave channel for an arbitrarily weak attraction, or any J_2 , as in the

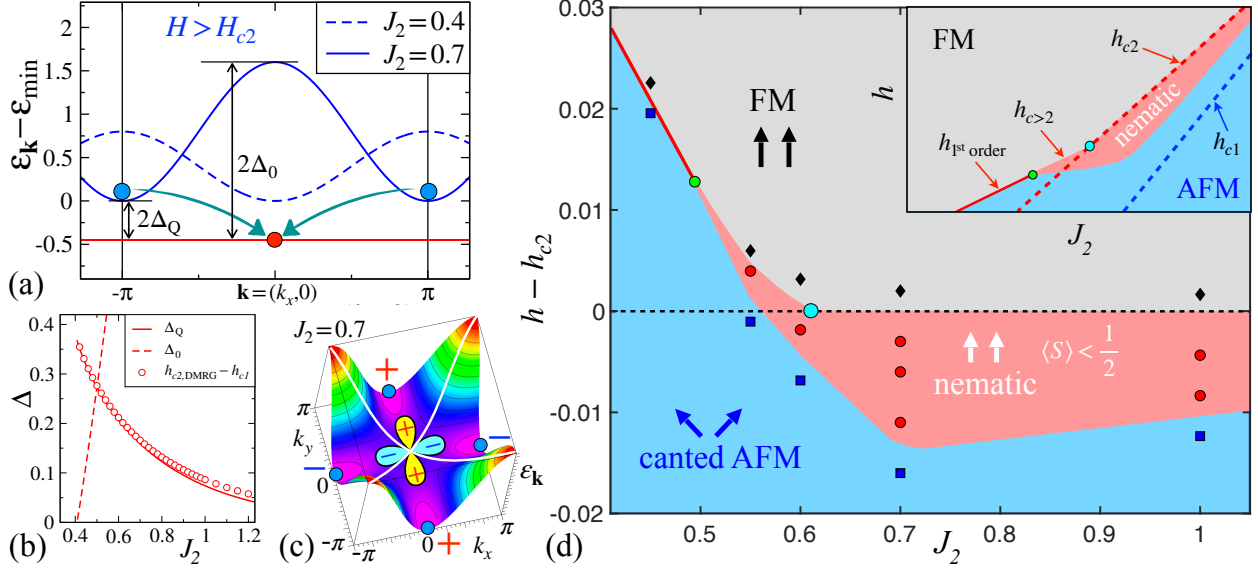


Figure 4.2: (a) Magnon energies $\varepsilon_{\mathbf{k}}$ at $h > h_{c2}$ for $J_2 = 0.7$ and 0.4 , schematics of magnon pairing, and gaps $\Delta_{\mathbf{Q}(0)}$. (b) The pairing gap Δ vs J_2 from theory (lines) and DMRG (symbols). (c) $\varepsilon_{\mathbf{k}}$ for $J_2 = 0.7$, nodes of the $d_{x^2-y^2}$ -wave harmonic (white lines), and schematics of the d -wave. (d) The h - J_2 phase diagram of the model (4.1) by DMRG, field h is relative to h_{c2} . Symbols mark the FM (black), nematic (red), and AFM (blue) phases. Phase boundaries are inferred from the midpoints between the data. Cyan circle marks a switch to the pair-attraction and green circle to the first-order transition (solid line). Inset: Schematics of the true h - J_2 phase diagram in Fig. 4.1(b). The nematic region and the deviation from the h_{c2} -line are exaggerated.

Cooper problem for superconductivity [219]. Yet, the prior works give a finite J_2 -range for the pairing [202, 203] and provide no insight into the pairs' d -wave symmetry.

The paring of two spin flips can be solved by an exact formalism [200, 212]. It yields the naïve phase diagram of the model (4.1) shown in Fig. 4.1(a), where $h_{c1} = 4J_2 - 2$ is the line of the single spin-flip BEC and the FM-AFM border in the classical limit, which is preempted by the pair-BEC at h_{c2} for *any* J_2 . DMRG energies for 16×8 cylinders with fixed numbers of spin flips yield h_{c1} and h_{c2} values in nearly-perfect agreement (symbols).

The magnon pairing gap Δ , sketched in Fig. 4.2(a), is the difference of these fields, $\Delta \equiv h_{c2} - h_{c1}$, which agrees with the weak-coupling result of the Cooper problem [219]

$$\Delta \approx J_2 e^{-\pi J_2}, \quad (4.2)$$

for $J_2 \gg 1$, but in the d -wave channel. Fig. 4.2(c) explains the predominance of the d -wave. The nodes of the $d_{x^2-y^2}$ harmonic of the attraction potential, $V_{\mathbf{q}}^d \propto (\cos q_x - \cos q_y)$, avoid crossing the magnon band minima at $\mathbf{Q} = (0, \pi)[(\pi, 0)]$, see Fig. 4.2(a), while the nodes of other harmonics do cross them, rendering pairing in these channels unfavorable (see Appendix. C). The spatial extent of the BS in (4.2) can be estimated as $\xi \propto \sqrt{J_2/\Delta} \propto e^{\pi J_2/2}$, relating deviations of the DMRG from exact results in Fig. 4.2(b) at larger J_2 to the finite-size effect ¹.

4.3 Phase diagram

With the pairing problem in the FM state solved exactly, its d -wave symmetry and J_2 -extent elucidated, a nematic phase is expected to exist below the pair-BEC transition h_{c2} down to the single spin-flip BEC h_{c1} , where the single-particle gap closes and the AFM order prevails, see the phase diagram in Fig. 4.1(a). However, as we demonstrate, the many-body effects strongly alter some of these expectations, see Figs. 4.1(b), 4.1(c), and 4.2(d).

Generally, for a BEC condensate to form a superfluid phase its constituents must repel [199, 221]. This is the case for the pair-BEC for large (repulsive) J_2 , implying that the nematic phase *must* occur in *some* region below the h_{c2} -line, which is unaffected by many-body effects.

As the pair binding energy 2Δ increases for smaller J_2 , see Fig. 4.2(b), one also expects a change of the *pair-pair* interaction from repulsive to attractive. With the numerical evidence

¹For example, $\xi \approx 4.8$ for $J_2 = 1.0$ (see Appendix. C)

for that presented below, this change occurs at about $J_2 \approx 0.6$, marked by a cyan circle in the phase diagrams in Figs. 4.1(b) and 4.2(d).

The pair-attraction has two effects. First, the FM-nematic phase boundary in Figs. 4.2(d) and 4.1(b) is pulled above the h_{c2} -line, superseded by a BEC of the multi-pair states ². Second, the nematic region shrinks as the critical pair density for a transition to the dipolar state is reached more readily. Ultimately, at about $J_2 \approx 0.5$ (green circle in Figs. 4.2(d) and 4.1(b)), the nematic phase ceases altogether. In a sense, while the pair-binding gets stronger, the stiffness of the phase vanishes, leading to a first-order collapse of the FM into AFM phase with a finite canting of spins, explaining the zero-field results of Ref. [218] and substantiating the proposal of Ref. [222].

The most striking change concerns the naïve nematic-AFM phase boundary in Fig. 4.1(a). The h_{c1} -line corresponds to a closing of the single-magnon gap for the non-interacting magnons. However, in the presence of the pair-BEC, this gap is strongly reduced due to attraction to the pair condensate (discussed in Sec. 4.5), dramatically extending the AFM phase *above* the h_{c1} -line and leading to about an order-of-magnitude contraction of the naïve nematic phase according to DMRG [223]; see Figs. 4.1 and 4.2(d).

Our Fig. 4.2(d) and Figs. 4.1(b) and 4.1(c) quantify all of the trends described above: the narrow nematic region below the h_{c2} -line, the change to the pair-attractive regime for $J_2 \lesssim 0.6$ leading to multi-pair transitions and further narrowing of the nematic region, and first-order transition for $J_2 \lesssim 0.5$ together with a shift of the FM-to-AFM boundary from the h_{c2} -line to smaller J_2 .

To reveal the resultant phase diagram in Figs. 4.1(b) and 4.1(c), we use iterative zooming because the width of the nematic region and the shift of the transition lines are hard to

²The “true” multi-pair states are likely to occupy only a very narrow region below the $h_{c>2}$ phase boundary, while the nematic phase is also pulled above h_{c2} , in analogy to the AFM state that expands above the h_{c1} -line.

discern on the scale of Fig. 4.1(a). They are derived from Figure 4.2(d), which is based on the DMRG results discussed below, with each symbol corresponding to an individual simulation.

4.4 DMRG results

DMRG calculations are performed on the $L_x \times L_y$ -site square-lattice cylinders with mixed boundary conditions, and width $L_y=8$.³

We use three complementary approaches. The first is long-cylinder “scans,” in which the magnetic field is varied along the length of the 40×8 cylinder, with different phases and their boundaries coexisting in one system. These 1D cuts through the phase diagram are very useful [60, 62, 67–69], allowing one to differentiate first- and second-order transitions by varying the ranges of the scans. Since the parameter gradient can impose unwanted proximity effects, we use such scans judiciously as the first exploratory measure of the nematic phase.

The second approach utilizes 20×8 cylinders, with an aspect ratio that approximates the 2D behavior in the thermodynamic limit [3]. To obtain BEC boundaries in Fig. 4.1, the pairing gap in Fig. 4.2(b), and multi-pair energies, we perform calculations for fixed numbers of spin flips (fixed total S^z) as a function of h and J_2 .

Lastly, the same cylinders are simulated without fixing total S^z to allow for symmetry-broken phases that are induced by weak edge fields. The broken symmetry allows us to measure local order parameters instead of their correlation functions [60, 62, 67–69]. The decay of the induced orders away from the boundary also serves as an excellent indicator of their stability in the 2D bulk.

³Calculations are carried out using the ITensor library [108], typically performing 16 sweeps and reaching a maximum bond dimension of about $m=2000$ to ensure good convergence with a truncation error $<10^{-6}$.

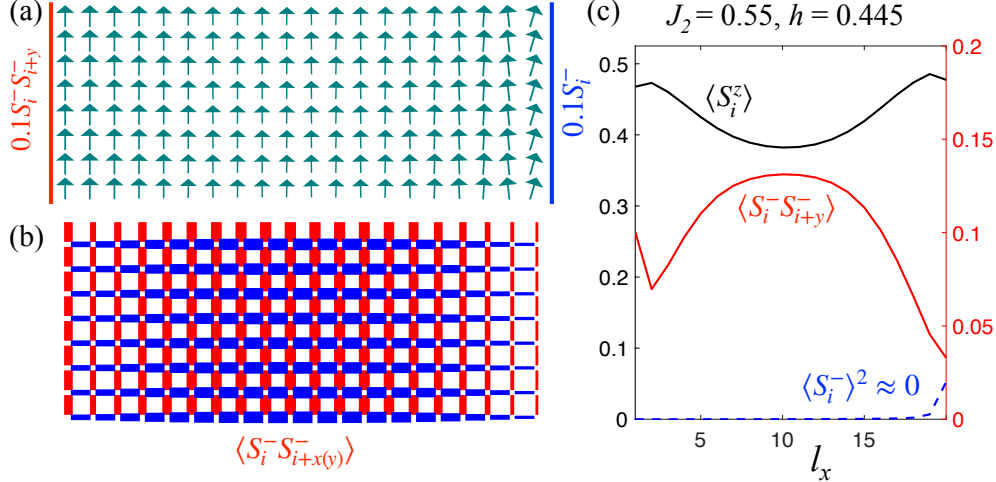


Figure 4.3: DMRG results in the 20×8 cluster for $J_2 = 0.55$ and $h = 0.445$. (a) Ordered moment $\langle S \rangle$ in the xz -plane with pairing field $0.1S_i^- S_{i+y}^-$ (spin-flip field $0.1S_i^-$) at the left (right) edge. (b) Nearest-neighbor component of the pair wave-function; thickness (color) of the bond corresponds to the value (sign) of $\langle S_i^- S_{i+x(y)}^- \rangle$. (c) z -axis magnetization $\langle S_i^z \rangle \approx \langle S \rangle$ (left axis), and nematic $\langle S_i^- S_{i+y}^- \rangle$ and spin-canting $\langle S_i^- \rangle^2$ order parameters (right axis) along the cylinder.

Our Figure 4.3 showcases the described approach and its results for $J_2 = 0.55$ and $h = 0.445$; see the leftmost red circle in Fig. 4.2(d), just above $h_{c2} = 0.441$ for this value of J_2 . Fig. 4.3(a) shows the spin configuration, with arrows' length equal to the local ordered moment $\langle S \rangle$. In Fig. 4.3(b) bonds represent the nearest-neighbor pair wave-function $\langle S_i^- S_{i+x(y)}^- \rangle$, which is directly related to the quadrupole-moment order parameter [210], and Fig. 4.3(c) provides a quantitative measure of them along the length of the cluster. A pairing field $0.1S_i^- S_{i+y}^-$ (spin-flip field $0.1S_i^-$) is applied at the left (right) edge.

In order to avoid the pitfalls of the earlier work [202], an important step in the search for the nematics is to rigorously rule out dipolar orders, since nematic correlations also exist in them as a subsidiary of the multipole expansion. As one can see in Fig. 4.3(a) and 4.3(c), the magnetization is markedly suppressed from full saturation away from the boundary, $\langle S^z \rangle < \frac{1}{2}$, but shows no sign of canting. In the same region, the quadrupolar order parameter is clearly developed, with $\langle S_i^- S_{i+y}^- \rangle \gtrsim 0.1$ and its d -wave character evident from the opposite sign of the horizontal and vertical bonds in Fig. 4.3(b). On the other hand, the induced canting on

To avoid metastable states, we use different initial spin configurations and compare converged energies to ensure the ground state is reached.

the right edge decays away from it with no detectable $\langle S_i^- \rangle$ in the bulk; see Figs. 4.3(a) and 4.3(c), which indicate a gap to one-magnon excitations and the absence of the dipolar order.

Altogether, the analysis presented in Fig. 4.3 leaves no doubt for the presence of the d -wave nematic state for the chosen values of h and J_2 . We point out again that without the pinning field, the nematic state still exists and can be detected through the pair-pair correlations instead of the local order parameter, but they are no more informative and less visual than the results in Fig. 4.3.

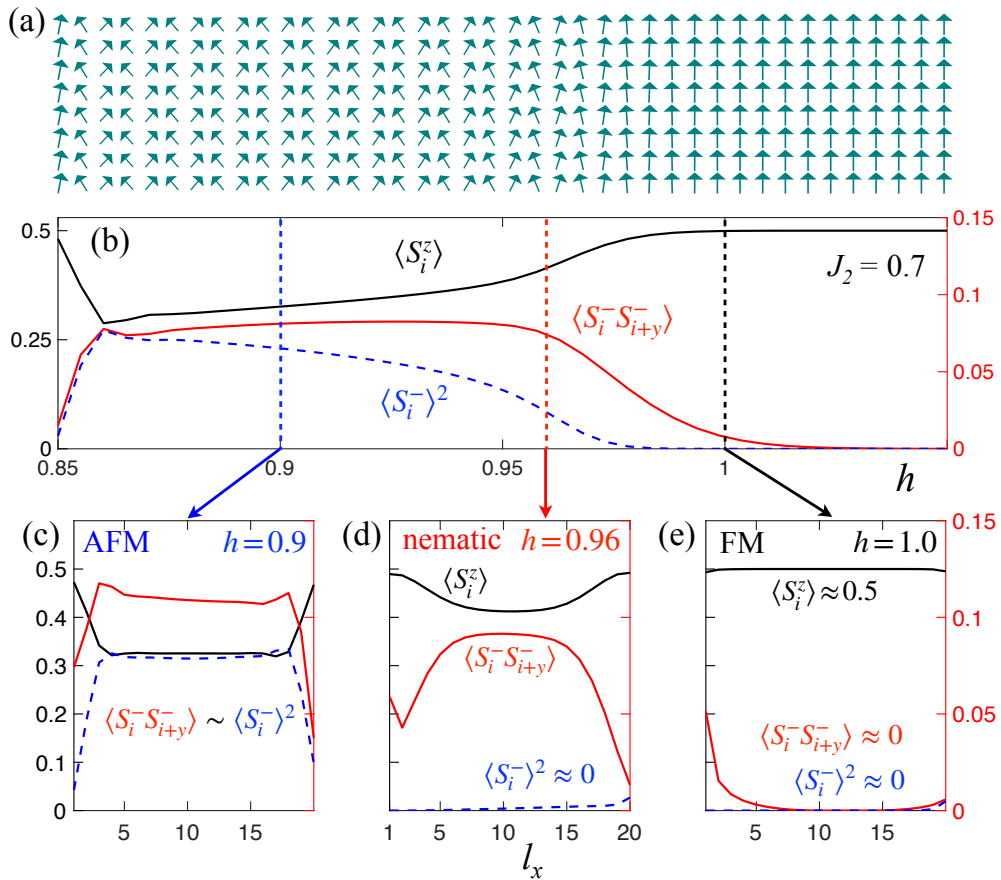


Figure 4.4: Long-cylinder scan in h from 0.85 to 1.05 for $J_2 = 0.7$, with (a) spin pattern of the ordered moments (field $0.1S_i^-$ at the left edge), and (b) magnetization $\langle S_i^z \rangle$ (left axis), and pair $\langle S_i^- S_{i+y}^- \rangle$ and spin-canting $\langle S_i^- \rangle^2$ order parameters (right axis). (c), (d) and (e) Fixed-parameter calculations as in Fig. 4.3(c) for $h = 0.9$, 0.96 , and 1.0 , respectively.

In Figure 4.4, we show a long-cylinder scan for $J_2 = 0.7$ with varied h . From Fig. 4.1(a) one expects to see the nematic phase from the single-magnon-BEC to the pair-BEC fields, from $h_{c1} = 0.792$ to $h_{c2} = 0.966$. Instead, we observe a robust AFM phase with substantial dipolar

order $\langle S_i^- \rangle$ all the way up to a vicinity of h_{c2} ; see Figs. 4.4(a) and 4.4(b). Although $\langle S^z \rangle$ in Fig. 4.4(b) drops precipitously in a narrow field range near h_{c2} , varying the limits of the scan suggests second-order transition(s).

Fig. 4.4(b) shows that near h_{c2} the nematic order parameter dominates the dipolar one, suggesting the presence of the nematic phase. This behavior is markedly different from the case of the quadrupolar order occurring as a byproduct of the dipolar one in the pure AFM mode (see Appendix. C). However, because of the proximity effects of the neighboring phases, it is difficult to make definite conclusions on the extent of the nematic region based solely on the results of Fig. 4.4(b), besides the fact that it is much narrower than suggested naïvely in Fig. 4.1(a).

Thus, we carry out the fixed-parameter, 20×8 cluster calculation as in Fig. 4.3 for several values of h along the path of the scan in Fig. 4.4(b). The results for three such fields, 0.9, 0.96, and 1.0, are shown in Figs. 4.4(c)-(e). Fig. 4.4(d) mirrors Fig. 4.3(c), clearly placing $h = 0.96$ in the nematic region. The finite-size scaling of the nematic order shows little change (see Appendix. C), indicating the near-2D character of our results. The $h = 1.0$ point in Fig. 4.4(e) shows saturated ordered moment and a decay of both pair and spin-canting away from the boundaries, confirming a polarized FM state. The $h = 0.9$ point in Fig. 4.4(c) demonstrates a strong presence of both dipolar and quadrupolar orders—a sign of the AFM phase. For all the (J_2, h) data points contributing to the phase diagram in Fig. 4.2(d), we performed the same type of analysis.

In Figure 4.5, we present the results of the same analysis for $J_2 = 0.45$, with the scan in h from 0.0 to 0.2. Unlike the case of Figure 4.4, where the evolution of magnetization suggests second-order transitions, in Fig. 4.5(a) and 4.5(b) one can notice that the canting of spins changes to a fully polarized state rather drastically. The transition is at about $h \approx 0.14$, which is also noticeably *higher* than the pair-BEC value of $h_{c2} = 0.12$ from Fig. 4.1(a). Another feature is the “scale-invariance” of the scan, demonstrated in Fig. 4.5(c) by zooming on the

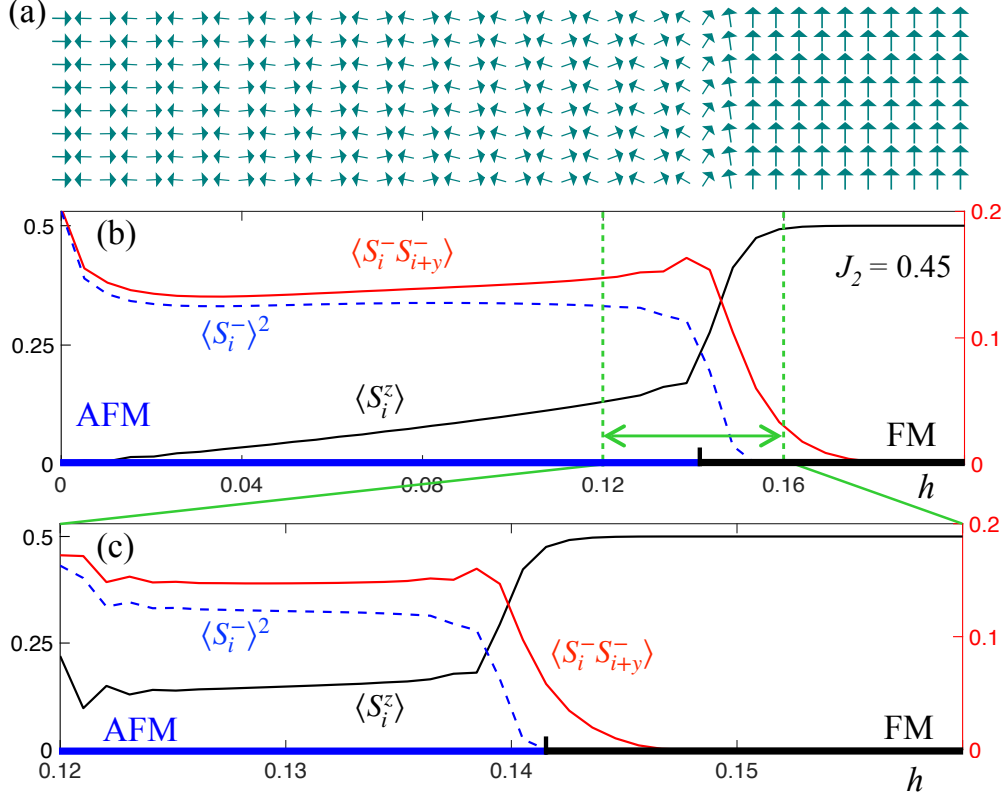


Figure 4.5: (a) and (b) Same as (a) and (b) in Fig. 4.4 for $J_2 = 0.45$ and h from 0.0 to 0.2. (c) Same as (b) for h from 0.12 to 0.16.

narrow field range of 0.12 to 0.16, suggesting the first-order character of the transition. The fixed-parameter calculations described above also find no nematic region between the AFM and FM states, supporting our scenario that pair attraction leads to a first-order collapse of the multi-pair state directly into the dipolar instead of the nematic phase, in a broad agreement with the proposal of Ref. [222].

The AFM-FM transition remains first-order down to zero field with the boundary shifting to $J_2 \approx 0.39$ from the pair-BEC value of $J_2 \approx 0.408$, see Fig. 4.1(b), in agreement with $J_2 = 0.394$ from the earlier study [218].

4.5 Reduction of the single-magnon gap in the presence of pairs

As is discussed above, the actual nematic phase occupies only a fraction of the naïvely anticipated region between h_{c1} and h_{c2} , with the rest of that region taken by the AFM phase. Since h_{c1} corresponds to a closing of the single-magnon gap for the non-interacting magnons, an expansion of the AFM phase above h_{c1} suggests that the single magnon-excitations can reduce their gap due to interaction with the existing pair-condensate. Here, we substantiate this picture by providing quantitative data for the reduction of the single-magnon gap based on the DMRG calculations in the 16×8 cluster with fixed total S^z for the representative value of $J_2 = 0.7$.

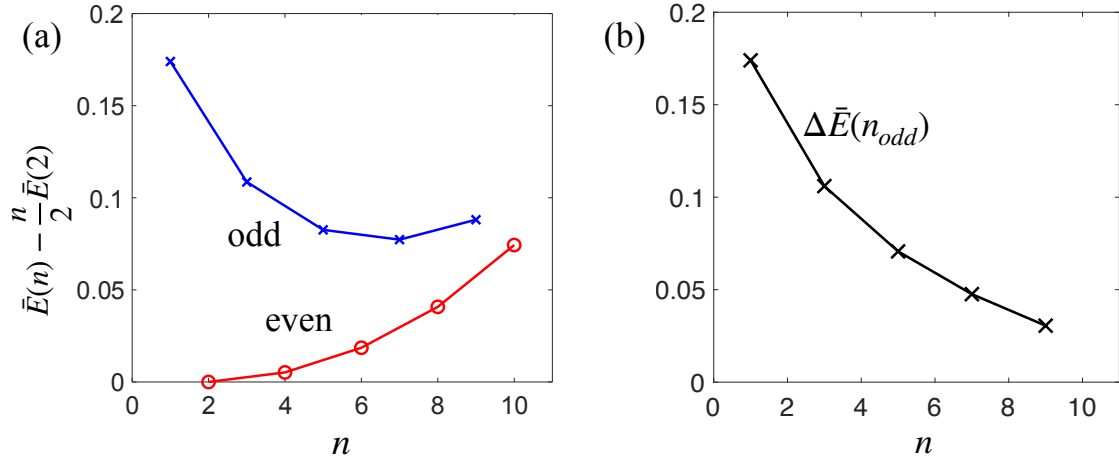


Figure 4.6: (a) The total energy of the system with n magnons relative to the magnon pairing energy in a pair per magnon, $\frac{1}{2}\bar{E}_2$, times n vs n in the 16×8 cluster with fixed total S^z for $J_2 = 0.7$ and n from 1 to 10. Red line is the even- n sector and blue line is the odd- n sector. (b) The single-magnon gap $\Delta\bar{E}(n_{odd})$ vs n .

First, we look at the total energy relative to the magnon pairing energy, as is shown in Fig. 4.6(a). The total energy of the n -magnon state $\bar{E}(n)$ is the energy relative to the energy of the fully polarized state: $\bar{E}(n) = E(n) - E(0)$. Considering it relative to the magnon pairing energy in a single pair per magnon times n , $\frac{n}{2}\bar{E}(2)$, is similar to introducing a chemical potential, so that energies of the states with a different magnon number can be

compared. One can see in Fig. 4.6(a), that for the states with even values of n , in which all magnons form pairs, the relative energy increases with n . This effect is simply due to repulsion between magnon pairs in a finite cluster. However, for the states with the odd n , in which there is one unpaired magnon, their energy decreases with n despite the pair-repulsion, indicating an attraction of the single magnon to the pairs and a reduction of the single-magnon gap.

In Fig. 4.6(b), we plot the single-magnon excitation gap, $\Delta\bar{E}(n)$, defined as $\Delta\bar{E}(n) = (2\bar{E}(n) - \bar{E}(n-1) - \bar{E}(n+1))/2$ for n =odd, which also corresponds to the average vertical distance between a blue cross and two closest red circles in Fig. 4.6(a). Indeed, for $n=1$, the value $\Delta\bar{E}(1)$ is nothing but the magnon pairing gap Δ , see Fig. 2(a) of the main text, which separates the lowest magnon energy from that of the pair. Generalizing it to $n > 1$, corresponds to the energy of an extra magnon with respect to the background energy of magnon pairs. As one can see in Fig. 4.6(b), this single-magnon excitation gap reduces significantly upon increase of n , implying that the magnon is attracted to the magnon pairs already at the level of one magnon–one pair, $n = 3$, and lowers its energy further by interacting with multiple magnon pairs for larger n . The decrease of the single-magnon gap due to interaction with the condensate of magnon pairs results in an expansion of the AFM phase above the non-interacting phase boundary h_{c1} .

4.6 Multi-pair states

For $J_2 \lesssim 0.6$ (left of the cyan circle in Fig. 4.2), spin-flip pairs attract each other and can form multi-pair states. As a result, the actual transition from the FM phase is above h_{c2} and is into the condensates of these multi-pair states. Furthermore, the quadrupolar nematic phase also extends above the h_{c2} line, see Figs. 4.2(d) and 4.1(b), for the same reason the dipolar AFM phase is pulled up above the h_{c1} line.

In this chapter, we provide a comparison of the energies of the states obtained from the DMRG calculations in the 16×8 cluster with fixed total S^z , which gives us the energies of the multi-pair states as a function of J_2 . The energy of the n -magnon state is denoted as $E(n)$ and corresponds to the state with n spin flips from the fully polarized ferromagnet. In the following, we consider only even values of n , because the states with odd values have consistently higher energies than the nearest even ones, indicating that the gap to single-magnon excitations is always present in the considered range of $J_2 > 0.39$ and for the low concentration of spin flips, $n/N_{site} \ll 1$.

In Fig. 4.7(a) and Fig. 4.7(b), we show two schematic plots of the total energy of the system $E(n)$ vs magnon number n for attractive and repulsive magnon pairs, respectively. The $n=0$ state is a fully polarized state and we do not include external field into consideration yet. In either case, the energy is lowered by the increase of the magnon density because the fully polarized state is a highly excited state in the regime where an antiferromagnetic state is a ground state of the system in zero field. If magnon pairs are attractive, the (negative) energy gain by $n+2$ magnons is always greater than the sum of such energy gains by n and 2 magnons separately. Therefore, the $E(n)$ vs n curve should be concave, as is shown in Fig. 4.7(a). In this case, the system can not be stabilized at a low magnon-pair density. Depending on the magnetic field, the ground state is either a saturated FM state or a multi-pair state with a large concentration of magnons, which is beyond the considered low-density regime. On the other hand, if the magnon pairs are repulsive, the energy curve should be convex, as is shown in Fig. 4.7(b), a state with a fixed magnon-pair density can be stabilized by a field, and the magnon pair-density in the ground state will increase continuously upon lowering of the field. In the following consideration, it is convenient to count the energy $E(n)$ from the energy $E(0)$ of the fully polarized state, $\bar{E}(n) \equiv E(n) - E(0)$.

In Fig. 4.7(c) we show the energy of the system with n magnons, $\bar{E}(n)$, relative to the energy of $\frac{n}{2}$ non-interacting pairs, $\frac{n}{2}\bar{E}(2)$, for $J_2 = 0.7$ and $J_2 = 0.5$, obtained from DMRG

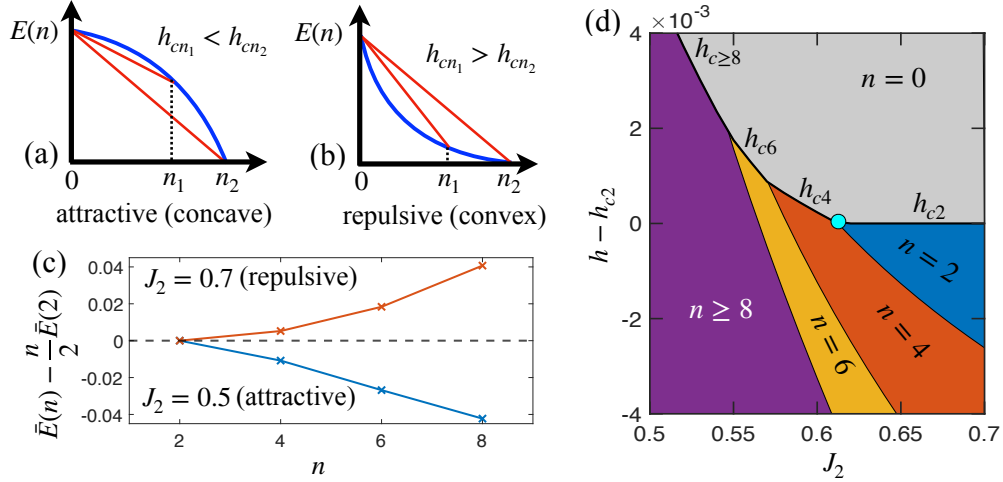


Figure 4.7: (a) and (b) Schematic plots of the total energy $E(n)$ vs magnon number n without the magnetic field. The slope of the line connecting $E(0)$ and $E(n)$ is the multi-pair BEC instability field h_{cn} . The energy vs magnon number curve is concave (convex) for attractive (repulsive) interaction. (c) The total energy of the system with n magnons $\bar{E}(n)$ relative to the energy of $\frac{n}{2}$ non-interacting pairs $\frac{n}{2}\bar{E}(2)$ for $J_2 = 0.7$ and $J_2 = 0.5$ in a 16×8 cylinder. (d) The h - J_2 phase diagram for the states with fixed number of magnons $n = 2, 4, 6, 8$ in a 16×8 cylinder. For $J_2 > 0.61$, magnon pairs are repulsive and the leading instability is the single-pair-BEC ($n = 2$), while for $J_2 < 0.61$ the magnon pairs are attractive, which leads to the multi-pair instabilities with narrowing J_2 steps that resemble a devil's staircase.

calculations in a 16×8 cylinder. For $J_2 = 0.7$, this energy is positive, indicating that adding another pair to the already existing ones cost extra energy due to repulsion between pairs. On the other hand, for $J_2 = 0.5$, this energy is negative due to attraction between pairs.

To identify which multi-pair state has the leading instability with respect to the fully polarized state, we calculate and compare the n -magnon instability field h_{cn} , defined as $h_{cn} = (E(0) - E(n))/n = -\bar{E}(n)/n$, for $n = 2, 4, 6, 8$ in a 16×8 cylinder. In the schematic plots in Figs. 4.7(a) and 4.7(b), the values of h_{cn} corresponds to the discrete versions of the (negative of the) slopes of the lines connecting $E(0)$ and $E(n)$. In the case of attractive magnon pairs, if the multi-pair states are formed that still repel each other, the instability field is achieved at $h_{cn} > h_{c2}$. The biggest achievable h_{cn} corresponds to the leading instability.

In Fig. 4.7(d), we present the h - J_2 phase diagram showing such instability fields for the states with fixed number of magnons in a 16×8 cylinder for J_2 from 0.5 to 0.7. To obtain this phase diagram, we calculated the total energy of the system in magnetic field h as a function of J_2 , $\tilde{E}_n(h, J_2) = E_n(J_2) + nh$, where $E_n(J_2)$ is the total energy of the system with n magnons without magnetic field as above. For each (h, J_2) point in this diagram, the n -magnon state with the lowest $\tilde{E}_n(h, J_2)$ is chosen. The phase boundary between the n -magnon state and the fully polarized state with $n = 0$ corresponds to the $h_{cn}(J_2)$ discussed above.

For $J_2 \gtrsim 0.61$, magnon pairs are repulsive and the leading instability field is h_{c2} . The states with more pairs are stabilized at a lower field. For $J_2 \lesssim 0.61$, the leading instability changes from h_{c2} to h_{c2n} in steps of 2, with h_{c2n} increasing as J_2 is decreased. At the same time, the J_2 -ranges in which each h_{c2n} dominates shrink with the increase of n , resembling a devil's staircase of an infinite sequence of transitions with the ever decreasing width. Although the shift of the leading instability away from the h_{c2} line in favor of the multi-pair h_{c2n} in our analysis is beyond doubt, the finite-size effects prevent a definite confirmation of the devil's staircase scenario.

In the attractive regime there are two scenarios. If multi-pair objects repel, the system will be stabilized at h_{cn} . Near the boundary of the two-magnon stability ($J_2 \lesssim 0.61$), this enables nematic state to survive for a certain field range below h_{cn} before entering the AFM state at a lower field. For a yet smaller J_2 ($J_2 \lesssim 0.5$), and stronger attraction, the multi-pair state cannot be stabilized for any finite n and the system undergoes a first-order transition to a strongly canted AFM state. This transition is discussed in Sec. 4.7 in more detail.

To summarize, in the regime associated with the pair-attraction, we identified condensations from the FM phase into the states with four, six, and eight magnons in a 16×8 cluster. They form a devil's staircase of diminishing ranges of J_2 before reaching the first-order transition point at $J_2 \approx 0.5$, bearing a resemblance to the results of Refs. [210, 211]. However, an

unambiguous confirmation of the higher-multipolar orders associated with the multi-pair BECs is beyond the present study because of the finite-size effects and weak higher-order pairing.

4.7 First order transition from FM to AFM at $J_2 = 0.45$

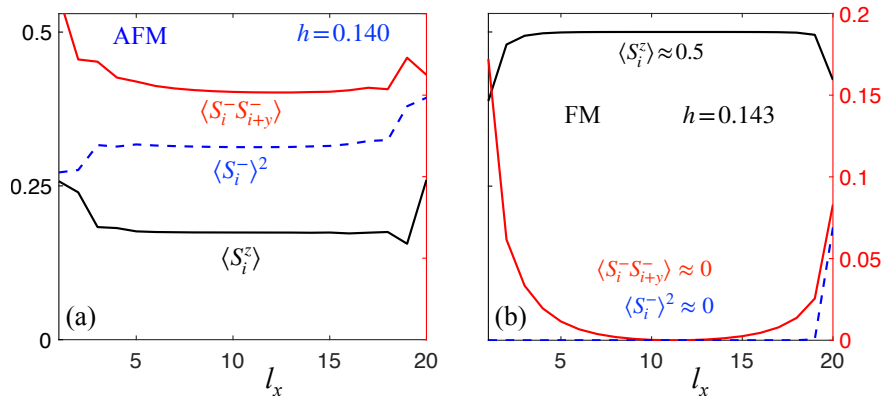


Figure 4.8: DMRG non-scan results for $J_2 = 0.45$, see Fig. 5 in the main text. (a) The ground state at $h = 0.140$ is a strongly canted AFM state as is indicated by the magnetization $\langle S_i^z \rangle$ (left axis), and by the dipolar, $\langle S_i^- \rangle^2$, and quadrupolar, $\langle S_i^- S_{i+y}^- \rangle$, order parameters (right axis). (b) The $h = 0.143$ state is a fully saturated FM state. We apply small pairing and canting fields on the left and right edges, as is described in the main text.

In this section, we provide further evidence supporting the first-order nature of the FM to AFM transition at $J_2=0.45$, based on the calculations in the clusters with fixed parameters (i.e., non-scan calculations). As is shown in Fig. 4.8, for the two very close magnetic fields, $h = 0.140$ and $h = 0.143$, the ground states are very different. For $h = 0.140$, it is a strongly canted AFM state, while for $h = 0.143$ it is a fully saturated FM. This discontinuity in the ground state spin configuration is a clear indication of the first-order transition, consistent with the scan calculations, shown in Fig. 5 of the main text.

Another general feature of the first-order transition is a possibility of the metastable states, in which the two states that are separated by such a transition can appear stable beyond the regions where they constitute global energy minima. We can observe such a metastability

in DMRG calculations. As was mentioned in Sec. 4.6, in the attractive-pair regime, the ground state is either a saturated FM state or a strongly canted AFM state with a large magnon density. An implication of this two drastically different outcomes is that these states remain local minima in terms of magnon density, even if they are not true ground states. For example, in the $h = 0.143$ case (polarized FM ground state), we can initiate DMRG calculation in the collinear Néel state, and the cluster will be stuck in the metastable canted AFM state, showing correlations that are similar to the one in Fig. 4.8(a), but having a higher energy. On the other hand, for the repulsive-pair regime ($J_2 > 0.6$), where all phase transitions are expected to be continuous, we do not detect such a metastability in our DMRG calculations, in agreement with these expectations.

4.8 Summary

We have established the actual extent of the d -wave nematic phase in the phase diagram of the paradigmatic J_1 - J_2 model using analytical and DMRG insights. The nature of the d -wave pairing is explained and the criteria for the existence of the pair-BEC are elucidated. The sequence of the multi-pair BEC transitions is suggested to bridge the d -wave pair-BEC and the first-order FM-AFM transition lines.

The nematic state is not stable at zero field and in the J_2 region close to the FM-AFM border because repulsive pair-pair interactions are generally required to ensure finite stiffness of the pair-BEC state. A suppression of the single-spin-flip gap by an attraction to the pair-condensate is shown to lead to a dramatic order-of-magnitude contraction of the nematic phase compared to the naïve expectations. The hallmark of the remaining nematic region is the significant drop in the magnetization in a very narrow field range near saturation without any dipolar order. Our work provides vital guidance to the ongoing theoretical and experimental searches of the elusive quantum spin-nematics, arming them with realistic

expectations. The proposed scenario and the phase diagram can be expected to be valid for a wide variety of models and materials.

Chapter 5

Quantum Phases in Frustrated Honeycomb Spin Models for Kitaev Material Candidates

5.1 Introduction

Ever since the Anderson's seminal work on the resonating valence-bond state [224], the significant role that can be played by quantum fluctuations in magnets with competing interactions has remained at the forefront of condensed matter physics, inspiring a multitude of quests for exotic states, models that can realize them, and real materials that can host them [18, 195, 225–228]. The elusive spin-liquid states with strongly entangled spins are but one example [18]; others include valence-bond phases with spatial symmetry breaking [58, 199, 229–233], quantum multipolar spin nematics that are quantum analogues of liquid crystals [13, 17, 234, 235], and an especially extensive class of unconventional magnetically *ordered* phases that do not appear in the classical solutions of the underlying spin

models [236–245]. It is the latter group of phenomena that creates a broader context for the present study.

The ordered phases that are not favored classically but are stabilized in the quantum $S = \frac{1}{2}$ limit have attracted significant attention in the search for Kitaev magnets on the honeycomb lattice [246–249]. Recently, this extensive experimental and theoretical effort has expanded to the Co^{2+} materials [9, 250–262]. It appears that the minimal XXZ -anisotropic J_1 – J_3 model with “mixed” ferro-antiferromagnetic (FM-AFM) couplings, given by

$$H = \sum_{n=1,3} \sum_{\langle ij \rangle_n} J_n \left(S_i^x S_j^x + S_i^y S_j^y + \Delta_n S_i^z S_j^z \right), \quad (5.1)$$

provides a tantalizingly close description for many of these compounds [9, 260–265], calling for its unbiased study. Here $\langle ij \rangle_{1(3)}$ stands for the first-(third-)neighbor bonds, $J_1 = -1$ is the energy unit, $J_3 > 0$, and $0 \leq \Delta_n \leq 1$ are the XXZ anisotropies. We note that earlier pre-Kitaev searches for exotic quantum states have focused on a pure AFM J_1 – J_2 – J_3 honeycomb-lattice model [266–277], motivated by the expectation of stronger fluctuations due to the lattice’s low coordination number and by the degeneracies in its classical phase diagram [269].

The model (5.1) was studied in the 1970s [278], yielding the classical phase diagram reproduced in Fig. 5.1(a). These phases are independent of Δ_n because all relevant classical states are coplanar. The ground state is FM for small J_3 , while zigzag (ZZ) order is preferred for large J_3 , and the ferrimagnetic spiral phase (Sp) continuously interpolates between FM and ZZ.

In this chapter, we combine density-matrix renormalization group (DMRG) and minimally-augmented spin-wave theory (MAGSWT) to obtain the groundstate phase diagram of the

quantum $S = \frac{1}{2}$ model (5.1). We focus on the *partial* XXZ version of the model (5.1), with the J_3 -term left in the Heisenberg limit, $\Delta_3 = 1$, referred to as the $J_1^\Delta - J_3$ model. This choice is motivated by real materials, in which further exchanges tend to be more isotropic [249, 279]. The standard version of the model with equal anisotropies, $\Delta_1 = \Delta_3$, referred to as the *full* XXZ or $J_1^\Delta - J_3^\Delta$ model, is considered too.

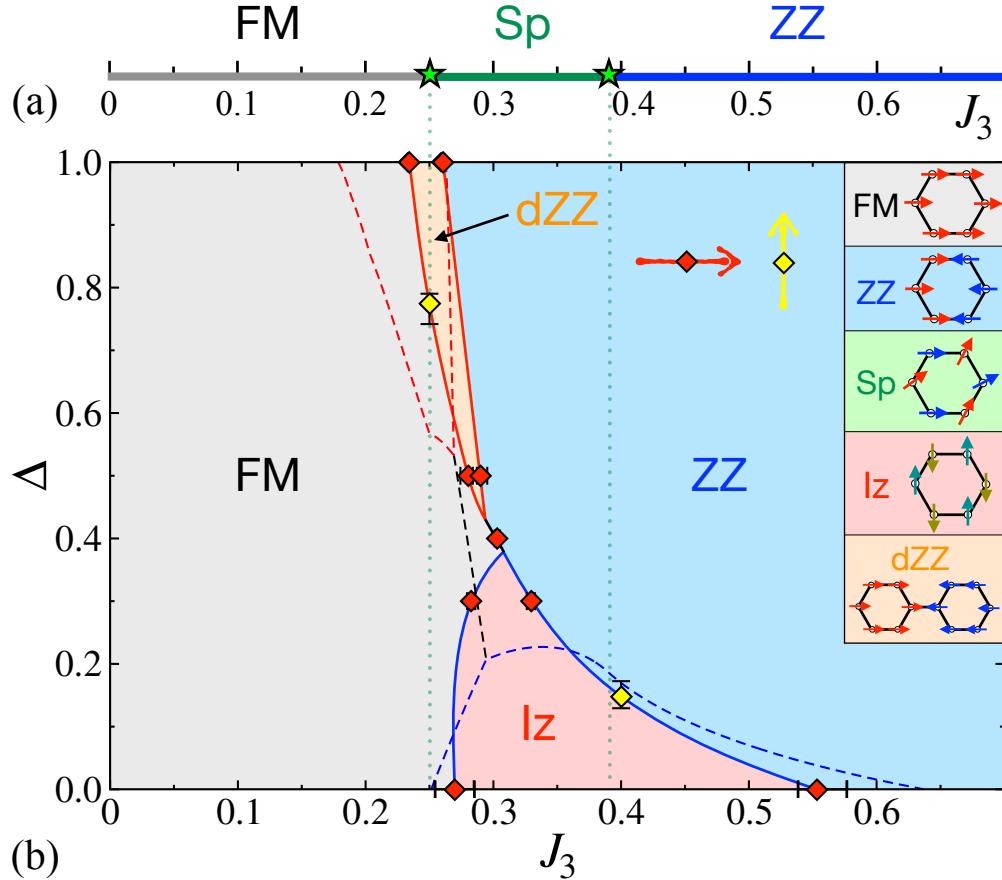


Figure 5.1: The classical (a) and quantum (b) phase diagrams of the XXZ $J_1^\Delta - J_3$ model (5.1) with the ferromagnetic (FM), zigzag (ZZ), spiral (Sp), double-zigzag (dZZ), and Ising- z (Iz) phases. The solid lines are phase boundaries interpolating transition points (diamonds) inferred from the DMRG scans along J_3 (red) and Δ (yellow). The vertical and dashed lines are classical and MAGSWT phase boundaries, respectively. Spins are in-plane for all phases except Iz, see also Fig. 5.2.

5.2 Phase diagram

Our phase diagram for the $S = \frac{1}{2}$ J_1^Δ - J_3 model is given in Fig. 5.1(b). In a dramatic deviation from the classical case, we find two unconventional phases stabilized by quantum fluctuations—the double-zigzag (dZZ) and Ising- z (Iz) phases—as intermediary between the FM and ZZ phases. The FM and ZZ phases also extend well beyond their classical regions to completely supersede the non-collinear classical spiral phase.

The solid lines are phase boundaries interpolating transition points obtained from the DMRG long-cylinder DMRG “scans” by varying J_3 or Δ , as well as from the more precise measurements. The dashed lines are phase boundaries of the same phases obtained by MAGSWT, with both approaches described below.

The qualitative agreement between these approaches is quite remarkable. Both methods produce the classically unstable dZZ and Iz phases, both expand the FM and ZZ phases beyond their classical ranges, and both eliminate the Sp phase. These findings are also in a broad agreement with order-by-disorder arguments [237, 244], which generally favor collinear phases.

We note that recent studies of related models also found the Sp phase to be absent [280, 281]. However, our conclusions on the nature and extent of the quantum phases that replace it differ substantially from theirs. For the details on these differences for the J_1 - J_3 and other models, see discussions below.

The $U(1)$ -preserving Iz phase, with spins ordered Néel-like along the z axis, has been first discovered in the XY J_1 - J_2 AFM-AFM model [276], where Iz order is stabilized solely by quantum effects with no exchange coupling favoring it. In our case, we find the z axis component of the J_3 -exchange in the J_1^Δ - J_3 model crucial for stabilizing the Iz phase in a wide range of parameters, see Fig. 5.1(b). In contrast to Ref. [281], we find only a very

narrow Iz phase in the J_1^Δ - J_3^Δ model. The spin-liquid phases in this model [280, 281] are also not supported (see Sec. 5.7).

The dZZ phase has been recently reported experimentally [260] and found favored by the *bond-dependent* extensions of the XY J_1^Δ - J_3^Δ model [9, 262]. Instead, we find the dZZ phase already in the Heisenberg limit of the principal J_1 - J_3 model (5.1), see Fig. 5.1(b).

5.3 DMRG calculations

DMRG calculations were performed on the $L_x \times L_y$ -site honeycomb-lattice open cylinders of width L_y up to 16 (8 honeycomb cells), using the ITensor library [108]. The majority of the results were obtained on the so-called X-cylinders (XC) [275], in which the first-neighbor bond is horizontal, while both X- and Y-cylinders (YC) were used for more delicate phases ¹. We allow for a spontaneous breaking of the spin $U(1)$ symmetry ², enabling us to measure the local ordered moment $\langle \mathbf{S}_i \rangle$ instead of the correlation function.

Our main exploratory tool is the long-cylinder “scans,” in which one parameter, J_3 or Δ , is varied along the length of the cylinder with L_x up to 40. It provides 1D cuts through the 2D phase diagram [60, 62, 68, 69], see Fig. 5.2, which give approximate phase boundaries. By narrowing parameter ranges of the scans one can determine the boundaries with increased precision, distinguish first- and second-order transitions [13], and uncover hidden phases. In cases when the phase boundary is less obvious, we utilize the fixed parameter (non-scan) calculations on clusters up to 16×16 , with the aspect ratio that closely approximates the 2D thermodynamic limit [3].

¹We typically perform 16 sweeps and reach a maximum bond dimension of $m \sim 3000$ to ensure good convergence with the truncation error of $\mathcal{O}(10^{-5})$.

²Such symmetry breaking in DMRG mimics the 2D system, see Sec. I of the SI in Ref. [10].

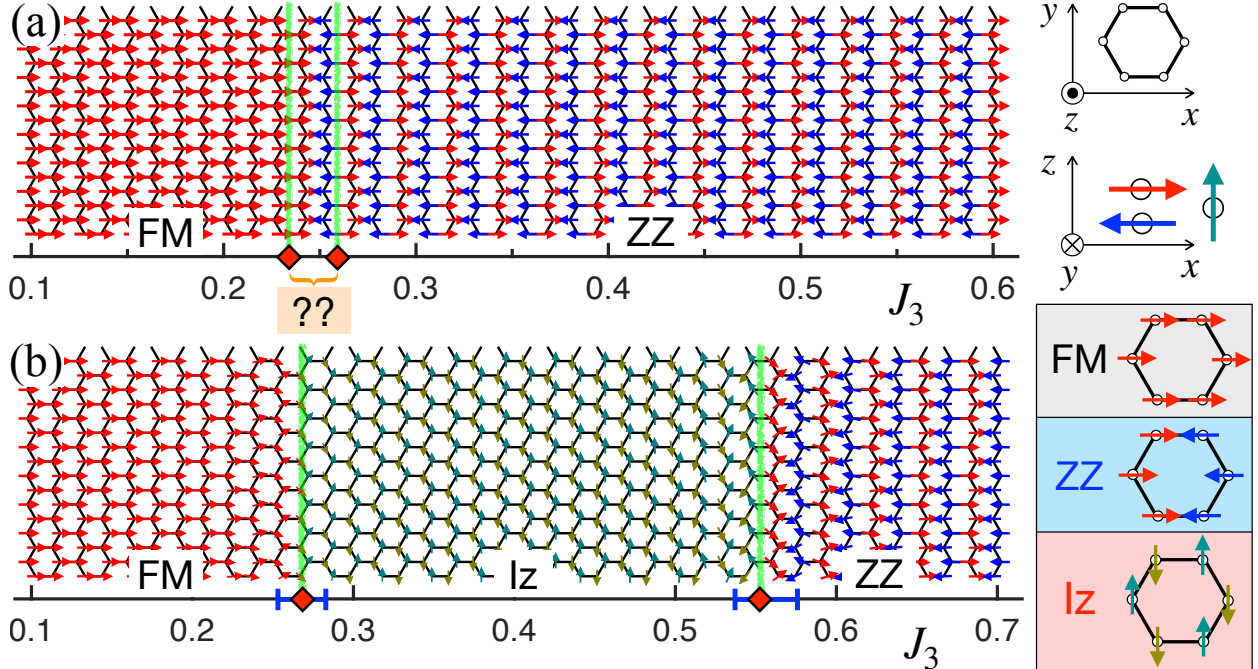


Figure 5.2: Long-cylinder scans of the $J_1^\Delta - J_3$ model (5.1) vs J_3 in the (a) Heisenberg ($\Delta = 1$) and (b) XY ($\Delta = 0$) limit. The arrows show the local ordered moment $\langle \mathbf{S}_i \rangle$. FM, ZZ, and Iz phases are indicated and transitions are determined as described in text. The honeycomb lattice is in the xy plane while spins shown in the figure are in the xz plane.

In Fig. 5.2, we present two long-cylinder scans for the $J_1^\Delta - J_3$ model (5.1), one in the Heisenberg limit, $\Delta = 1$, and the other in the XY limit, $\Delta = 0$, vs J_3 . In the Heisenberg limit, Fig. 5.2(a), the transition from FM to ZZ is very sharp and FM phase seems to terminate right at the classical boundary of this state, $J_3^{cl} = 0.25$. However, one would expect that the FM phase should retreat from this boundary, as the competing ZZ state is fluctuating in the Heisenberg limit, while the FM state is exact. The subsequent analysis reveals a hidden intermediate dZZ state, discussed next. We note that the scan calculation in Fig. 5.2(a) misses it not only due to the narrow region of the dZZ phase, but also because of the high symmetry of the model in the Heisenberg limit, which requires additional effort to avoid metastable states.

Fig. 5.2(b) for the XY limit shows transitions from the FM to Iz and from Iz to ZZ vs J_3 . By using scans in the narrower ranges of J_3 , we verify that the spiral-like spin patterns in the transition regions in Fig. 5.2(b) are proximity effects of the neighboring phases, not

additional phases. The phase boundaries shown in Fig. 5.2(b) and used in the phase diagram in Fig. 5.1(b) are the crossing points of the order parameters vs J_3 (Appendix. D). The error bars are the width of the transition region in the scans, where a discontinuous transition is assigned a width equal to the parameter change over one lattice spacing.

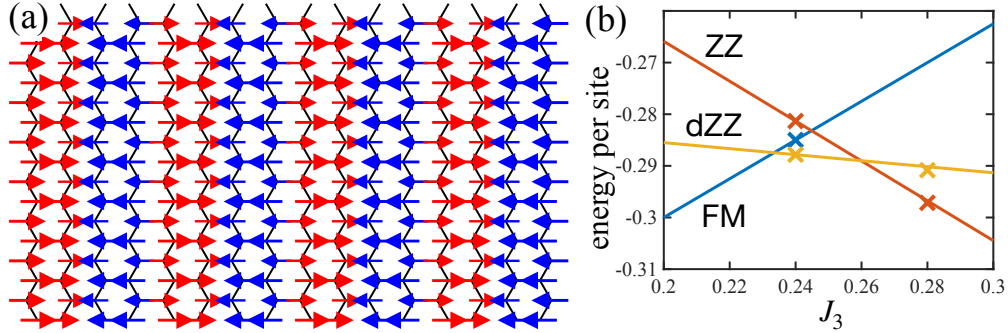


Figure 5.3: (a) Ordered moments in the 16×16 non-scan cluster for $J_3=0.24$, showing dZZ pattern. (b) Energies of the three competing phases vs J_3 , crosses are DMRG results and higher-energy states are metastable. Lines are extrapolated energies, $\langle \psi_i | H(J_3) | \psi_i \rangle$, where ψ_i are the three states at $J_3=0.24$.

In the Heisenberg limit, the three states, FM, dZZ, and ZZ, compete in the proximity of the classical FM boundary $J_3=0.25$. Because of the high spin-symmetry of the model, and depending on the initial state, all three can be stabilized in the non-scan DMRG simulations, such as the one shown in Fig. 5.3(a) for $J_3 = 0.24$ in the 16×16 cluster. As is shown in Fig. 5.3(b), the energy of the dZZ is the lowest, with the FM and ZZ being metastable, suggesting that the transitions between the corresponding phases are first order. To identify their phase boundaries, we compare the energies of these three states as a function of J_3 using extrapolations based on the spin-spin correlations extracted at $J_3=0.24$ from the center of the cluster for each of the states. While the FM line is exact in this limit, the extrapolated energies for ZZ and dZZ are also very close to the ones given by a direct DMRG calculation at a different value of J_3 , justifying the analysis, see Fig. 5.3(b). The dZZ phase is found to be confined between $J_3=0.2333$ and 0.2596 .

The lower spin-symmetry away from the Heisenberg limit helps to reveal the dZZ phase more readily, see Fig. 5.4(a) for a long-cylinder scan along the Δ axis and fixed $J_3=0.25$, confirming

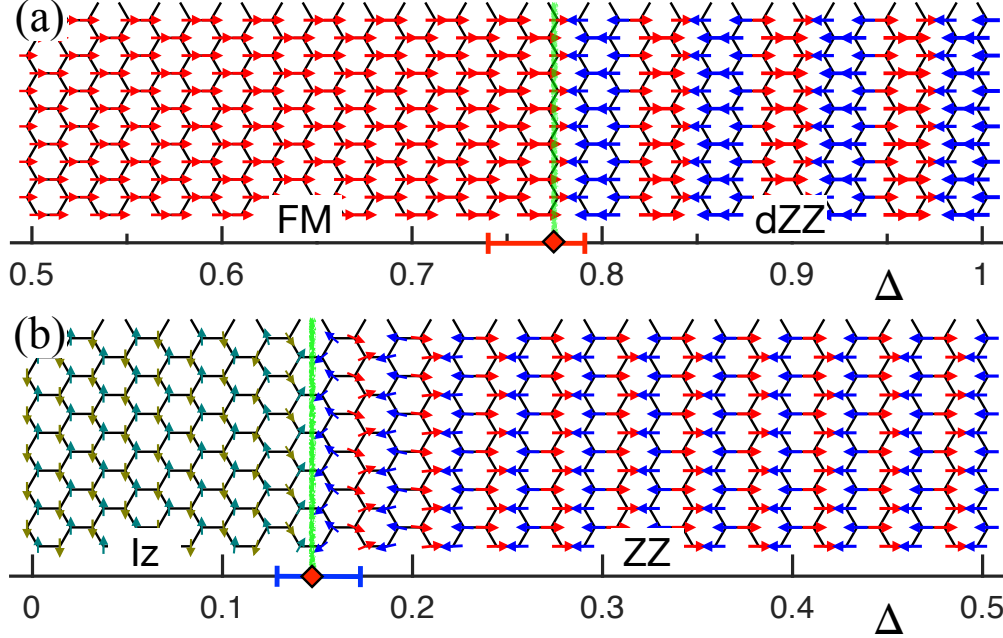


Figure 5.4: Long-cylinder Δ -scans of the J_1^Δ - J_3 model (5.1) for (a) $J_3=0.25$ and (b) $J_3=0.4$. Notations are as in Fig. 5.2.

the presence of this phase in an extended region of the phase diagram in Fig. 5.1. A similar Δ -scan for $J_3=0.4$ in Fig. 5.4(b) compliments the J_3 -scans in establishing boundaries of the Iz phase.

In Fig. 5.5, we show additional J_3 -scans that are used to construct the phase diagram of the J_1^Δ - J_3 model in Fig. 1(b) of the main text. In each scan, approximate transition boundaries with error bars are indicated. In the $\Delta=0.5$ scan, we observe a narrow phase intervening between FM and ZZ, which is identified as the dZZ phase using non-scan calculations in the region of J_3 from 0.28 to 0.29 (not shown). The $\Delta=0.4$ scan in Fig. 5.5 shows a direct transition from FM to ZZ. The non-scans using smaller clusters in the vicinity of $J_3=0.3$ have initially suggested a spin-liquid (SL) state discussed below, which turns into ZZ order in the larger non-scan clusters. Although we cannot completely rule out the Iz state for $\Delta=0.4$, it must be extremely narrow if it exists. The $\Delta=0.3$ scan is similar to Fig. 2(b) of the main text with an extended region of the Iz phase intervening between FM and ZZ.

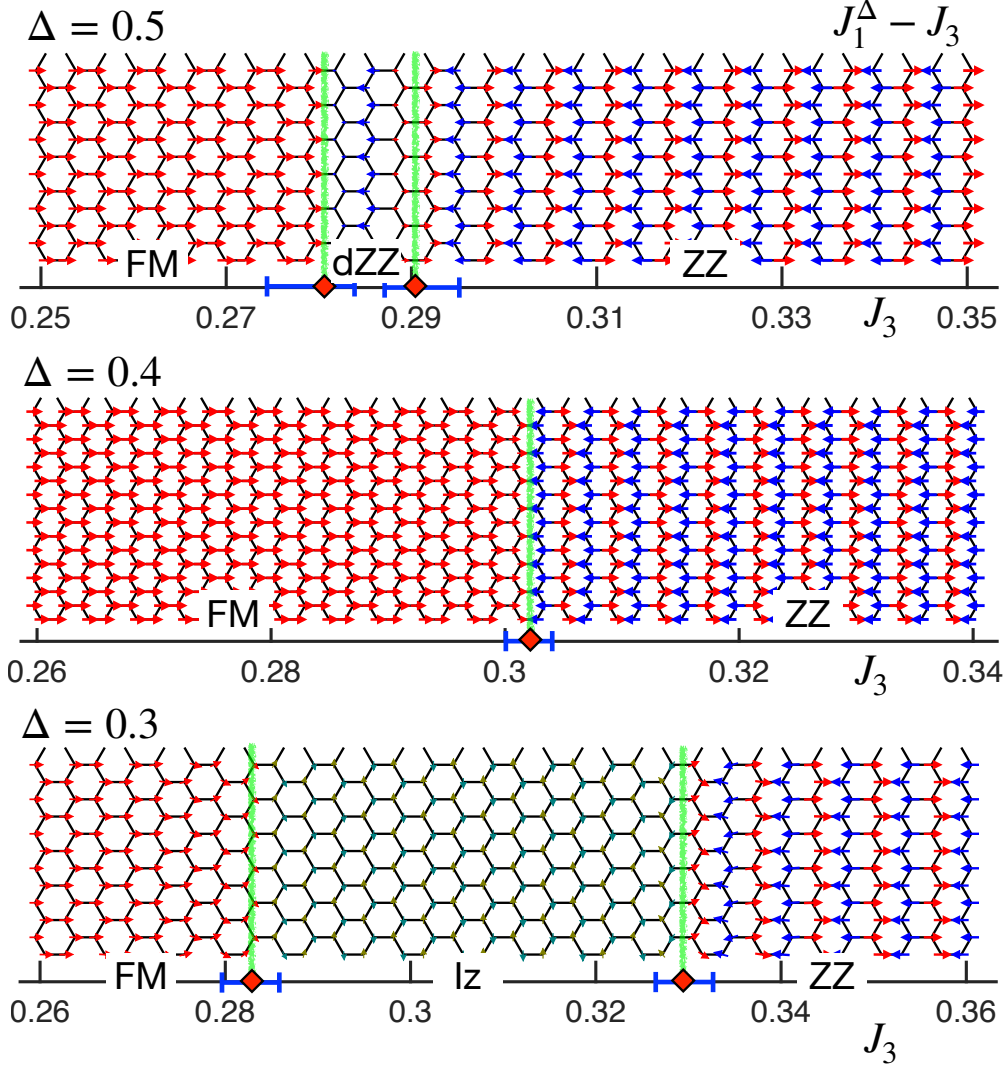


Figure 5.5: DMRG J_3 -scans for $\Delta=0.5$, 0.4, and 0.3 in the J_1^Δ - J_3 model. The scans for $\Delta=0.5$ and 0.3 are on the 12×32 cylinders while the $\Delta=0.4$ scan is on the 16×40 cylinder.

5.4 Minimally-augmented spin-wave theory

The standard SWT is successful at accounting for quantum effects in the ordered states [282], but cannot describe either the ordered phases that are not classically stable, or the shifts of the phase boundaries by quantum fluctuations. An analytical approach to address this problem, originally proposed for the classically unstable field-induced states in the transverse-field Ising and frustrated Heisenberg models [283–285], can be successfully applied here.

The method consists of introducing a local field in the direction of the ordered moment \mathbf{n}_i for the proposed (unstable) classical spin configurations, leading to a shift of the chemical potential in the bosonic SWT language

$$\delta\mathcal{H} = \mu \sum_i (S - \mathbf{S}_i \cdot \mathbf{n}_i) = \mu \sum_i a_i^\dagger a_i, \quad (5.2)$$

while leaving the classical energy of the state unchanged. The *minimal* value of μ is chosen to ensure stability of the spectrum, i.e., that the squares of all eigenvalues of the SWT matrix are positive definite. Then, the energy of the proposed spin state, $\mathcal{E} = E_{cl} + \delta E$, with the $1/S$ -correction to the groundstate energy δE , is well-defined and can be compared with the energies of the competing states calculated to the same $O(S)$ order.

The power of the method, coined as the *minimally augmented SWT* (MAGSWT), is not only in its simplicity, but in the form of Eq. (5.2), which guarantees that its contribution to the Hamiltonian is positive for $\mu > 0$. In turn, this implies that the so-obtained groundstate energy \mathcal{E} is an *upper bound* for the energy of the suggested spin state to the order $O(S)$. This method allows one to consider the phase beyond its classical range of stability and inspect states that are classically not competitive, but can lower their energy due to quantum fluctuations. The new phase boundaries are determined from the crossings of the energies \mathcal{E} for the competing phases as a function of the varied parameter(s).

We note that MAGSWT may not be applied to an arbitrary classically-unstable state [285], with the absence of the linear-bosonic terms in the $1/S$ -expansion for a given state being a sufficient criterion of its applicability.

5.5 MAGSWT results

In case of the $XXZ J_1^\Delta - J_3$ model (5.1), all four competing phases of interest are collinear, which guarantees the absence of the linear-bosonic terms, while the non-collinear Sp state is not the subject of MAGSWT, as it corresponds to a minimum of the classical energy in its entire possible range of existence.

The technical procedure of extracting minimal μ vs J_3 and Δ for each phase is discussed in Appendix. D. We note that the limiting XY and Heisenberg cases and select momenta are useful for obtaining analytical expressions for $\mu(J_3, \Delta)$, eliminating the need of a numerical scan of the momentum space for spectrum instabilities. With that, the energy surfaces $\mathcal{E}(J_3, \Delta)$ are readily obtained for each phase and the MAGSWT phase boundaries are drawn from the intersections of such surfaces.

The resulting phase boundaries are shown in Fig. 5.1(b) by the dashed lines. Most, if not all, of the features already discussed above are present. The noncollinear Sp phase is not effective at benefiting from quantum fluctuations, in agreement with the order-by-disorder arguments [237], and is wiped out. The classically-unstable dZZ and Iz phases are extensive and both FM and ZZ expand beyond their classical borders. A close quantitative agreement with the DMRG phase boundaries can also be observed, with most discrepancies concerning the borders of the less-fluctuating FM phase (see Appendix. D). Otherwise, the entire picture for the $J_1^\Delta - J_3$ model in Fig. 5.1(b) is in rather astonishing agreement with the numerical data.

5.6 The $J_1^\Delta - J_3^\Delta$ model

The phase diagram of the full XXZ model (5.1) with equal anisotropies in both terms, obtained using the same methods as described above, is presented in Fig. 5.6. It repeats most of the trends of the partial XXZ model in Fig. 5.1(b), such as the absence of the Sp phase, expansion of the FM and ZZ, and the presence of the two unconventional phases, Iz and dZZ.

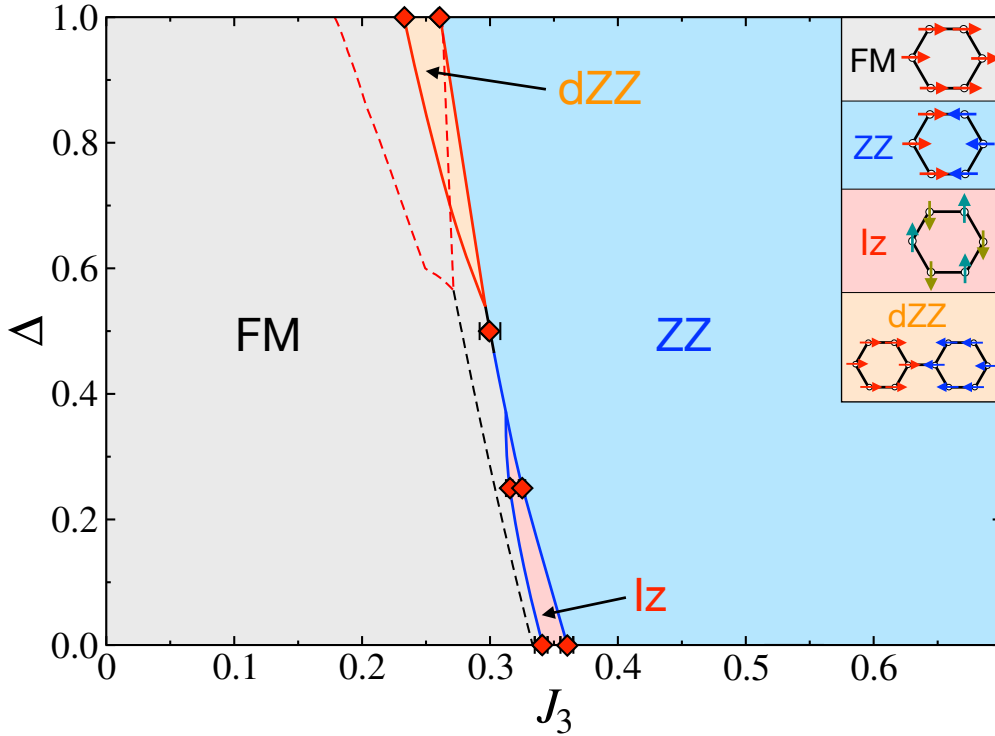


Figure 5.6: The quantum $S = \frac{1}{2}$ phase diagrams of the full XXZ $J_1^\Delta - J_3^\Delta$ model (5.1), c.f. Fig. 5.1(b). See text.

In Fig. 5.7, we show DMRG J_3 -scans that are used to construct the phase diagram of the $J_1^\Delta - J_3^\Delta$ model in Fig. 5 of the main text. While the $\Delta = 0.5$ scan looks somewhat similar to the scan for the same Δ in Fig. 5.5, it has a direct FM-ZZ transition at $J_3 = 0.30$, with the separate non-scan calculations showing no sign of the intermediate phase.

In the $\Delta = 0.25$ and $\Delta = 0$ scans, an intermediate region is suggested with the suppressed ordered moments. As we discuss next, initial non-scans in these regions have shown strongly

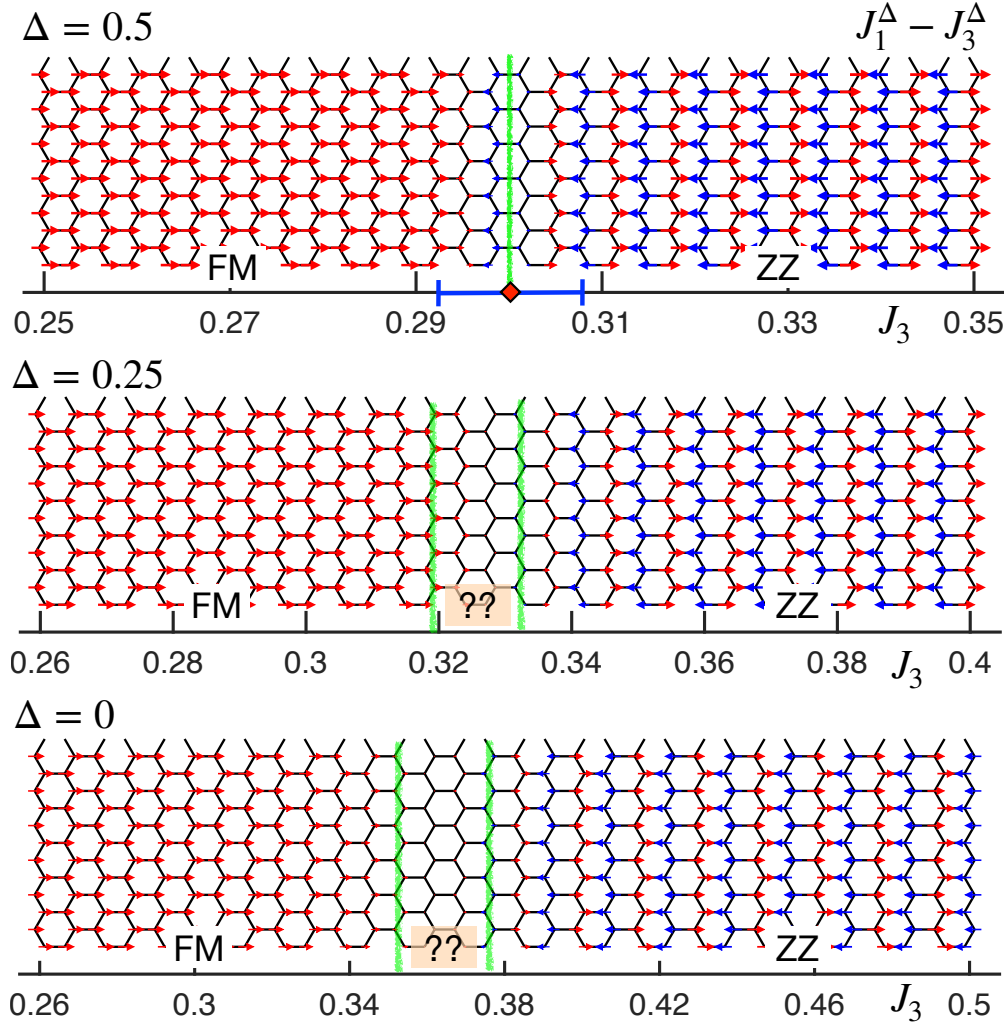


Figure 5.7: DMRG J_3 -scans in the $J_1^\Delta - J_3^\Delta$ model for $\Delta=0.5$, 0.25 , and 0 on the 12×32 cylinders.

anisotropic correlations, with short correlations in one direction and FM-like in the other, resembling the state that has been hypothesized as a spin liquid in Ref. [280]. Upon closer inspection and finite-size scaling, they reveal a narrow region of the Iz phase. For $\Delta = 0$, $J_3 = 0.33$ is in the FM phase, $J_3 = 0.37$ is in the ZZ phase, and $J_3 = 0.35$ is in the Iz phase by that analysis, confining the Iz phase between $J_3 = 0.34$ and 0.36 . For $\Delta = 0.25$, the Iz phase is even narrower, between $J_3 = 0.315$ and 0.325 .

In contrast to the recent studies [280, 281], our results do not support the proposed spin-liquid states in the Heisenberg [281], or strongly-anisotropic ($\Delta = 0.25$) nearly XY [280]

limits. The J_3 -width of the quantum Iz phase in the same XY limit ($\Delta=0$) is also an order of magnitude narrower in our case than the one suggested in [281].

While the first of the quantum phases, dZZ, missed by the previous works due to small cluster sizes or an approximate nature of their approaches [281], is nearly the same in the partial and full XXZ models in Fig. 5.1(b) and Fig. 5.6, respectively, the Iz phase is substantially more tenuous. In fact, the initial DMRG scans have shown a direct FM-ZZ transition, with some possible narrow intermediate state. Dedicated non-scans in that region did uncover short-range correlations in both XC and YC clusters (sec. 5.7), not unlike the ones reported in Ref. [280]. However, these spin-liquid-suspects either order on the cylinder width increase (XC), or indicate a sufficiently robust Iz order in the range of $J_3=0.315-0.325$ for $\Delta=0.25$ and $J_3=0.34-0.36$ for $\Delta=0$, which we will discuss in details in the next session.

It is worth noting that MAGSWT in the XY limit of the full XXZ model shows a close, but insufficient, competition of the strongly fluctuating Iz phase, rendering it absent from its version of the phase diagram in Fig. 5.6.

5.7 Pseudo-spin-liquid state

In some of the transition regions discussed above for both versions of the XXZ J_1 - J_3 model, we have found regimes that can be taken as evidence for a spin-liquid state, similar to the ones reported in Ref. [280]. These include nearly zero ordered moment at intermediate bond dimension in DMRG calculations, for which the system is expected to spontaneously break symmetry if it has an order, and the short-range spin-spin correlation in one direction, as shown in Figs. 5.8(a) and 5.8(b). This anisotropy in correlations is suspicious, however, as one would expect a “lock in” of such 1D-like correlations into some order in a larger system.

Indeed, with the increase of the system's width, one of the spin-liquid possibilities in the $J_1^\Delta - J_3$ model ($\Delta = 0.4$), develops a ZZ order, see Fig. 5.8(c).

Another such suspect region is in the $J_1^\Delta - J_3^\Delta$ model, $\Delta = 0.25$, near $J_3 = 0.32$, similar to the one reported in Ref. [280], but it does not follow that trend. In fact, as is shown in Fig. 5.8(d), the spin-liquid candidate looks even more realistic (less anisotropic) in the YC lattice. However, the system was tested with various boundary conditions and responded strongly to the staggered pinning field $(-1)^i h S_i^z$, developing a substantial Iz order, see Fig. 5.8(e), with the ordered moment nearly constant $\langle S \rangle \approx 0.1$ in the bulk. Following Ref. [3], we carry out an $1/L_y$ -scaling of the ordered moment, which gives a strong indication of the Iz order in the thermodynamic limit, see Fig. 5.8(f).

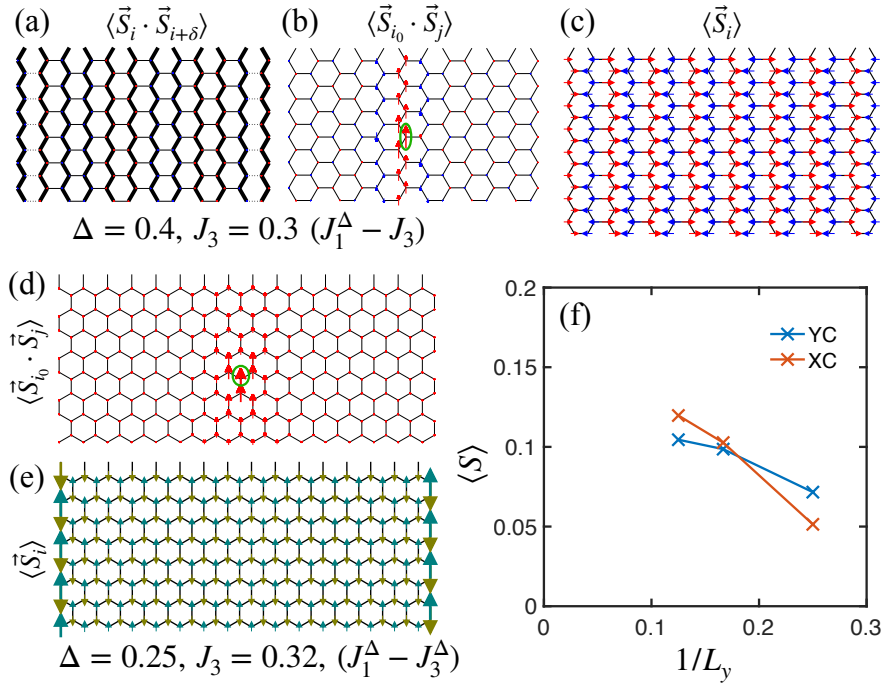


Figure 5.8: (a) and (b) 12×12 XC cylinder non-scans for $\Delta = 0.4$ and $J_3 = 0.3$ in the $J_1^\Delta - J_3$ model showing: (a) nearly-zero ordered moment and nearest-neighbor $\langle \vec{S}_i \cdot \vec{S}_{i+\delta} \rangle$ (thickness of the bond), and (b) spin-spin correlation $\langle \vec{S}_{i_0} \cdot \vec{S}_j \rangle$, denoted by the length and direction of the arrow, with i_0 site shown by the green oval. The arrow on i_0 is of length 0.25. (c) Same as (a) on the 16×16 cylinder. (d) Same as (b) on the 8×32 YC cylinder for $\Delta = 0.25$ and $J_3 = 0.32$ in the $J_1^\Delta - J_3^\Delta$ model. (e) Ordered moment in (d) under the Iz pinning field of 0.5 on both edges. (f) The $1/L_y$ -scaling of the Iz ordered moment in the center of the cylinder with the edge pinning fields from (e) and the XC and YC cylinders having the aspect ratio 2, which mimics the 2D limit closely—see Ref. [3].

5.8 Generalized $J_1^{\Delta_1}-J_3^{\Delta_3}$ model for $\text{BaCo}_2(\text{AsO}_4)_2$

Extensive experimental and theoretical searches for the Kitaev magnets on the honeycomb lattice have recently expanded to the Co^{2+} , $S_{eff} = 1/2$ materials. Among this family, $\text{BaCo}_2(\text{AsO}_4)_2$ has received significant attention [9, 253, 260–262]. Its minimal model description has currently coalesced to a generalized XXZ FM-AFM $J_1^{\Delta_1}-J_3^{\Delta_3}$ model [9, 261, 262, 280] with additional Kitaev-like bond-dependent terms.

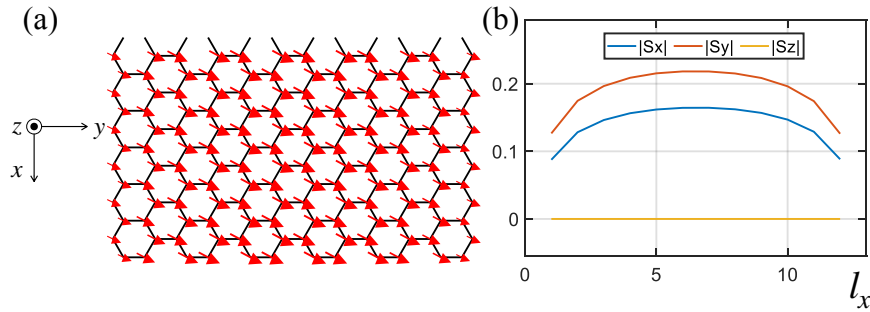


Figure 5.9: (a) Spin pattern in the 12×12 DMRG cylinder and (b) spin components in the ground state of the generalized XXZ $J_1^{\Delta_1}-J_3^{\Delta_3}$ model from Ref. [9].

One such model parametrization was advocated in Ref. [9], based on fitting experimental excitation spectrum in high fields and assuming the spin-spiral ground state with a nearly commensurate ordering \mathbf{Q} -vector in zero field. Leaving the correctness of the latter assumption aside [260], the model parameters in Ref. [9] were constrained to match the ordering \mathbf{Q} -vector of the planar spin spiral from the *classical* solution of the generalized XXZ $J_1^{\Delta_1}-J_3^{\Delta_3}$ model.

Since we find that such a spiral state does not survive at all in the *quantum* $S = 1/2$ version of the XXZ J_1-J_3 model, as it is overtaken by the collinear phases due to quantum fluctuations, we have checked the validity of the key assumption made in Ref. [9] regarding the structure of the ground state for their proposed set of parameters. The model used in Ref. [9] has strong XXZ anisotropies for the J_1 and J_3 terms, but of different sign, $\Delta_1 \approx 0.16$ and $\Delta_3 = -0.34$,

and the ratio $J_3/J_1 \approx -0.33$ (see Eq. [13] of Ref. [9]). The model also contains two minimal bond-dependent corrections in the J_1 exchange matrix.

We have performed DMRG calculations for these parameters, including the bond-dependent terms, on a 12×12 cylinder in order to see whether the opposite sign of Δ_1 and Δ_3 , or the bond-dependent terms, are able to stabilize the spiral state to avoid the fate we find for it in the other models. As is shown in Fig 5.9, we find an FM ground state instead of the spiral state, suggesting that the model parameters for $\text{BaCo}_2(\text{AsO}_4)_2$ proposed in Ref. [9] are not adequate to describe its ground-state spin configuration and require a reconsideration.

5.9 The generalized Kitaev- J_3 model for $\alpha\text{-RuCl}_3$

$\alpha\text{-RuCl}_3$ has been one of the most promising candidate in the search for Kitaev spin liquids [286]. The material features a honeycomb lattice emerging from a nearly perfect edge-sharing RuCl_6 octahedra, an ideal match for the realization of the exotic Kitaev Hamiltonian [287]. While experimental observations of phenomena such as the anomalous thermal Hall effect [288, 289] and continuum in the excitation spectrum [290] provide encouraging evidence supporting the Kitaev spin liquid, it has been argued that the presence of other types of spin exchanges can substantially deviates the model away from the pure-Kitaev limit while retaining consistencies with experiments [249, 263, 291, 292].

Despite of an enormous amount of theoretical researches, the effective spin model for $\alpha\text{-RuCl}_3$ has yet to be settled. Under the commonly used cubic reference frame, the symmetry-allowed terms are the Kitaev K , the Heisenberg J , and the off-diagonal Γ and Γ' exchanges. The important role of the third-neighbor isotropic exchange J_3 has also been pointed out [249]. Consensus has been reached regarding the minimal model of $\alpha\text{-RuCl}_3$ taking the form of the

K - J - Γ - Γ' - J_3 model, with its Hamiltonian written as:

$$H = \sum_{\langle ij \rangle \gamma} [J \mathbf{S}_i \cdot \mathbf{S}_j + K S_i^\gamma S_j^\gamma + \Gamma (S_i^\alpha S_j^\beta + S_i^\beta S_j^\alpha) + \Gamma' (S_i^\gamma S_j^\alpha + S_i^\alpha S_j^\gamma + S_i^\beta S_j^\gamma + S_i^\gamma S_j^\beta)], \quad (5.3)$$

However, the parameters of the model are still largely under debate [263].

In a forthcoming paper [293], we argue that the existing key phenomenological observations impose strong natural constraints on the parameterization of the model for α -RuCl₃. We study the ground state phase diagram of the K - J - Γ - Γ' - J_3 model focusing on the relevant parameter region under such constraints. Employing a combination of exact-diagonalization, semi-classics and DMRG, we obtain an extended phase diagram as shown below in Fig. 5.10.

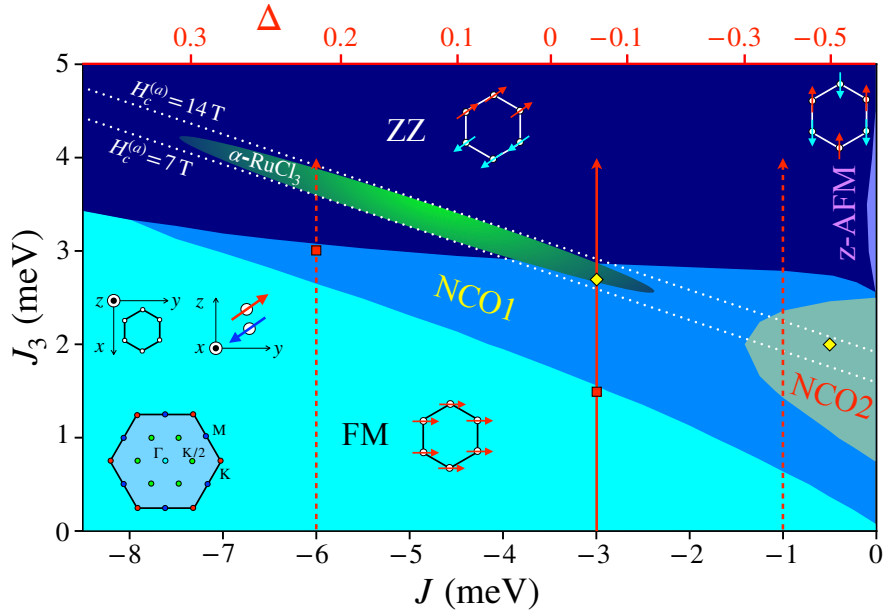


Figure 5.10: The quantum $S = \frac{1}{2}$ phase diagram of the K - J - Γ - Γ' - J_3 model in the J - J_3 plane with fixed $K = -7.567$, $\Gamma = 4.276$, $\Gamma' = 2.362$ (in unit of meV). Phases include ferromagnetism (FM), zigzag (ZZ), out-of-plane antiferromagnetism (z -AFM) and two non-collinear (NCO) out-of-plane counter-rotating spirals with different ordering vectors. The green region is the possible parameter region for α -RuCl₃ constrained by experimental observations including critical in-plane fields denoted by the dotted lines.

One of the highlights of this work is the detailed agreement between different methods on the nature of the incommensurate phases that realize two distinct counter-rotating helical states (denoted as NCO in fig: 5.10). In Fig. 5.11 we present the details of a DMRG simulation showing a counter-rotating spiral with its ordering vector \vec{Q} along the Γ -M direction, denoted as the NCO1 phase in Fig. 5.10 (\vec{Q} of the NCO2 phase is along the Γ -K direction). The spins are in the yz plane which is perpendicular to the ordering vector \vec{Q} . Spins in different sublattices rotates in opposite direction along \vec{Q} .

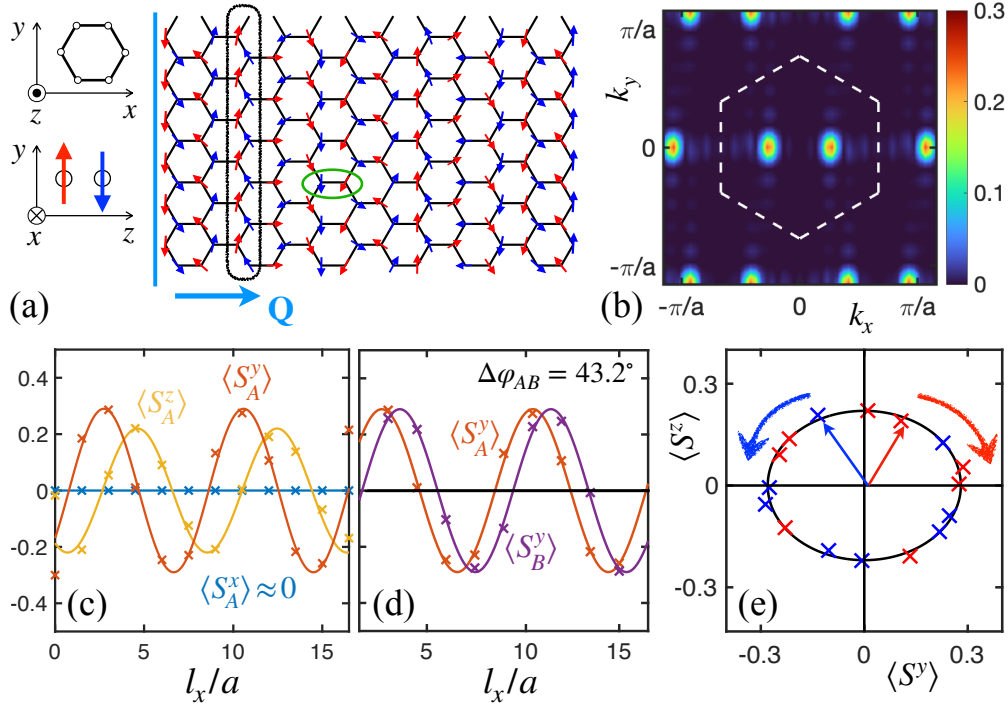


Figure 5.11: In a 12×12 XC cylinder with K, Γ, Γ' fixed as in Fig. 5.10 and $J = -3.0$ meV, $J_3 = 2.7$ meV, (a) the local ordered moments $\langle \mathbf{S}_i \rangle$ represented by the arrows. Spins in sublattice A and B are in red and blue, respectively. The honeycomb lattice is in the xy plane, and spins are in the yz plane that form an out-of-plane counter-rotating spiral with its \vec{Q} along the x direction. (b) Squared norm of the Fourier transform of S^y for spins in sublattice B, which has a maximum at \vec{Q} that is along the Γ -M direction. (c) Three components of the ordered moments for the spins in sublattice A, averaged over the y direction and plotted along the x direction. (d) S^y of spins in different sublattices averaged over the y direction and plotted along the x direction. Spins in two sublattices that have the same l_x are denoted by green ellipse in (a). For (c) and (d), the cross markers are the data points and lines are fitted sine functions. (e) The ordered moments of spins in the S^y - S^z plane (spins on edges are excluded). The straight arrows from the center point to the ordered moments of the spins in the rounded black rectangle in (a). The curved arrows indicate the rotating orientation of the spins along the propagation direction of the spiral \vec{Q} .

5.10 Summary

In this chapter, we have studied the emergence of the quantum phases that are not stable classically within a simple model of great current interest. We have combined state-of-the-art DMRG and analytical approaches to obtain conclusive phase diagrams of this model. It is established beyond any reasonable doubt that the two unconventional quantum phases occupy a significant portion of this diagram, with the known phases also extending well beyond their classical regions and completely replacing the less-fluctuating non-collinear phase. The results of the analytical MAGSWT approach are shown to be in a close accord with the numerical DMRG data, providing additional insights into the energetics of the quantum stabilization of the non-classical phases and offering a systematic path for the explorations of similar models.

The proposed phase diagrams have direct relevance to a group of novel materials and provide important guidance to the ongoing theoretical and experimental searches of the unconventional quantum states.

Bibliography

- [1] A. W. Sandvik, Phys. Rev. B **56**, 11678 (1997).
- [2] E. M. Stoudenmire and S. R. White, Annu. Rev. Condens. Matter Phys. **3**, 111 (2012).
- [3] S. R. White and A. L. Chernyshev, Phys. Rev. Lett. **99**, 127004 (2007).
- [4] E. H. da Silva Neto, R. Comin, F. He, R. Sutarto, Y. Jiang, R. L. Greene, G. A. Sawatzky, and A. Damascelli, Science **347**, 282 (2015).
- [5] T. Xiang and J. Wheatley, Phys. Rev. B **54**, R12653 (1996).
- [6] P. W. Leung, B. O. Wells, and R. J. Gooding, Phys. Rev. B **56**, 6320 (1997).
- [7] P. A. Lee, N. Nagaosa, and X.-G. Wen, Rev. Mod. Phys. **78**, 17 (2006).
- [8] T. Tohyama, Phys. Rev. B **70**, 174517 (2004).
- [9] T. Halloran, F. Desrochers, E. Z. Zhang, T. Chen, L. E. Chern, Z. Xu, B. Winn, M. Graves-Brook, M. B. Stone, A. I. Kolesnikov, et al., Proc. Natl. Acad. Sci. U.S.A. **120**, e2215509119 (2023).
- [10] S. Jiang, D. J. Scalapino, and S. R. White, Proc. Natl. Acad. Sci. U.S.A. **118**, e2109978118 (2021).
- [11] S. Jiang, D. J. Scalapino, and S. R. White, Phys. Rev. B **106**, 174507 (2022).
- [12] S. Jiang, D. J. Scalapino, and S. R. White, Phys. Rev. B **108**, L161111 (2023).
- [13] S. Jiang, J. Romhányi, S. R. White, M. E. Zhitomirsky, and A. L. Chernyshev, Phys. Rev. Lett. **130**, 116701 (2023).
- [14] S. Jiang, S. R. White, and A. L. Chernyshev, Phys. Rev. B **108**, L180406 (2023).
- [15] E. Fradkin, S. A. Kivelson, and J. M. Tranquada, Rev. Mod. Phys. **87**, 457 (2015).
- [16] D. J. Scalapino, Rev. Mod. Phys. **84**, 1383 (2012).
- [17] K. Penc and A. M. Läuchli, in *Introduction to Frustrated Magnetism: Materials, Experiments, Theory*, edited by C. Lacroix, P. Mendels, and F. Mila (Springer-Verlag Berlin Heidelberg, 2011), chap. Spin Nematic Phases in Quantum Spin Systems, p. 331.

- [18] L. Balents, *Nature* **464**, 199 (2010).
- [19] R. B. Laughlin, *Phys. Rev. Lett.* **50**, 1395 (1983).
- [20] Y. Cao, V. Fatemi, S. Fang, K. Watanabe, T. Taniguchi, E. Kaxiras, and P. Jarillo-Herrero, *Nature* **556**, 43 (2018).
- [21] E. Dagotto, *Rev. Mod. Phys.* **66**, 763 (1994).
- [22] J. E. Hirsch, *Phys. Rev. B* **31**, 4403 (1985).
- [23] S. R. White, D. J. Scalapino, R. L. Sugar, E. Y. Loh, J. E. Gubernatis, and R. T. Scalettar, *Phys. Rev. B* **40**, 506 (1989).
- [24] C. Lanczos, *J. Res. Natl. Inst. Stand. Technol.* **45** (1950).
- [25] A. Wietek, S. Capponi, and A. M. Läuchli, *Phys. Rev. X* **14**, 021010 (2024).
- [26] M. Troyer and U.-J. Wiese, *Phys. Rev. Lett.* **94**, 170201 (2005).
- [27] M. Qin, C.-M. Chung, H. Shi, E. Vitali, C. Hubig, U. Schollwöck, S. R. White, and S. Zhang (Simons Collaboration on the Many-Electron Problem), *Phys. Rev. X* **10**, 031016 (2020).
- [28] H. Xu, C.-M. Chung, M. Qin, U. Schollwöck, S. R. White, and S. Zhang, *Science* **384**, eadh7691 (2024).
- [29] S. R. White, *Phys. Rev. Lett.* **69**, 2863 (1992).
- [30] J. Eisert, M. Cramer, and M. B. Plenio, *Rev. Mod. Phys.* **82**, 277 (2010).
- [31] K. G. Wilson, *Rev. Mod. Phys.* **47**, 773 (1975).
- [32] F. Verstraete and J. I. Cirac, *Phys. Rev. B* **73**, 094423 (2006).
- [33] H. A. Kramers and G. H. Wannier, *Phys. Rev.* **60**, 252 (1941).
- [34] R. Baxter, *Physica A Stat. Mech. Appl.* **106**, 18 (1981).
- [35] B. A. Jones, Ph.D. thesis, Cornell University (1988).
- [36] R. Orús, *Nat. Rev. Phys.* **1**, 538 (2019).
- [37] S. Östlund and S. Rommer, *Phys. Rev. Lett.* **75**, 3537 (1995).
- [38] G. Vidal, J. I. Latorre, E. Rico, and A. Kitaev, *Phys. Rev. Lett.* **90**, 227902 (2003).
- [39] M. B. Hastings, *J. Stat. Mech.: Theory Exp.* **2007**, P08024 (2007).
- [40] G. Vidal, *Phys. Rev. Lett.* **93**, 040502 (2004).
- [41] S. R. White and A. E. Feiguin, *Phys. Rev. Lett.* **93**, 076401 (2004).

- [42] J. Haegeman, J. I. Cirac, T. J. Osborne, I. Pižorn, H. Verschelde, and F. Verstraete, Phys. Rev. Lett. **107**, 070601 (2011).
- [43] S. R. White, Phys. Rev. Lett. **102**, 190601 (2009).
- [44] F. Verstraete, J. J. García-Ripoll, and J. I. Cirac, Phys. Rev. Lett. **93**, 207204 (2004).
- [45] T. Barthel, New J. Phys. **15**, 073010 (2013).
- [46] J. I. Cirac, D. Pérez-García, N. Schuch, and F. Verstraete, Rev. Mod. Phys. **93**, 045003 (2021).
- [47] G. Vidal, Phys. Rev. Lett. **99**, 220405 (2007).
- [48] U. Schollwöck, Ann. Phys. **326**, 96 (2011).
- [49] I. P. McCulloch, arXiv:0804.2509 (2008).
- [50] M. P. Zaletel and F. Pollmann, Phys. Rev. Lett. **124**, 037201 (2020).
- [51] H. C. Jiang, Z. Y. Weng, and T. Xiang, Phys. Rev. Lett. **101**, 090603 (2008).
- [52] W.-Y. Liu, S.-J. Dong, Y.-J. Han, G.-C. Guo, and L. He, Phys. Rev. B **95**, 195154 (2017).
- [53] L. Savary and L. Balents, Rep. Prog. Phys. **80**, 016502 (2016).
- [54] S. Yan, D. A. Huse, and S. R. White, Science **332**, 1173 (2011).
- [55] Y.-C. He, M. P. Zaletel, M. Oshikawa, and F. Pollmann, Phys. Rev. X **7**, 031020 (2017).
- [56] H. C. Jiang, Z. Y. Weng, and D. N. Sheng, Phys. Rev. Lett. **101**, 117203 (2008).
- [57] H.-C. Jiang, H. Yao, and L. Balents, Phys. Rev. B **86**, 024424 (2012).
- [58] S.-S. Gong, W. Zhu, D. N. Sheng, O. I. Motrunich, and M. P. A. Fisher, Phys. Rev. Lett. **113**, 027201 (2014).
- [59] W.-Y. Liu, J. Hasik, S.-S. Gong, D. Poilblanc, W.-Q. Chen, and Z.-C. Gu, Phys. Rev. X **12**, 031039 (2022).
- [60] Z. Zhu and S. R. White, Phys. Rev. B **92**, 041105(R) (2015).
- [61] Y.-F. Jiang and H.-C. Jiang, Phys. Rev. B **107**, L140411 (2023).
- [62] Z. Zhu, P. A. Maksimov, S. R. White, and A. L. Chernyshev, Phys. Rev. Lett. **119**, 157201 (2017).
- [63] P. A. Maksimov, Z. Zhu, S. R. White, and A. L. Chernyshev, Phys. Rev. X **9**, 021017 (2019).

- [64] T. Xie, A. Eberharter, J. Xing, S. Nishimoto, M. Brando, P. Khanenko, J. Sichelschmidt, A. Turrini, D. Mazzone, P. Naumov, et al., *npj Quantum Mater.* **8**, 48 (2023).
- [65] E. Lieb and D. Mattis, *J. Math. Phys.* **3**, 749 (1962).
- [66] F. Chen, F. D. M. Haldane, and D. N. Sheng, arXiv:2311.15092 (2023).
- [67] Z. Zhu, D. A. Huse, and S. R. White, *Phys. Rev. Lett.* **110**, 127205 (2013).
- [68] Z. Zhu, D. A. Huse, and S. R. White, *Phys. Rev. Lett.* **111**, 257201 (2013).
- [69] Z. Zhu, P. A. Maksimov, S. R. White, and A. L. Chernyshev, *Phys. Rev. Lett.* **120**, 207203 (2018).
- [70] B.-X. Zheng, C.-M. Chung, P. Corboz, G. Ehlers, M.-P. Qin, R. M. Noack, H. Shi, S. R. White, S. Zhang, and G. K.-L. Chan, *Science* **358**, 1155 (2017).
- [71] D. P. Arovas, E. Berg, S. A. Kivelson, and S. Raghu, *Annu. Rev. Condens. Matter Phys.* **13**, 239 (2022).
- [72] M. Qin, T. Schäfer, S. Andergassen, P. Corboz, and E. Gull, *Annu. Rev. Condens. Matter Phys.* **13**, 275 (2022).
- [73] H.-C. Jiang and T. P. Devereaux, *Science* **365**, 1424 (2019).
- [74] Y.-F. Jiang, J. Zaanen, T. P. Devereaux, and H.-C. Jiang, *Phys. Rev. Research* **2**, 033073 (2020).
- [75] E. W. Huang, C. B. Mendl, H.-C. Jiang, B. Moritz, and T. P. Devereaux, *npj Quantum Mater.* **3**, 1 (2018).
- [76] J. F. Dodaro, H.-C. Jiang, and S. A. Kivelson, *Phys. Rev. B* **95**, 155116 (2017).
- [77] C.-M. Chung, M. Qin, S. Zhang, U. Schollwöck, and S. R. White (The Simons Collaboration on the Many-Electron Problem), *Phys. Rev. B* **102**, 041106(R) (2020).
- [78] H.-C. Jiang, Z.-Y. Weng, and S. A. Kivelson, *Phys. Rev. B* **98**, 140505(R) (2018).
- [79] K. Ido, T. Ohgoe, and M. Imada, *Phys. Rev. B* **97**, 045138 (2018).
- [80] L. F. Tocchio, F. Becca, and S. Sorella, *Phys. Rev. B* **94**, 195126 (2016).
- [81] P. Corboz, T. M. Rice, and M. Troyer, *Phys. Rev. Lett.* **113**, 046402 (2014).
- [82] P. Corboz, S. R. White, G. Vidal, and M. Troyer, *Phys. Rev. B* **84**, 041108(R) (2011).
- [83] J. P. F. LeBlanc, A. E. Antipov, F. Becca, I. W. Bulik, G. K.-L. Chan, C.-M. Chung, Y. Deng, M. Ferrero, T. M. Henderson, C. A. Jiménez-Hoyos, et al. (Simons Collaboration on the Many-Electron Problem), *Phys. Rev. X* **5**, 041041 (2015).

- [84] S. R. White and D. J. Scalapino, Phys. Rev. B **79**, 220504(R) (2009).
- [85] B. Ponsioen, S. S. Chung, and P. Corboz, Phys. Rev. B **100**, 195141 (2019).
- [86] A. Himeda, T. Kato, and M. Ogata, Phys. Rev. Lett. **88**, 117001 (2002).
- [87] X. Y. Xu and T. Grover, Phys. Rev. Lett. **126**, 217002 (2021).
- [88] H.-C. Jiang and S. A. Kivelson, Phys. Rev. Lett. **127**, 097002 (2021).
- [89] T. Tohyama, M. Mori, and S. Sota, Phys. Rev. B **97**, 235137 (2018).
- [90] J. Zaanen and O. Gunnarsson, Phys. Rev. B **40**, 7391 (1989).
- [91] D. Poilblanc and T. M. Rice, Phys. Rev. B **39**, 9749 (1989).
- [92] K. Machida, Physica C Supercond. **158**, 192 (1989).
- [93] M. Kato, K. Machida, H. Nakanishi, and M. Fujita, J. Phys. Soc. Japan **59**, 1047 (1990).
- [94] S. R. White, Phys. Rev. Lett. **69**, 2863 (1992).
- [95] S. R. White, Phys. Rev. B **48**, 10345 (1993).
- [96] S. R. White and D. J. Scalapino, Phys. Rev. Lett. **80**, 1272 (1998).
- [97] F. Becca, L. Capriotti, and S. Sorella, Phys. Rev. Lett. **87**, 167005 (2001).
- [98] S. Sorella, G. B. Martins, F. Becca, C. Gazza, L. Capriotti, A. Parola, and E. Dagotto, Phys. Rev. Lett. **88**, 117002 (2002).
- [99] C.-P. Chou and T.-K. Lee, Phys. Rev. B **81**, 060503(R) (2010).
- [100] K. Ido, T. Ohgoe, and M. Imada, Phys. Rev. B **97**, 045138 (2018).
- [101] L. F. Tocchio, A. Montorsi, and F. Becca, SciPost Phys. **7**, 21 (2019).
- [102] S. R. White and D. J. Scalapino, Phys. Rev. B **60**, R753 (1999).
- [103] G. Psaltakis and E. Fenton, J. Phys. C: Solid State Phys. **16**, 3913 (1983).
- [104] S.-C. Zhang, Science **275**, 1089 (1997).
- [105] A. Aperis, G. Varelogiannis, P. Littlewood, and B. Simons, J. Phys. Condens. Matter. **20**, 434235 (2008).
- [106] W. Rowe, J. Knolle, I. Eremin, and P. J. Hirschfeld, Phys. Rev. B **86**, 134513 (2012).
- [107] D. E. Almeida, R. M. Fernandes, and E. Miranda, Phys. Rev. B **96**, 014514 (2017).
- [108] M. Fishman, S. R. White, and E. M. Stoudenmire, SciPost Phys. Codebases p. 4 (2022).

- [109] D. J. Scalapino, Phys. Rep. **250**, 329 (1995).
- [110] S. R. White, R. M. Noack, and D. J. Scalapino, Phys. Rev. Lett. **73**, 886 (1994).
- [111] T. Xiang and N. d’Ambrumenil, Phys. Rev. B **45**, 8150 (1992).
- [112] D. Sénéchal, P.-L. Lavertu, M.-A. Marois, and A.-M. S. Tremblay, Phys. Rev. Lett. **94**, 156404 (2005).
- [113] A. Foley, S. Verret, A.-M. S. Tremblay, and D. Sénéchal, Phys. Rev. B **99**, 184510 (2019).
- [114] B. Kyung, Phys. Rev. B **62**, 9083 (2000).
- [115] M. Kato and K. Machida, Phys. Rev. B **37**, 1510 (1988).
- [116] K. Machida, K. Nokura, and T. Matsubara, Phys. Rev. B **22**, 2307 (1980).
- [117] M. Murakami and H. Fukuyama, J. Phys. Soc. Japan **67**, 2784 (1998).
- [118] E. Jeckelmann, D. J. Scalapino, and S. R. White, Phys. Rev. B **58**, 9492 (1998).
- [119] S. R. White and D. J. Scalapino, Phys. Rev. B **55**, 6504 (1997).
- [120] S. Krinner, T. Esslinger, and J.-P. Brantut, J. Phys. Condens. Matter. **29**, 343003 (2017).
- [121] V. I. Belinicher, A. L. Chernyshev, and V. A. Shubin, Phys. Rev. B **53**, 335 (1996).
- [122] F. C. Zhang and T. M. Rice, Phys. Rev. B **37**, 3759 (1988).
- [123] Y.-F. Jiang, T. P. Devereaux, and H.-C. Jiang, Phys. Rev. B **109**, 085121 (2024).
- [124] X. Lu, F. Chen, W. Zhu, D. N. Sheng, and S.-S. Gong, Phys. Rev. Lett. **132**, 066002 (2024).
- [125] S. Gong, W. Zhu, and D. N. Sheng, Phys. Rev. Lett. **127**, 097003 (2021).
- [126] H.-C. Jiang and S. A. Kivelson, Phys. Rev. Lett. **127**, 097002 (2021).
- [127] H.-C. Jiang, S. A. Kivelson, and D.-H. Lee, Phys. Rev. B **108**, 054505 (2023).
- [128] E. W. Huang, T. Liu, W. O. Wang, H.-C. Jiang, P. Mai, T. A. Maier, S. Johnston, B. Moritz, and T. P. Devereaux, Phys. Rev. B **107**, 085126 (2023).
- [129] P. Mai, S. Karakuzu, G. Balduzzi, S. Johnston, and T. A. Maier, Proc. Natl. Acad. Sci. U.S.A. **119**, e2112806119 (2022).
- [130] W. He, J. Wen, H.-C. Jiang, G. Xu, W. Tian, T. Taniguchi, Y. Ikeda, M. Fujita, and Y. S. Lee, arXiv:2107.10264 (2021).

- [131] S. Karakuzu, A. Tanjaroon Ly, P. Mai, J. Neuhaus, T. A. Maier, and S. Johnston, *Commun. Phys.* **5**, 1 (2022).
- [132] V. J. Emery, *Phys. Rev. Lett.* **58**, 2794 (1987).
- [133] E. W. Huang, C. B. Mendl, S. Liu, S. Johnston, H.-C. Jiang, B. Moritz, and T. P. Devereaux, *Science* **358**, 1161 (2017).
- [134] P. Mai, G. Balduzzi, S. Johnston, and T. A. Maier, *npj Quantum Mater.* **6**, 1 (2021).
- [135] Z.-H. Cui, C. Sun, U. Ray, B.-X. Zheng, Q. Sun, and G. K.-L. Chan, *Phys. Rev. Res.* **2**, 043259 (2020).
- [136] A. Chiciak, E. Vitali, and S. Zhang, *Phys. Rev. B* **102**, 214512 (2020).
- [137] S. R. White and D. J. Scalapino, *Phys. Rev. B* **92**, 205112 (2015).
- [138] N. Kowalski, S. S. Dash, P. Sémon, D. Sénéchal, and A.-M. Tremblay, *Proc. Natl. Acad. Sci. U.S.A.* **118**, e2106476118 (2021).
- [139] A. Biborski, M. Zegrodnik, and J. Spałek, *Phys. Rev. B* **101**, 214504 (2020).
- [140] S. Li, A. Nocera, U. Kumar, and S. Johnston, *Commun. Phys.* **4**, 217 (2021).
- [141] N. B. Brookes, G. Ghiringhelli, O. Tjernberg, L. H. Tjeng, T. Mizokawa, T. W. Li, and A. A. Menovsky, *Phys. Rev. Lett.* **87**, 237003 (2001).
- [142] L. H. Tjeng, B. Sinkovic, N. B. Brookes, J. B. Goedkoop, R. Hesper, E. Pellegrin, F. M. F. de Groot, S. Altieri, S. L. Hulbert, E. Shekel, et al., *Phys. Rev. Lett.* **78**, 1126 (1997).
- [143] Y. Harada, K. Okada, R. Eguchi, A. Kotani, H. Takagi, T. Takeuchi, and S. Shin, *Phys. Rev. B* **66**, 165104 (2002).
- [144] E. Arrigoni, M. Aichhorn, M. Daghofer, and W. Hanke, *New J. Phys.* **11**, 055066 (2009).
- [145] I. J. Hamad, L. O. Manuel, and A. A. Aligia, *Phys. Rev. Lett.* **120**, 177001 (2018).
- [146] V. Marino, F. Becca, and L. F. Tocchio, *SciPost Phys.* **12**, 180 (2022).
- [147] S. Sorella, *arXiv:2101.07045* (2021).
- [148] H.-C. Jiang and S. A. Kivelson, *Proc. Natl. Acad. Sci. U.S.A.* **119**, e2109406119 (2022).
- [149] H. Xu, H. Shi, E. Vitali, M. Qin, and S. Zhang, *Phys. Rev. Res.* **4**, 013239 (2022).
- [150] C. Peng, Y. Wang, J. Wen, Y. S. Lee, T. P. Devereaux, and H.-C. Jiang, *Phys. Rev. B* **107**, L201102 (2023).
- [151] A. Wietek, Y.-Y. He, S. R. White, A. Georges, and E. M. Stoudenmire, *Phys. Rev. X* **11**, 031007 (2021).

- [152] S. Raghu, S. A. Kivelson, and D. J. Scalapino, *Phys. Rev. B* **81**, 224505 (2010).
- [153] M. Danilov, E. G. van Loon, S. Brener, S. Iskakov, M. I. Katsnelson, and A. I. Liechtenstein, *npj Quantum Mater.* **7**, 50 (2022).
- [154] W.-C. Chen, Y. Wang, and C.-C. Chen, *Phys. Rev. B* **108**, 064514 (2023).
- [155] D.-W. Qu, B.-B. Chen, X. Lu, Q. Li, Y. Qi, S.-S. Gong, W. Li, and G. Su, *arXiv:2211.06322* (2022).
- [156] X. Lu, D.-W. Qu, Y. Qi, W. Li, and S.-S. Gong, *Phys. Rev. B* **107**, 125114 (2023).
- [157] Y. Chang and L. K. Wagner, *arXiv:2302.02899* (2023).
- [158] H. J. Changlani, H. Zheng, and L. K. Wagner, *J. Chem. Phys.* **143**, 102814 (2015).
- [159] Z.-H. Cui, H. Zhai, X. Zhang, and G. K.-L. Chan, *Science* **377**, 1192 (2022).
- [160] H. Zheng, H. J. Changlani, K. T. Williams, B. Busemeyer, and L. K. Wagner, *Front. Phys.* **6** (2018).
- [161] M. Hirayama, Y. Nomura, and R. Arita, *Front. Phys.* p. 49 (2022).
- [162] R. C. Sawaya and S. R. White, *Phys. Rev. B* **105**, 045145 (2022).
- [163] Y. F. Kung, C.-C. Chen, Y. Wang, E. W. Huang, E. A. Nowadnick, B. Moritz, R. T. Scalettar, S. Johnston, and T. P. Devereaux, *Phys. Rev. B* **93**, 155166 (2016).
- [164] W. Hanke, M. L. Kiesel, M. Aichhorn, S. Brehm, and E. Arrighoni, *Eur. Phys. J.: Spec. Top.* **188**, 15 (2010).
- [165] J. Zaanen, G. A. Sawatzky, and J. W. Allen, *Phys. Rev. Lett.* **55**, 418 (1985).
- [166] H.-C. Jiang, *Phys. Rev. B* **107**, 214504 (2023).
- [167] J.-P. Song, S. Mazumdar, and R. T. Clay, *Phys. Rev. B* **104**, 104504 (2021).
- [168] B. Ponsioen, S. S. Chung, and P. Corboz, *Phys. Rev. B* **108**, 205154 (2023).
- [169] P.-O. Löwdin, *J. Chem. Phys.* **18**, 365 (1950).
- [170] F. Werner, O. Parcollet, A. Georges, and S. R. Hassan, *Phys. Rev. Lett.* **95**, 056401 (2005).
- [171] J. Hirsch, *Phys. C: Supercond. Appl.* **158**, 326 (1989).
- [172] R. B. Laughlin, *Phys. Rev. Lett.* **112**, 017004 (2014).
- [173] S. L. Sondhi, M. P. Gelfand, H. Q. Lin, and D. K. Campbell, *Phys. Rev. B* **51**, 5943 (1995).

- [174] P.-G. De Gennes and J. Prost, *The physics of liquid crystals*, 83 (Oxford university press, 1993).
- [175] D. Andrienko, *J. Mol. Liq.* **267**, 520 (2018).
- [176] E. Fradkin, S. A. Kivelson, M. J. Lawler, J. P. Eisenstein, and A. P. Mackenzie, *Annu. Rev. Condens. Matter Phys.* **1**, 153 (2010).
- [177] J.-H. Chu, H.-H. Kuo, J. G. Analytis, and I. R. Fisher, *Science* **337**, 710 (2012).
- [178] R. M. Fernandes, A. V. Chubukov, and J. Schmalian, *Nat. Phys.* **10**, 97 (2014).
- [179] S. Mukhopadhyay, R. Sharma, C. K. Kim, S. D. Edkins, M. H. Hamidian, H. Eisaki, S. ichi Uchida, E.-A. Kim, M. J. Lawler, A. P. Mackenzie, et al., *Proc. Natl. Acad. Sci. U.S.A.* **116**, 13249 (2019).
- [180] F. Mila, *Physics* **10**, 64 (2017).
- [181] R. Nath, A. A. Tsirlin, H. Rosner, and C. Geibel, *Phys. Rev. B* **78**, 064422 (2008).
- [182] L. E. Svistov, T. Fujita, H. Yamaguchi, S. Kimura, K. Omura, A. Prokofiev, A. I. Smirnov, Z. Honda, and M. Hagiwara, *JETP letters* **93**, 21 (2011).
- [183] M. Yoshida, K. Nawa, H. Ishikawa, M. Takigawa, M. Jeong, S. Krämer, M. Horvatić, C. Berthier, K. Matsui, T. Goto, et al., *Phys. Rev. B* **96**, 180413(R) (2017).
- [184] A. Orlova, E. L. Green, J. M. Law, D. I. Gorbunov, G. Chanda, S. Krämer, M. Horvatić, R. K. Kremer, J. Wosnitza, and G. L. J. A. Rikken, *Phys. Rev. Lett.* **118**, 247201 (2017).
- [185] Y. Kohama, H. Ishikawa, A. Matsuo, K. Kindo, N. Shannon, and Z. Hiroi, *Proc. Natl. Acad. Sci. U.S.A.* **116**, 10686 (2019).
- [186] K. Y. Povarov, V. K. Bhartiya, Z. Yan, and A. Zheludev, *Phys. Rev. B* **99**, 024413 (2019).
- [187] V. K. Bhartiya, K. Y. Povarov, D. Blosser, S. Bettler, Z. Yan, S. Gvasaliya, S. Raymond, E. Ressouche, K. Beauvois, J. Xu, et al., *Phys. Rev. Research* **1**, 033078 (2019).
- [188] F. Landolt, S. Bettler, Z. Yan, S. Gvasaliya, A. Zheludev, S. Mishra, I. Sheikin, S. Krämer, M. Horvatić, A. Gazizulina, et al., *Phys. Rev. B* **102**, 094414 (2020).
- [189] K. M. Ranjith, F. Landolt, S. Raymond, A. Zheludev, and M. Horvatić, *Phys. Rev. B* **105**, 134429 (2022).
- [190] D. Flavián, S. Hayashida, L. Huberich, D. Blosser, K. Y. Povarov, Z. Yan, S. Gvasaliya, and A. Zheludev, *Phys. Rev. B* **101**, 224408 (2020).
- [191] A. F. Andreev and I. M. Lifshitz, *Sov. Phys. JETP* **29**, 1107 (1969).
- [192] A. J. Leggett, *Phys. Rev. Lett.* **25**, 1543 (1970).

- [193] J. Léonard, A. Morales, P. Zupancic, T. Esslinger, and T. Donner, *Nature* **543**, 87 (2017).
- [194] M. A. Norcia, C. Politi, L. Klaus, E. Poli, M. Sohmen, M. J. Mark, R. N. Bisset, L. Santos, and F. Ferlino, *Nature* **596**, 357 (2021).
- [195] J. Knolle and R. Moessner, *Annu. Rev. Condens. Matter Phys.* **10**, 451 (2019).
- [196] M. Blume and Y. Y. Hsieh, *J. Appl. Phys.* **40**, 1249 (1969).
- [197] A. F. Andreev and I. A. Grishchuk, *Sov. Phys. JETP* **60**, 267 (1984).
- [198] A. V. Chubukov, *Phys. Rev. B* **44**, 4693 (1991).
- [199] V. Zapf, M. Jaime, and C. D. Batista, *Rev. Mod. Phys.* **86**, 563 (2014).
- [200] M. Wortis, *Phys. Rev.* **132**, 85 (1963).
- [201] D. C. Mattis, *The theory of magnetism made simple: an introduction to physical concepts and to some useful mathematical methods* (World Scientific Publishing, Singapore, 2006), ISBN 981-238-579-7.
- [202] N. Shannon, T. Momoi, and P. Sindzingre, *Phys. Rev. Lett.* **96**, 027213 (2006).
- [203] P. Sindzingre, L. Seabra, N. Shannon, and T. Momoi, *J. Phys. Conf. Ser.* **145**, 012048 (2009).
- [204] Y. Iqbal, P. Ghosh, R. Narayanan, B. Kumar, J. Reuther, and R. Thomale, *Phys. Rev. B* **94**, 224403 (2016).
- [205] R. O. Kuzian and S.-L. Drechsler, *Phys. Rev. B* **75**, 024401 (2007).
- [206] T. Hikihara, L. Kecke, T. Momoi, and A. Furusaki, *Phys. Rev. B* **78**, 144404 (2008).
- [207] T. Momoi, P. Sindzingre, and K. Kubo, *Phys. Rev. Lett.* **108**, 057206 (2012).
- [208] R. Shindou and T. Momoi, *Phys. Rev. B* **80**, 064410 (2009).
- [209] T. Momoi and N. Shannon, *Prog. Theor. Phys.* **159**, 72 (2005).
- [210] J. Sudan, A. Lüscher, and A. M. Läuchli, *Phys. Rev. B* **80**, 140402(R) (2009).
- [211] L. Balents and O. A. Starykh, *Phys. Rev. Lett.* **116**, 177201 (2016).
- [212] M. E. Zhitomirsky and H. Tsunetsugu, *EPL (Europhysics Letters)* **92**, 37001 (2010).
- [213] H. T. Ueda and K. Totsuka, *Phys. Rev. B* **80**, 014417 (2009).
- [214] O. Janson, S. Furukawa, T. Momoi, P. Sindzingre, J. Richter, and K. Held, *Phys. Rev. Lett.* **117**, 037206 (2016).
- [215] R. Bendjama, B. Kumar, and F. Mila, *Phys. Rev. Lett.* **95**, 110406 (2005).

- [216] C. Knetter, A. Bühler, E. Müller-Hartmann, and G. S. Uhrig, Phys. Rev. Lett. **85**, 3958 (2000).
- [217] K. Totsuka, S. Miyahara, and K. Ueda, Phys. Rev. Lett. **86**, 520 (2001).
- [218] J. Richter, R. Darradi, J. Schulenburg, D. J. J. Farnell, and H. Rosner, Phys. Rev. B **81**, 174429 (2010).
- [219] J. F. Annett, *Superconductivity, Superfluids and Condensates* (Oxford University Press Inc., New York, 2006), ISBN 9780198507567.
- [220] J. R. Taylor, *Scattering Theory: The Quantum Theory of Nonrelativistic Collisions* (Dover Publications, 2006), ISBN 978-0486450131.
- [221] E. M. Lifshitz and L. P. Pitaevskii, in *Statistical Physics, v. 2*, edited by L. D. Landau and E. M. Lifshitz (Pergamon Press, Oxford, 1980), pp. 85–140, ISBN 978-0-08-050350-9.
- [222] H. T. Ueda and T. Momoi, Phys. Rev. B **87**, 144417 (2013).
- [223] In a similar setting, an earlier work has suggested *expansion* of the nematic phase *below* the h_{c1} -line [212], but it neglected attraction effects between the single spin flips and pair BEC.
- [224] P. Anderson, Mater. Res. Bull. **8**, 153 (1973).
- [225] M. R. Norman, Rev. Mod. Phys. **88**, 041002 (2016).
- [226] Y. Zhou, K. Kanoda, and T.-K. Ng, Rev. Mod. Phys. **89**, 025003 (2017).
- [227] A. Kitaev, Ann. Phys. **321**, 2 (2006), ISSN 0003-4916.
- [228] L. Capriotti, F. Becca, A. Parola, and S. Sorella, Phys. Rev. Lett. **87**, 097201 (2001).
- [229] M. Mambrini, A. Läuchli, D. Poilblanc, and F. Mila, Phys. Rev. B **74**, 144422 (2006).
- [230] K. Kodama, M. Takigawa, M. Horvatić, C. Berthier, H. Kageyama, Y. Ueda, S. Miyahara, F. Becca, and F. Mila, Science **298**, 395 (2002).
- [231] Y. H. Matsuda, N. Abe, S. Takeyama, H. Kageyama, P. Corboz, A. Honecker, S. R. Manmana, G. R. Foltin, K. P. Schmidt, and F. Mila, Phys. Rev. Lett. **111**, 137204 (2013).
- [232] M. Jaime, R. Daou, S. A. Crooker, F. Weickert, A. Uchida, A. E. Feiguin, C. D. Batista, H. A. Dabkowska, and B. D. Gaulin, Proc. Natl. Acad. Sci. U.S.A. **109**, 12404 (2012).
- [233] F. Ferrari, S. Bieri, and F. Becca, Phys. Rev. B **96**, 104401 (2017).
- [234] M. E. Zhitomirsky and H. Tsunetsugu, EPL (Europhysics Letters) **92**, 37001 (2010).

- [235] Y. Kohama, H. Ishikawa, A. Matsuo, K. Kindo, N. Shannon, and Z. Hiroi, *Proc. Natl. Acad. Sci. U.S.A.* **116**, 10686 (2019).
- [236] C. L. Henley, *J. Appl. Phys.* **61**, 3962 (1987).
- [237] C. L. Henley, *Phys. Rev. Lett.* **62**, 2056 (1989).
- [238] O. A. Starykh, *Rep. Prog. Phys.* **78**, 052502 (2015).
- [239] A. W. C. Wong, Z. Hao, and M. J. P. Gingras, *Phys. Rev. B* **88**, 144402 (2013).
- [240] K. A. Ross, L. Savary, B. D. Gaulin, and L. Balents, *Phys. Rev. X* **1**, 021002 (2011).
- [241] J. G. Rau and M. J. Gingras, *Annu. Rev. Condens. Matter Phys.* **10**, 357 (2019).
- [242] A. M. Hallas, J. Gaudet, and B. D. Gaulin, *Annu. Rev. Condens. Matter Phys.* **9**, 105 (2018).
- [243] J. G. Rau, R. Moessner, and P. A. McClarty, *Phys. Rev. B* **100**, 104423 (2019).
- [244] J. G. Rau, P. A. McClarty, and R. Moessner, *Phys. Rev. Lett.* **121**, 237201 (2018).
- [245] R. Schick, O. Götze, T. Ziman, R. Zinke, J. Richter, and M. E. Zhitomirsky, *Phys. Rev. B* **106**, 094431 (2022).
- [246] W. Witczak-Krempa, G. Chen, Y. B. Kim, and L. Balents, *Annu. Rev. Condens. Matter Phys.* **5**, 57 (2014).
- [247] R. Schaffer, E. K.-H. Lee, B.-J. Yang, and Y. B. Kim, *Rep. Prog. Phys.* **79**, 094504 (2016).
- [248] J. G. Rau, E. K.-H. Lee, and H.-Y. Kee, *Annu. Rev. Condens. Matter Phys.* **7**, 195 (2016).
- [249] S. M. Winter, A. A. Tsirlin, M. Daghofer, J. van den Brink, Y. Singh, P. Gegenwart, and R. Valentí, *J. Phys. Condens. Matter* **29**, 493002 (2017).
- [250] H. Liu and G. Khaliullin, *Phys. Rev. B* **97**, 014407 (2018).
- [251] H. Liu, J. Chaloupka, and G. Khaliullin, *Phys. Rev. Lett.* **125**, 047201 (2020).
- [252] X. Zhang, Y. Xu, T. Halloran, R. Zhong, C. Broholm, R. Cava, N. Drichko, and N. Armitage, *Nat. Mater.* **22**, 58 (2023).
- [253] R. Zhong, T. Gao, N. P. Ong, and R. J. Cava, *Sci. Adv.* **6**, eaay6953 (2020).
- [254] H. S. Nair, J. M. Brown, E. Coldren, G. Hester, M. P. Gelfand, A. Podlesnyak, Q. Huang, and K. A. Ross, *Phys. Rev. B* **97**, 134409 (2018).
- [255] X. Wang, R. Sharma, P. Becker, L. Bohatý, and T. Lorenz, *Phys. Rev. Mater.* **7**, 024402 (2023).

- [256] H. Yang, C. Kim, Y. Choi, J. H. Lee, G. Lin, J. Ma, M. Kratochvílová, P. Proschek, E.-G. Moon, K. H. Lee, et al., *Phys. Rev. B* **106**, L081116 (2022).
- [257] W. Yao, Y. Zhao, Y. Qiu, C. Balz, J. R. Stewart, J. W. Lynn, and Y. Li, *Phys. Rev. Res.* **5**, L022045 (2023).
- [258] M. Songvilay, J. Robert, S. Petit, J. A. Rodriguez-Rivera, W. D. Ratcliff, F. Damay, V. Balédent, M. Jiménez-Ruiz, P. Lejay, E. Pachoud, et al., *Phys. Rev. B* **102**, 224429 (2020).
- [259] X. Li, Y. Gu, Y. Chen, V. O. Garlea, K. Iida, K. Kamazawa, Y. Li, G. Deng, Q. Xiao, X. Zheng, et al., *Phys. Rev. X* **12**, 041024 (2022).
- [260] L.-P. Regnault, C. Boullier, and J. Lorenzo, *Heliyon* **4**, e00507 (2018).
- [261] S. Das, S. Voleti, T. Saha-Dasgupta, and A. Paramakanti, *Phys. Rev. B* **104**, 134425 (2021).
- [262] P. A. Maksimov, A. V. Ushakov, Z. V. Pchelkina, Y. Li, S. M. Winter, and S. V. Streltsov, *Phys. Rev. B* **106**, 165131 (2022).
- [263] P. A. Maksimov and A. L. Chernyshev, *Phys. Rev. Res.* **2**, 033011 (2020).
- [264] L. Regnault and J. Rossat-Mignod, in *Magnetic Properties of Layered Transition Metal Compounds* (Springer, 1990), pp. 271–321.
- [265] A. L. Chernyshev, M. E. Zhitomirsky, N. Martin, and L.-P. Regnault, *Phys. Rev. Lett.* **109**, 097201 (2012).
- [266] Z. Weihong, J. Oitmaa, and C. J. Hamer, *Phys. Rev. B* **44**, 11869 (1991).
- [267] R. R. P. Singh, Z. Weihong, C. J. Hamer, and J. Oitmaa, *Phys. Rev. B* **60**, 7278 (1999).
- [268] J. Fouet, P. Sindzingre, and C. Lhuillier, *Eur. Phys. J. B* **20**, 241 (2001).
- [269] A. Mulder, R. Ganesh, L. Capriotti, and A. Paramakanti, *Phys. Rev. B* **81**, 214419 (2010).
- [270] J. Oitmaa and R. R. P. Singh, *Phys. Rev. B* **84**, 094424 (2011).
- [271] D. C. Cabra, C. A. Lamas, and H. D. Rosales, *Phys. Rev. B* **83**, 094506 (2011).
- [272] C. N. Varney, K. Sun, V. Galitski, and M. Rigol, *Phys. Rev. Lett.* **107**, 077201 (2011).
- [273] P. H. Y. Li, R. F. Bishop, and C. E. Campbell, *Phys. Rev. B* **89**, 220408(R) (2014).
- [274] S.-S. Gong, D. N. Sheng, O. I. Motrunich, and M. P. A. Fisher, *Phys. Rev. B* **88**, 165138 (2013).
- [275] Z. Zhu, D. A. Huse, and S. R. White, *Phys. Rev. Lett.* **110**, 127205 (2013).

- [276] Z. Zhu, D. A. Huse, and S. R. White, Phys. Rev. Lett. **111**, 257201 (2013).
- [277] R. Ganesh, J. van den Brink, and S. Nishimoto, Phys. Rev. Lett. **110**, 127203 (2013).
- [278] E. Rastelli, A. Tassi, and L. Reatto, Physica B+C **97**, 1 (1979).
- [279] S. M. Winter, Y. Li, H. O. Jeschke, and R. Valentí, Phys. Rev. B **93**, 214431 (2016).
- [280] A. Bose, M. Routh, S. Voleti, S. K. Saha, M. Kumar, T. Saha-Dasgupta, and A. Paramekanti, Phys. Rev. B **108**, 174422 (2023).
- [281] Y. Watanabe, S. Trebst, and C. Hickey, arXiv:2212.14053 (2022).
- [282] M. E. Zhitomirsky and A. L. Chernyshev, Rev. Mod. Phys. **85**, 219 (2013).
- [283] S. Wenzel, T. Coletta, S. E. Korshunov, and F. Mila, Phys. Rev. Lett. **109**, 187202 (2012).
- [284] T. Coletta, S. E. Korshunov, and F. Mila, Phys. Rev. B **90**, 205109 (2014).
- [285] T. Coletta, M. E. Zhitomirsky, and F. Mila, Phys. Rev. B **87**, 060407(R) (2013).
- [286] H. Takagi, T. Takayama, G. Jackeli, G. Khaliullin, and S. E. Nagler, Nat. Rev. Phys. **1**, 264 (2019).
- [287] G. Jackeli and G. Khaliullin, Phys. Rev. Lett. **102**, 017205 (2009).
- [288] T. Yokoi, S. Ma, Y. Kasahara, S. Kasahara, T. Shibauchi, N. Kurita, H. Tanaka, J. Nasu, Y. Motome, C. Hickey, et al., Science **373**, 568 (2021).
- [289] J. Bruin, R. Claus, Y. Matsumoto, N. Kurita, H. Tanaka, and H. Takagi, Nature Physics **18**, 401 (2022).
- [290] A. Banerjee, J. Yan, J. Knolle, C. A. Bridges, M. B. Stone, M. D. Lumsden, D. G. Mandrus, D. A. Tennant, R. Moessner, and S. E. Nagler, Science **356**, 1055 (2017).
- [291] T. Cookmeyer and J. E. Moore, Phys. Rev. B **98**, 060412 (2018).
- [292] T. Cookmeyer and J. E. Moore, Phys. Rev. B **107**, 224428 (2023).
- [293] M. Möller et al., to appear (2024).
- [294] M. Tinkham, *Group Theory and Quantum Mechanics (Dover Books on Chemistry)* (Dover Publications, 2003).
- [295] H. Bethe, Zeitschrift für Physik **71**, 205 (1931).
- [296] R. P. Feynman, *Statistical Mechanics: A Set Of Lectures* (CRC Press, Boca Raton, 1998), ISBN 9780429493034.
- [297] F. J. Dyson, Phys. Rev. **102**, 1217 (1956).

- [298] V. M. Galitski, B. Karnakov, V. Galitski, and V. I. Kogan, *Exploring Quantum Mechanics: A Collection of 700+ Solved Problems for Students, Lecturers, and Researchers* (OUP Oxford, 2013), ISBN 9780199232727.
- [299] M. E. Zhitomirsky and T. Nikuni, Phys. Rev. B **57**, 5013 (1998).
- [300] T. Holstein and H. Primakoff, Phys. Rev. **58**, 1098 (1940).
- [301] J. Colpa, Phys. A: Stat. Mech. Appl. **93**, 327 (1978).

Appendix A

Supplemental materials for Chapter 2

A.1 Magnetic order in the AFM- $d/\pi p$ phase

There are several types of approaches one could take to try to infer the broken symmetries of the 2D system from our finite-bond dimension DMRG results on finite sized cylinders. For the most part, our results in the main text seem clear-cut, with broken symmetries appearing in fairly large cylinders with small changes as the bond dimension is increased. However, it is clearly very useful to try to consider particular points in the phase diagram for a more careful finite-sized analysis. In this section we consider the antiferromagnetic order in the low-doped $t' > 0$ system. In the recent paper[125], the authors found that in this regime on width 6 cylinders strong d -wave pairing was indicated, but the authors did not clearly conclude that there was AF order.

The DMRG studies in [125] used full SU(2) symmetry, and kept more states than we have been able to. However, in DMRG calculations, correlation functions, which were used in [125], are inherently less accurate than local quantities, which we used. The spin-spin correlations decayed exponentially in[125], but the mere fact of exponential decay does not

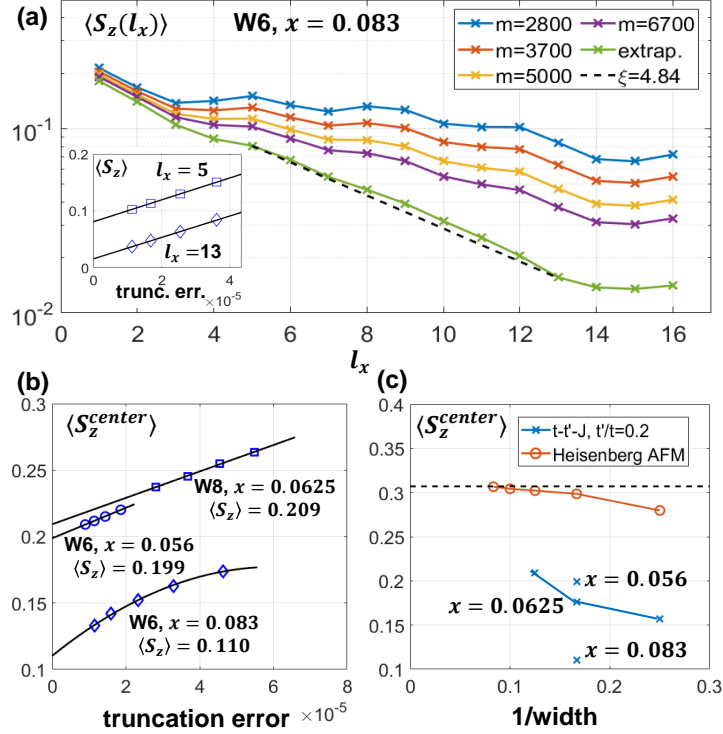


Figure A.1: (a): Decay of local magnetic order as one moves away from the left edge where a weak staggered magnetic field of 0.03 is applied for different bond dimension m . $\langle S_z(l_x) \rangle$ is extrapolated with truncation error (shown in inset) on a point by point basis. The decay of magnetic order shows good agreement with correlation length $\xi = 4.84$ [125]. (b): For a length/width=2 cylinder with strong staggered magnetic pinning field of 0.2 on both edges [3], local magnetic order in the center extrapolated with truncation error. All three cases are in the AFM- $d/\pi p$ phase with $t' = 0.2$. (c): Using the technique described in (b), local magnetic order in the center for cylinders of different widths for $t-t'-J$ model and the Heisenberg model. For the Heisenberg model, the dashed line shows the precisely known order parameter 0.307 from [1].

tell much about possible long-range order in 2D. For example, it is known that an even-leg Heisenberg ladder always has exponential decay of correlations, but in 2D the model has long range order. The crucial question is what is the decay length, and how does it scale with width?

Spin-spin correlation lengths can also be determined through the static response to a pinning field, allowing a local measurement. In Fig. A.1(a), we compare measurements of the spin-spin correlation length of the width 6 system at a doping of $x = 0.083$ and $t' = 0.22$, $J = 1/3$, $J' = 0.016$. The correlation length in [125] for this system was determined to be $\xi =$

4.84. By extrapolating the local response to an edge field, we find a completely consistent exponential decay with the same correlation length. The extrapolations in truncation error for each local measurement are very well behaved, as shown in inset of Fig. A.1(a). Does $\xi = 4.84$ on a width 6 cylinder correspond to long range 2D order? Correlation lengths were shorter on width 4, but this information did not make it clear in [125] that there was long range AF order in 2D.

Instead, we use the aspect ratio method discussed in reference[3]. In this case strong pinning is applied to the ends of the cylinder and the order parameter is measured in the center. The aspect ratio can be chosen to eliminate the leading finite size correction, making the approach to the 2D order parameter very rapid. (In longer cylinders, the system looks more 1D-like, giving a smaller order parameter; in shorter cylinders, the strong pinning prevails, giving an overestimate.) For the Heisenberg square lattice, Fig. A.1(c) shows how effective this approach is for an aspect ratio of 2, which is a little larger than the ideal aspect ratio near 1.9. With the slightly larger aspect ratio, the approach is from below as the width is increased. We apply this approach to the low-doped t - J model at $x = 0.0625$, using 8×4 , 12×6 , and 16×8 cylinders. For width 6, the target doping corresponded to a non-integer number of pairs, so a linear interpolation was made between two adjacent integral dopings. The finite size behavior is not as flat as for the Heisenberg case, and the interpolation is only a rough treatment, but nevertheless the results provide solid evidence for a nonzero AF order parameter, roughly between 0.2 and 0.25.

Appendix B

Supplemental materials for Chapter 3

B.1 The parameters choice for the three-band Hubbard model

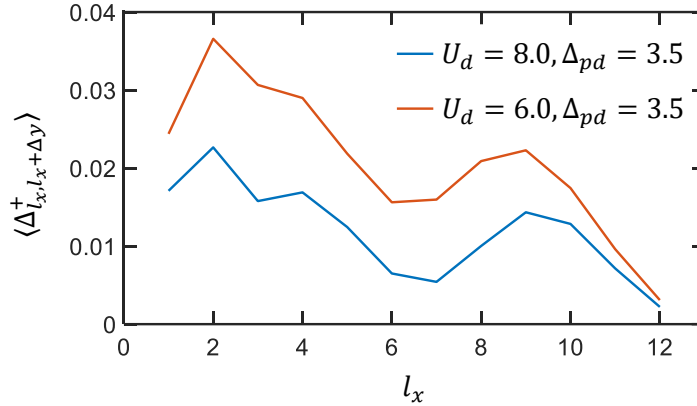


Figure B.1: Pairing response of two different U_{dd} with pairfields applied on two columns ($l_x = 1, 2$) on the left edge of a 12×5 cylinder, at a hole doping of 0.15 ($n = 1.15$). Both the applied pairfields and the pairing responses are on nearest-neighbor vertical Cu-Cu bonds.

A common choice of the parameters for the three-band Hubbard model is: $t_{pd} = 1.0$, $t_{pp} = 0.5$, $\Delta_{pd} = 3.0$, $U_d = 8.0$, $U_p = 3.0$, $V_{pd} = 0.5$ [164]. In a recent density-matrix embedding theory study [135], the appropriate range of U_d is estimated to be 4.5-9.3 when fixing other

parameters as in the common choice. While the common choice $U_d = 8.0$ falls in the upper half of this range, we also consider another $U_d = 6.0$ in the lower half of this range. In addition, we omit V_{pd} but increase Δ_{pd} to 3.5 to incorporate its effect. A comparison of the pairing responses of these two choices of U_d are shown in Fig. B.1, and $U_d = 6.0$ exhibits a stronger pairing response, so we choose it for a clearer signal.

B.2 Calculations of the Wannier single-band model

After constructing of Wannier functions, we derive the downfolded single-band model by projecting the three-band Hamiltonian on the Wannier basis and truncate terms with small magnitude, as described in the main text.

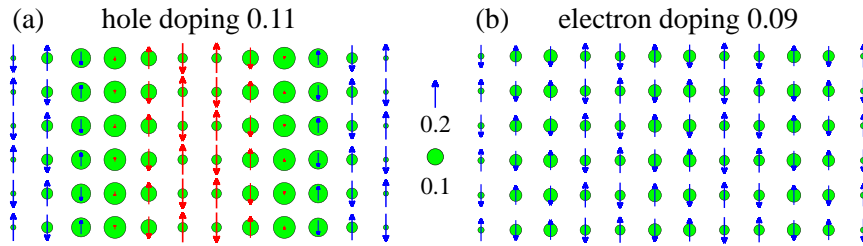


Figure B.2: Simulations of the Wannier model on width-6 cylinders for (a) hole doping of 0.11 and (b) electron doping of 0.09, respectively.

Simulations of the Wannier model (with parameters from the case **h1**) on a width-6 cylinder for both hole and electron doping are presented in Fig. B.2. The occurrence of stripes (hole doping) and commensurate antiferromagnetism (electron doping) is consistent with the three-band model as well as the cuprates.

The validity of the Wannier model is verified by the consistency with the three-band model in the local spin and charge order, the d -wave pairing order, as well as the single-particle correlations, as shown in Fig. B.3. The minor differences in modulations of the hole density and the pairing order along the y direction could be related to different finite size effects or virtual processes involving higher bands, which appear to be unimportant.

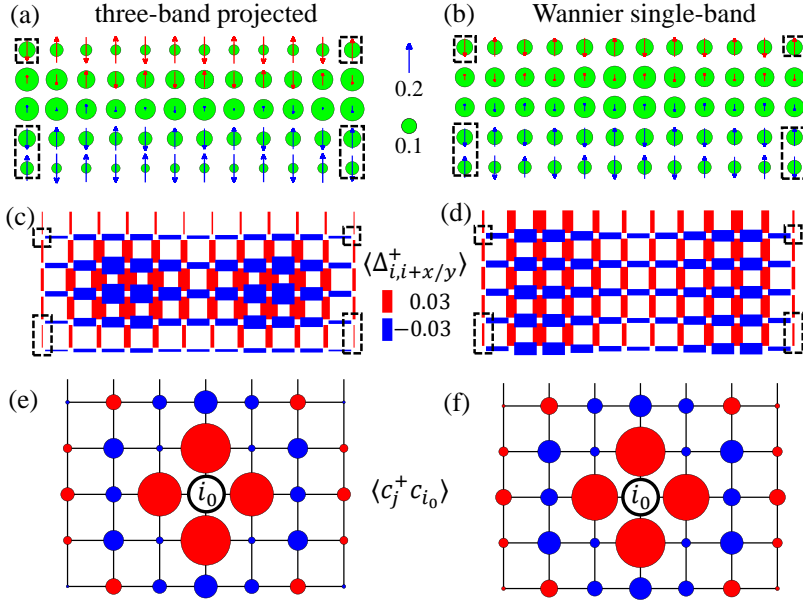


Figure B.3: For the case **h1**, comparisons of physical properties for the three-band wavefunction projected onto the single-band space defined by the Wannier functions (left), and a direct simulation the truncated Wannier model (right). (a) and (b): The local charge and spin structure. The length of the arrows and the diameter of the circles represent $\langle S^z \rangle$ and local doping, respectively. (c) and (d): The d -wave pairing order $\langle \Delta_{ij}^+ + \Delta_{ij} \rangle$ between neighboring sites i and j , with the color and thickness of the bond representing the sign and amplitude of the pairing order. (e) and (f): Single-particle correlation functions with the area and color of the circle on site j indicating the magnitude and sign of $\sum_{\sigma} \langle C_{j\sigma}^\dagger C_{i_0\sigma} \rangle$, with i_0 being the center reference site.

The biggest difference between the Wannier single-band model with the conventional model is the nearest-neighbor additional density-assisted hopping term $t_n c_{j\sigma}^\dagger c_{i\sigma} (n_{i\bar{\sigma}} + n_{j\bar{\sigma}})$ with $t_n \sim 0.6t$, which further enhances pairing comparing to its mean-field $t_n c_{j\sigma}^\dagger c_{i\sigma} \langle n \rangle$. In Fig. B.4, we vary the magnitude of t_n and find that it always produces a bigger superconducting phase stiffness, compared with the mean-field treatment where the t_n term is incorporated into an ordinary effective hopping t_{eff} .

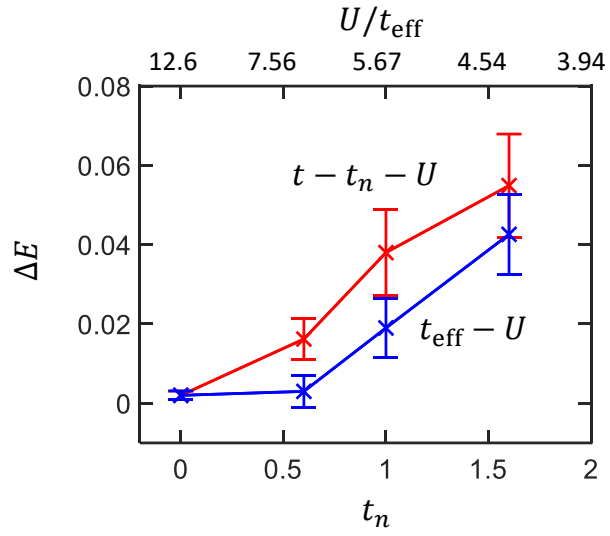


Figure B.4: Superconducting phase stiffness measured by the energy difference for different pairfield boundary conditions (see the main text) as a function of t_n and the corresponding mean-field t_{eff} . $t = 1$ is the energy unit and $U = 12.6$ for both models. System is at a hole doping ~ 0.11 .

Appendix C

Supplemental materials for Chapter 4

C.1 Multipolar order parameters

We are interested in quantum spin orders that break full rotational symmetry without displaying dipolar ordering. These phases are characterized by multipole order parameters such as quadrupole, octupole, etc. Higher quantum spins have larger local Hilbert spaces and naturally exhibit higher-multipole degrees of freedom. In general, spins S allows for on-site order parameters, which transform as rank- k tensor operators, with k taking values of $0, 1, \dots, 2S$.

A rank- k tensor operator $\mathbf{T}^{(k)}$ has $2k + 1$ components that satisfy the commutation relations [294]

$$[S^z, T_q^{(k)}] = qT_q^{(k)} \quad \text{and} \quad [S^\pm, T_q^{(k)}] = \sqrt{k(k+1) - q(q \pm 1)} T_{q \pm 1}^{(k)}, \quad (\text{C.1})$$

which enable a systematic construction of the multipole order parameters $T_q^{(k)}$ with $q \in [-k, k]$ for each k .

For example, the dipole operators correspond to the $k = 1$ multiplet with $T_1^{(1)} = S^+$, $T_0^{(1)} = S^z$, and $T_{-1}^{(1)} = S^-$, while the quadrupole operators form a rank-2 tensor with

$$T_2^{(2)} = S^+S^+, \quad T_1^{(2)} = -S^+S^z - S^zS^+, \quad T_0^{(2)} = \sqrt{\frac{2}{3}}(3S^zS^z - S(S+1)), \quad (\text{C.2})$$

$$T_{-1}^{(2)} = T_1^{(2)\dagger}, \quad \text{and} \quad T_{-2}^{(2)} = T_2^{(2)\dagger}. \quad (\text{C.3})$$

Octupolar operators can be generated from $T_3^{(3)} = S^+S^+S^+$ by the repeated application of $[S^\pm, T_q^{(k)}]$, see Eq. (C.1).

For the $S = \frac{1}{2}$ systems, quadrupole (nematic) orders require a consideration of the two-spin operators in the form of $S_1^\alpha S_2^\beta$ defined on bonds instead of the on-site spin-operators in case of the higher spins. The decomposition of such bond operators consists of the trace, that is the scalar operator $\mathbf{S}_1 \cdot \mathbf{S}_2$, which is SU(2) invariant and commutes with the total spin, the traceless antisymmetric part $\mathbf{S}_1 \times \mathbf{S}_2$, which is a vector (rank-1 tensor), and the traceless symmetric part corresponding to spin-quadrupole operators (rank-2 tensor) $Q_{12}^{\alpha\beta} = S_1^\alpha S_2^\beta + S_1^\beta S_2^\alpha - \delta_{\alpha\beta} \frac{2}{3} (\mathbf{S}_1 \cdot \mathbf{S}_2)$.

The quadrupole bond operators can be expressed in the time-reversal invariant basis

$$|s\rangle = \frac{1}{\sqrt{2}}(|\uparrow\downarrow\rangle - |\downarrow\uparrow\rangle), \quad |t_x\rangle = \frac{i}{\sqrt{2}}(|\uparrow\uparrow\rangle - |\downarrow\downarrow\rangle), \quad (\text{C.4})$$

$$|t_y\rangle = \frac{1}{\sqrt{2}}(|\uparrow\uparrow\rangle + |\downarrow\downarrow\rangle), \quad |t_z\rangle = \frac{-i}{\sqrt{2}}(|\uparrow\downarrow\rangle + |\downarrow\uparrow\rangle), \quad (\text{C.5})$$

as $Q_{12}^{\alpha\beta} = -\frac{1}{2}(|t_\alpha\rangle\langle t_\beta| + |t_\beta\rangle\langle t_\alpha|) + \frac{1}{3}\delta_{\alpha\beta} \sum_\gamma |t_\gamma\rangle\langle t_\gamma|$. A bond nematic state can be written as a linear combination of the triplet states $|\mathbf{t}\rangle = \sum_\alpha \bar{t}_\alpha |t_\alpha\rangle$ with real coefficients \bar{t}_α . Such a state

is time-reversal symmetric, and has no dipole order, $\langle \mathbf{t} | S_i^\alpha | \mathbf{t} \rangle \equiv 0$, as only the quadrupole matrix elements are finite.

While the expectation values of dipolar operators are zero in a purely quadrupolar state, the reverse is not true; quadrupolar order parameters can be finite in a magnetic state. For example, the magnetic state $|\uparrow\uparrow\rangle = \frac{1}{\sqrt{2}}(|t_y\rangle - i|t_x\rangle)$ gives $\langle S_{\text{tot}}^z \rangle = 1$ and at the same time $\langle Q^{zz} \rangle = \frac{1}{3}$.

Bond-nematic phases in spin-half frustrated magnets can arise from a condensation of bound magnon pairs in the field-polarized paramagnet. The two-magnon state is directly related to the quadrupole operator $T_{-2}^{(2)} = -S_i^- S_j^-$

$$\sum_{i,j} \psi_{ij} T_{-2}^{(2)} | \uparrow\uparrow \dots \uparrow \rangle = \sum_{i,j} \psi_{ij} (Q_{ij}^{x^2-y^2} - iQ_{ij}^{xy}) | \uparrow\uparrow \dots \uparrow \rangle, \quad (\text{C.6})$$

with the bound state in the $Q_{ij}^{x^2-y^2}$ and Q_{ij}^{xy} channels. The orbital (lattice) symmetry of the bound state is encoded in the ψ_{ij} coefficients that are determined from the solution of the two-magnon Schrodinger equation (SE) considered in the next Section. While the nomenclature of the $Q_{ij}^{\alpha\beta}$ operators is reminiscent of that of the $L = 2$ orbital states, it is unrelated to the d -wave nature of the bound states discussed below.

The ordering of the dipole and quadrupole moments can be expressed via the spin and quadrupole structure factors, $\mathcal{S}^{\alpha\beta}(\mathbf{k}) = \langle S_{\mathbf{k}}^\alpha S_{-\mathbf{k}}^\beta \rangle$ and $\mathcal{Q}^{\alpha\beta}(\mathbf{k}) = \langle Q_{\mathbf{k}}^{\alpha\beta} Q_{-\mathbf{k}}^{\alpha\beta} \rangle$, respectively. One expects finite Bragg peaks in both $\mathcal{S}(\mathbf{k})$ and $\mathcal{Q}(\mathbf{k})$ in the conventional magnetic phase, whereas in the nematic state Bragg peaks are present only in $\mathcal{Q}(\mathbf{k})$.

A general quadrupole-quadrupole correlation function has the form $\langle Q_{i,j}^{\alpha\beta} Q_{i+r,j+r'}^{\alpha\beta} \rangle$, which can be measured numerically in finite clusters. However, for the symmetry-broken states, the expectation value of the nematic order parameter $\langle Q_{ij}^{\alpha\beta} \rangle$ can be also detected directly,

similarly to the ordered moment $\langle S_i^z \rangle$ in the dipolar magnetic states. This is used in our DMRG approach, see Secs. C.4 below and the main text.

C.2 Magnon bound states

C.2.1 Magnon interaction

We restrict ourselves to the bound-state problem in a fully polarized FM phase of an isotropic spin- S Heisenberg model on a Bravais lattice in a field

$$\mathcal{H} = \frac{1}{2} \sum_{i,\delta} J_\delta \mathbf{S}_i \cdot \mathbf{S}_j - H \sum_i S_i^z, \quad (\text{C.7})$$

where $\boldsymbol{\delta} = \mathbf{r}_j - \mathbf{r}_i$ spans all non-zero n th-neighbor couplings that are present in the model.

The kinetic energy of a magnon, or a single-spin-flip eigenstate $|\psi_{1,\mathbf{q}}\rangle = 1/\sqrt{N} \sum_i e^{-i\mathbf{q}\mathbf{r}_i} S_i^- |0\rangle$, relative to the ground-state energy E_0 of $|0\rangle = |\uparrow\uparrow\uparrow \dots\rangle$, can be written as [212]

$$\varepsilon_{\mathbf{q}} = H + S(\mathcal{J}_{\mathbf{q}} - \mathcal{J}_0), \quad \text{with} \quad \mathcal{J}_{\mathbf{q}} = \sum_{\delta} J_\delta e^{i\mathbf{q}\boldsymbol{\delta}}, \quad (\text{C.8})$$

where $\mathcal{J}_{\mathbf{q}} = \mathcal{J}_{-\mathbf{q}}$ as $J_\delta = J_{-\delta}$ on a Bravais lattice. Assuming that $\varepsilon_{\mathbf{q}}$ has an absolute minimum at the momentum \mathbf{Q} and given the simple Zeeman-like dependence of energy on the field, one can find the critical field for a transition to a single-spin-flip BEC from the condition $\varepsilon_{\mathbf{Q}} = 0$, which yields

$$H_{s1} = S(\mathcal{J}_0 - \mathcal{J}_{\mathbf{Q}}). \quad (\text{C.9})$$

In the absence of an attraction between magnons, the expression (C.9) is valid for any value of S . Thus, one refers to H_{s1} and to the single-magnon BEC transitions itself as the “classical” ones in this case.

Magnon interaction requires a consideration of the two-spin-flip wavefunction, whose generic form is given by

$$|\psi_2\rangle = \frac{1}{2} \sum_{i,j} \psi_{i,j} S_i^- S_j^- |0\rangle. \quad (\text{C.10})$$

The reason why this function cannot be built directly from the basis of single-spin-flip *operators*, which are complete and orthogonal in the single-particle sector, is the non-commutativity of spin operators, the problem recognized early on [295–297]. The commonly followed resolution [200, 201] is to operate directly in the basis of the $|\psi_2\rangle$ wavefunctions (C.10), which is complete, but not orthogonal. Despite this latter inconvenience, the *exact* two-particle Schroedinger equation (SE) can be obtained by standard, if tedious, manipulations [212] to yield

$$(E - \varepsilon_{\frac{\mathbf{K}}{2}+\mathbf{q}} - \varepsilon_{\frac{\mathbf{K}}{2}-\mathbf{q}})\psi_{\mathbf{K}}(\mathbf{q}) = \frac{1}{2N} \sum_{\mathbf{p}} V_{\mathbf{K}}(\mathbf{q}, \mathbf{p})\psi_{\mathbf{K}}(\mathbf{p}), \quad (\text{C.11})$$

$$\text{with } \psi_{\mathbf{K}}(\mathbf{q}) = \frac{1}{N} \sum_{i,j} e^{-i\frac{\mathbf{K}}{2}(\mathbf{r}_i+\mathbf{r}_j)} e^{-i\mathbf{q}(\mathbf{r}_j-\mathbf{r}_i)} \psi_{i,j}, \quad (\text{C.12})$$

and the magnon interaction potential given by

$$V_{\mathbf{K}}(\mathbf{q}, \mathbf{p}) = \mathcal{J}_{\mathbf{q}-\mathbf{p}} + \mathcal{J}_{\mathbf{q}+\mathbf{p}} - \mathcal{J}_{\frac{\mathbf{K}}{2}-\mathbf{q}} - \mathcal{J}_{\frac{\mathbf{K}}{2}+\mathbf{q}}. \quad (\text{C.13})$$

The first two terms in $V_{\mathbf{K}}(\mathbf{q}, \mathbf{p})$ in (C.13) adhere to the conventional “potential-like” form, as they depend on the momentum transfer between initial and final particles in the scattering, with the momenta $\mathbf{K}/2 \pm \mathbf{q}$ and $\mathbf{K}/2 \pm \mathbf{p}$, respectively. The last two terms depend on the individual particle momenta and originate from the “hard-core” repulsion of spin flips.

Given the single-magnon energy in (C.8) and magnon interaction potential in (C.13), it is made explicit by SE (C.12) that the magnon interaction is manifestly a $1/S$ effect, with the role of pairing diminishing in the large- S limit and single-magnon BEC retaining its classical value.

We also would like to remark that an expression *identical* to (C.13) is trivially obtained in the $O(S^0)$ order of expansion of (C.7) within the perfectly commutative and orthogonal *bosonic* basis of the standard $1/S$ -approximation, obviously leading to a form of the two-magnon SE that is identical to (C.12).

C.2.2 Simple case, Cooper problem analogy, and higher harmonics

It is instructive to have a general intuition on solving SE in (C.12) for a simple case. Consider a continuum limit for particles of mass m and energies $\varepsilon_{\mathbf{k}} = \mathbf{k}^2/2m$ that are attracted via a δ -functional potential in real space, $V(\mathbf{r}_1, \mathbf{r}_2) = -\alpha\delta(\mathbf{r}_1 - \mathbf{r}_2)$, which corresponds to a constant in the momentum space, $V_{\mathbf{K}}(\mathbf{q}, \mathbf{p}) = -\alpha$. This reduces (C.12) to an algebraic equation for ψ that is trivially solved as

$$\psi_{\mathbf{K}}(\mathbf{q}) = -\frac{\alpha}{2} \cdot \frac{C_{\mathbf{K}}}{E - E_{\mathbf{K}} - \mathbf{q}^2/m}, \quad \text{with} \quad C_{\mathbf{K}} = \frac{1}{N} \sum_{\mathbf{p}} \psi_{\mathbf{K}}(\mathbf{p}), \quad (\text{C.14})$$

where $E_{\mathbf{K}} = \mathbf{K}^2/4m$ is the bottom of the two-particle continuum for the total momentum \mathbf{K} . The second equation in (C.14) provides a self-consistency condition, which is also an implicit equation on the pair's energy E

$$1 = -\frac{\alpha}{2N} \sum_{\mathbf{p}} \frac{1}{E - E_{\mathbf{K}} - \mathbf{p}^2/m}. \quad (\text{C.15})$$

Finding $E < E_{\mathbf{K}}$ from (C.15) constitutes a solution of the bound-state problem. This consideration is analogous to a textbook problem of the bound state for a single particle in a free space with a δ -functional potential well [298], also demonstrating a mapping of the two- to one-body problem. A direct integration in Eq. (C.15) in the D -dimensional continuum demonstrates the existence of a bound state for an *arbitrarily weak* attraction in the dimensions $D = 1$ and $D = 2$, and requires α to exceed a threshold value of order $1/m$ in $D = 3$ [298]. Since we are interested in the case of $D = 2$, the solution for it is

$$E - E_{\mathbf{K}} = \frac{\Lambda}{m} \cdot e^{-\frac{8\pi}{\alpha m}}, \quad (\text{C.16})$$

where Λ is a large-momentum cut-off and the non-analytic dependence on the coupling constant α is clear. These results rely exclusively on the density of states of the non-relativistic particles in D -dimensions and are expected to hold for *any* short-range attractive potential in the continuum [298]. One of the well-known realizations of such conditions is the celebrated Cooper problem of the short-range attraction of electrons near the Fermi surface [219]. The presence of the finite Fermi-momentum cutoff leads to an effective *dimensional reduction* from 3D to 2D, resulting in the 2D-like density of states and the pairing gap that closely follows Eq. (C.16).

For a realization of the pair-BEC, the lowest bound-state energy needs to be below the *absolute minimum* of the two-particle continuum, which typically occurs at a high-symmetry \mathbf{K} -point. In an example above, this is the $\mathbf{K} = 0$ point. There, a systematic symmetry consideration of the pairing in the higher partial-wave channels is also possible. Given the mapping onto the one-body problem in the continuum, it can be made explicit that with an exception of the s -wave channel, which is exposed above, all other channels have nodes of their corresponding pairing potential that pass through the minimum of the single-particle energy. This crucial feature leads to an effective *dimensional increase*, as opposed to the dimensional reduction, suggesting that the weak attraction in the continuum in 2D can only

create s -wave bound states, but not the ones in the higher-harmonics, which would require the corresponding coupling strengths to exceed threshold values of order $1/m$.

C.2.3 Pairing in the J_1 - J_2 Heisenberg model

We now turn to the problem of pairing in the ferro-antiferromagnetic $S = 1/2$ J_1 - J_2 Heisenberg model on the square lattice with the ferromagnetic $J_1 = -1$ taken as a unit of energy and antiferromagnetic $J_2 > 0$. The convenient shorthand notation $\mathcal{J}_{\mathbf{q}}$ in (C.8) can be rewritten using standard hopping amplitudes

$$\mathcal{J}_{\mathbf{q}} = -4\gamma_{\mathbf{q}} + 4J_2\gamma_{\mathbf{q}}^{(2)}, \quad \text{with} \quad \gamma_{\mathbf{q}} = \frac{1}{2}(\cos q_x + \cos q_y), \quad \text{and} \quad \gamma_{\mathbf{q}}^{(2)} = \cos q_x \cos q_y. \quad (\text{C.17})$$

The single-magnon energy (C.8) for $S = 1/2$ is given by

$$\varepsilon_{\mathbf{q}} = H + 2(1 - \gamma_{\mathbf{q}}) - 2J_2(1 - \gamma_{\mathbf{q}}^{(2)}) = \varepsilon_{\mathbf{Q}} - 2\gamma_{\mathbf{q}} + 2J_2(1 + \gamma_{\mathbf{q}}^{(2)}), \quad (\text{C.18})$$

where we use that for $J_2 > 0.5$, the minima of $\varepsilon_{\mathbf{q}}$ are at the non-trivial $\mathbf{Q} = (0, \pi)[(\pi, 0)]$ points, with $\varepsilon_{\mathbf{Q}} = H + 2 - 4J_2$, leading to $H_{s1} = -2 + 4J_2$, see (C.9). This is the range of J_2 that we will consider below, although extension to the case of $J_2 < 0.5$, for which the minimum of $\varepsilon_{\mathbf{q}}$ is at $\mathbf{Q}=0$, is easily made.

In addition to the hopping amplitude $\gamma_{\mathbf{q}}$ in (C.17), one can see an immediate utility in introducing other combinations of lattice harmonics of different symmetry

$$\gamma_{\mathbf{q}}^- = \frac{1}{2}(\cos q_x - \cos q_y), \quad \gamma_{\mathbf{q}}^{sxy} = [\gamma_{\mathbf{q}}^{(2)}] \cos q_x \cos q_y, \quad \text{and} \quad \gamma_{\mathbf{q}}^{dxy} = \sin q_x \sin q_y, \quad (\text{C.19})$$

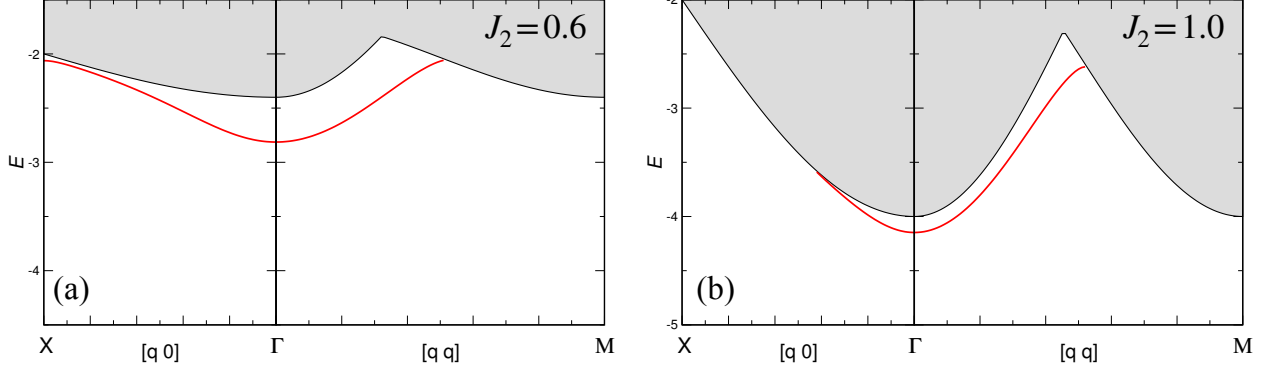


Figure C.1: The two-magnon continuum (shaded area) and the bound state energies (lines) along the representative $\mathbf{K} = [q_x, q_y]$ cuts in the Brillouin zone for (a) $J_2 = 0.6$ and (b) $J_2 = 1.0$. $M = [\pi, \pi]$ and $X = [\pi, 0]$.

as they permit an easy symmetrization of the single-magnon energies in SE (C.12) and a separation of interaction potential (C.13) into the partial harmonics using

$$\gamma_{\mathbf{q}-\mathbf{p}} + \gamma_{\mathbf{q}+\mathbf{p}} = 2\gamma_{\mathbf{p}}\gamma_{\mathbf{q}} + 2\gamma_{\mathbf{p}}^-\gamma_{\mathbf{q}}^-, \quad \gamma_{\mathbf{q}-\mathbf{p}}^{(2)} + \gamma_{\mathbf{q}+\mathbf{p}}^{(2)} = 2\gamma_{\mathbf{p}}^{sxy}\gamma_{\mathbf{q}}^{sxy} + 2\gamma_{\mathbf{p}}^{dxy}\gamma_{\mathbf{q}}^{dxy}. \quad (\text{C.20})$$

Introducing binding energy of the pair $2\Delta > 0$ relative to the absolute minimum of the two-magnon continuum via $E = -2\Delta + 2\varepsilon_{\mathbf{Q}}$, converts the energy difference in the left-hand side of SE in (C.12) to

$$E - \varepsilon_{\frac{\mathbf{K}}{2}+\mathbf{q}} - \varepsilon_{\frac{\mathbf{K}}{2}-\mathbf{q}} = -2\Delta + 4(\gamma_{\frac{\mathbf{K}}{2}}\gamma_{\mathbf{q}} + \gamma_{\frac{\mathbf{K}}{2}}^-\gamma_{\mathbf{q}}^-) - 4J_2(1 + \gamma_{\frac{\mathbf{K}}{2}}^{sxy}\gamma_{\mathbf{q}}^{sxy} + \gamma_{\frac{\mathbf{K}}{2}}^{dxy}\gamma_{\mathbf{q}}^{dxy}), \quad (\text{C.21})$$

while the interaction potential (C.13) becomes

$$V_{\mathbf{K}}(\mathbf{q}, \mathbf{p}) = -8\gamma_{\mathbf{q}}(\gamma_{\mathbf{p}} - \gamma_{\frac{\mathbf{K}}{2}}) - 8\gamma_{\mathbf{q}}^-(\gamma_{\mathbf{p}}^- - \gamma_{\frac{\mathbf{K}}{2}}^-) + 8J_2\gamma_{\mathbf{q}}^{sxy}(\gamma_{\mathbf{p}}^{sxy} - \gamma_{\frac{\mathbf{K}}{2}}^{sxy}) + 8J_2\gamma_{\mathbf{q}}^{dxy}(\gamma_{\mathbf{p}}^{dxy} - \gamma_{\frac{\mathbf{K}}{2}}^{dxy}), \quad (\text{C.22})$$

with the terms clearly assuming the separable partial-wave decomposition structure, although with asymmetric “shifts” of the harmonics by $\gamma_{\frac{\mathbf{K}}{2}}$ due to the hard-core components of the original potential (C.13).

For the magnon-band minima at $\mathbf{Q} = (0, \pi)[(\pi, 0)]$ points, there only two distinct total momenta of their pair at which pair-BEC can occur, $\mathbf{K} = 0$ and $\mathbf{K} = (\pi, \pi)$. While rigorous arguments can be given to prove that the $\mathbf{K} = (\pi, \pi)$ sector does not support pairing in any orbital channel in the range of $J_2 > 1/\pi$, we skip them in favor of the visual demonstration of the numerical solution for the bound state problem (C.12) with the energy denominator (C.21) and pairing potential (C.22) for \mathbf{K} along a representative cut of the Brillouin zone and for two representative $J_2 = 0.6$ and $J_2 = 1.0$, see Fig. C.1. This Figure clearly points to the importance of the $\mathbf{K} = 0$ sector in our case, considered next.

$\mathbf{K} = 0$ sector

For the $\mathbf{K} = 0$ sector, $\gamma_{\frac{\mathbf{K}}{2}} = \gamma_{\frac{\mathbf{K}}{2}}^{s_{xy}} = 1$ and $\gamma_{\frac{\mathbf{K}}{2}}^- = \gamma_{\frac{\mathbf{K}}{2}}^{d_{xy}} = 0$, converting the energy part of SE (C.21) to

$$\Delta E_0(\mathbf{q}) = (E - \varepsilon_{\frac{\mathbf{K}}{2} + \mathbf{q}} - \varepsilon_{\frac{\mathbf{K}}{2} - \mathbf{q}})|_{\mathbf{K}=0} = -2\Delta - 4J_2(1 + \gamma_{\mathbf{q}}^{(2)}) + 4\gamma_{\mathbf{q}} = -2\Delta - 2(\varepsilon_{\mathbf{q}} - \varepsilon_{\mathbf{Q}}) < 0, \quad (\text{C.23})$$

where the binding energy Δ is relative to the $2\varepsilon_{\mathbf{Q}}$ minimum, and the interaction potential (C.22) becomes,

$$V_0(\mathbf{q}, \mathbf{p}) = -8\gamma_{\mathbf{q}}(\gamma_{\mathbf{p}} - 1) - 8\gamma_{\mathbf{q}}^- \gamma_{\mathbf{p}}^- + 8J_2\gamma_{\mathbf{q}}^{s_{xy}}(\gamma_{\mathbf{p}}^{s_{xy}} - 1) + 8J_2\gamma_{\mathbf{q}}^{d_{xy}}\gamma_{\mathbf{p}}^{d_{xy}} = \sum_{\gamma} V_{\gamma} R_{\gamma}(\mathbf{q}) \tilde{R}_{\gamma}(\mathbf{p}), \quad (\text{C.24})$$

with $\gamma = \{s, d, s_{xy}, d_{xy}\}$, $V_{\gamma} = \{8, 8, -8J_2, -8J_2\}$, $R_{\gamma}(\mathbf{q}) = \{\gamma_{\mathbf{q}}, \gamma_{\mathbf{q}}^-, \gamma_{\mathbf{q}}^{s_{xy}}, \gamma_{\mathbf{q}}^{d_{xy}}\}$, and $\tilde{R}_{\gamma}(\mathbf{p}) = \{\gamma_{\mathbf{p}} - 1, \gamma_{\mathbf{p}}^-, \gamma_{\mathbf{p}}^{s_{xy}} - 1, \gamma_{\mathbf{p}}^{d_{xy}}\}$.

While it is tempting to conclude that this form of interaction already guarantees decomposition of the SE in (C.12) into a fully orthogonal set of algebraic equations on pairing in

separate channels, the analysis provided so far is based entirely on the lattice-harmonic expansion of the interaction potential and magnon energies. Continuing without any symmetry analysis for a moment, the SE (C.12) for the $\mathbf{K}=0$ sector can be rewritten as

$$\psi_0(\mathbf{q}) = -\frac{1}{2} \sum_{\gamma} V_{\gamma} R_{\gamma}(\mathbf{q}) \cdot \frac{C_{\gamma}}{\Delta E_0(\mathbf{q})}, \quad \text{with} \quad C_{\gamma} = \frac{1}{N} \sum_{\mathbf{p}} \tilde{R}_{\gamma}(\mathbf{p}) \psi_0(\mathbf{p}). \quad (\text{C.25})$$

Although it is clear that the SE is, indeed, reduced to a set of algebraic equations for $\psi_0(\mathbf{q})$, these equations are, or can be, coupled, as the constants C_{γ} in (C.25) can have contributions from the $\gamma' \neq \gamma$ components of $\psi_0(\mathbf{q})$.

The partial waves in (C.24) and (C.25) are of the s , s_{xy} , $d_{x^2-y^2}$, and d_{xy} character, with the mirror-plane symmetries at the $\mathbf{K} = 0$ point separating $d_{x^2-y^2}$ and d_{xy} partial-wave solutions of the SE, while the two generalized s -wave-like solutions are allowed to mix. Thus, Eq. (C.25) for the $\mathbf{K} = 0$ sector decouples into two independent algebraic equations for the d -waves and two coupled equations for the s -waves.

The resultant equations on the pairing energy for the $d_{x^2-y^2}$ (d for brevity) and d_{xy} waves are given by

$$d: \quad 1 = -\frac{4}{N} \sum_{\mathbf{p}} \frac{(\gamma_{\mathbf{p}}^-)^2}{\Delta E_0(\mathbf{p})}, \quad \text{and} \quad d_{xy}: \quad 1 = \frac{4J_2}{N} \sum_{\mathbf{p}} \frac{(\gamma_{\mathbf{p}}^{d_{xy}})^2}{\Delta E_0(\mathbf{p})}, \quad (\text{C.26})$$

of which the d_{xy} -wave does not permit any solutions having negatively-defined right-hand side. The d -wave equation yields a solution of our ultimate interest that is discussed in more detail below.

The coupled s -wave equations can be written as

$$C_s = C_s I_{11} + C_{s_{xy}} I_{12}, \quad \text{and} \quad C_{s_{xy}} = C_{s_{xy}} I_{22} + C_s I_{21}, \quad \text{with} \quad I_{11} = -\frac{4}{N} \sum_{\mathbf{p}} \frac{\gamma_{\mathbf{p}}(\gamma_{\mathbf{p}} - 1)}{\Delta E_0(\mathbf{p})},$$

(C.27)

$$I_{22} = \frac{4J_2}{N} \sum_{\mathbf{p}} \frac{\gamma_{\mathbf{p}}^{s_{xy}}(\gamma_{\mathbf{p}}^{s_{xy}} - 1)}{\Delta E_0(\mathbf{p})}, \quad I_{12} = \frac{4J_2}{N} \sum_{\mathbf{p}} \frac{\gamma_{\mathbf{p}}^{s_{xy}}(\gamma_{\mathbf{p}} - 1)}{\Delta E_0(\mathbf{p})}, \quad I_{21} = -\frac{4}{N} \sum_{\mathbf{p}} \frac{\gamma_{\mathbf{p}}(\gamma_{\mathbf{p}}^{s_{xy}} - 1)}{\Delta E_0(\mathbf{p})}.$$

(C.28)

While, ultimately, one can simply use these expressions to numerically prove that they are unable to yield a viable solution for the binding energy, having an intuition on “why” would be very useful. For that, let us consider only the diagonal $I_{\gamma\gamma}$ terms, because if they are unable to sustain a solution on their own, the situation is unlikely to improve by the coupling between the two channels.

For the I_{22} in the s_{xy} -wave channel, the situation is similar to the d_{xy} -wave above in that the coupling is due to a repulsive J_2 term, but it contains a “hard-core shift” in the pairing potential, which makes the outcome less certain analytically. However, with a minimal effort, one is able to prove that I_{22} does indeed remain negative and yields no feasible solutions for the binding energy,

The interaction in the s -wave channel in I_{11} is attractive ($J_1 = -1 < 0$), but it has a hard-core shift in the pairing potential, which is repulsive and is often quoted as the reason for the suppression of the s -wave pairing. While this is a valid mechanism for the lack of pairing in the pure ferromagnetic cases, which never result in the bound states that occur below the absolute minimum of the continuum, this is not the reason why the s -wave is projected out of a pairing in our case. A counterexample is always useful. If we ignore the momentum-dependence in $\Delta E_0(\mathbf{q})$ in the denominator of the integral in I_{11} in (C.27) for a moment (flat magnon bands), it will yield a solution for the bound-state energy that is actually *degenerate*

with the one for the d -wave in (C.26). Yet, for the true $\Delta E_0(\mathbf{q})$ from (C.23), the s -wave solution is absent. Hence, the lack of the binding is elsewhere.

The resolution is that the extended s -wave pairing harmonic $\gamma_{\mathbf{p}} \propto (\cos q_x + \cos q_y)$ in (C.27) has nodes of zeros passing through the energy minima of the denominator $\Delta E_0(\mathbf{p})$, which are at the magnon energy minima $\mathbf{Q} = (0, \pi)[(\pi, 0)]$, leading to a suppressed attraction via the “dimensional increase” mechanism and giving no bound-state solution. For the smaller values of $J_2 < 0.5$, the magnon band minima migrate back to the ferromagnetic minima at $\mathbf{Q} = 0$, where the “hard-core” reasoning takes over in forbidding the $\mathbf{K} = 0$ bound state in the s -wave channel.

Altogether, the d -wave $\mathbf{K} = 0$ magnon bound-state in (C.26) is the only candidate to have a BEC in the ferro-antiferromagnetic J_1 - J_2 Heisenberg model on the square lattice. We consider it in some more details next.

d -wave solution and asymptotics

We rewrite the equation on the d -wave pairing energy (C.26) in two different ways

$$1 = \frac{1}{2N} \sum_{\mathbf{p}} \frac{(\cos p_x - \cos p_y)^2}{\Delta + 2J_2(1 + \cos p_x \cos p_y) - (\cos p_x + \cos p_y)}, \quad (\text{C.29})$$

$$\text{and } 1 = -\frac{V_d}{2N} \sum_{\mathbf{p}} \frac{(\gamma_{\mathbf{p}}^-)^2}{-2\Delta - 2(\varepsilon_{\mathbf{p}} - \varepsilon_{\mathbf{Q}})}, \quad (\text{C.30})$$

with the first one being handy to use in the numerical integration that results in the curves for Δ vs J_2 in Fig. 2(a) and $h_{c2} = h_{c1} + \Delta$ in Fig. 1(a) of the main text. The second one, with $V_d = 8$ in units of $|J_1|$ as before, is useful to relate back to the very beginning of our bound-state consideration, the s -wave pairing in the continuum. Taking the $J_2 \gg 1$ limit for the denominator in (C.30) and expanding near the magnon energy minima $\mathbf{Q} = (0, \pi)[(\pi, 0)]$ yields $\Delta E_0(\mathbf{p}) = -2\Delta - \mathbf{p}^2/m_{\mathbf{Q}}$ with $1/m_{\mathbf{Q}} = 2J_2$.

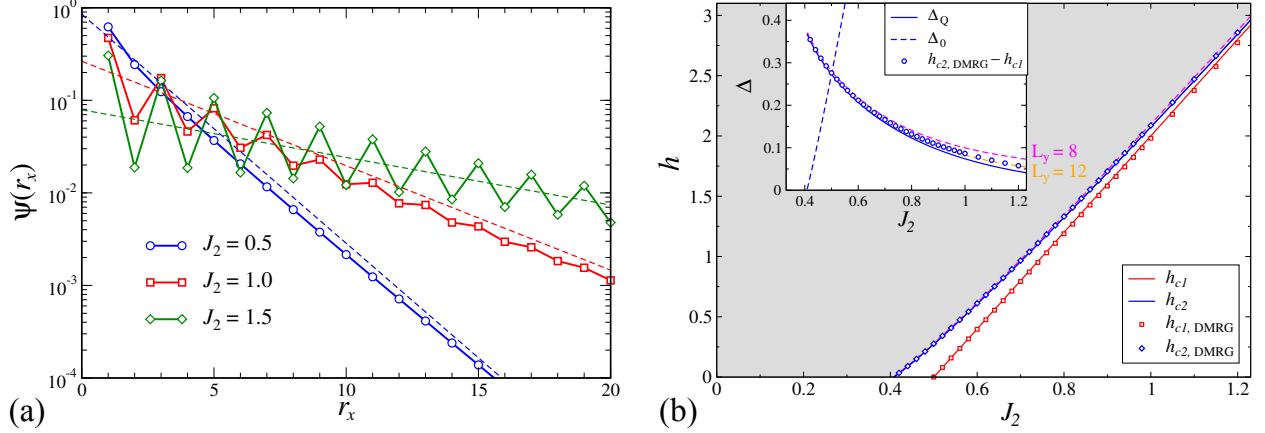


Figure C.2: (a) Numerical results for the d -wave bound-state wave-function $\psi_d(\mathbf{r}_x)$ on a semi-log plot for three representative values of J_2 together with the asymptotic result $\psi_d(\mathbf{r}) = Ae^{-|\mathbf{r}|/\xi}$, with the correlation length $\xi = 0.8e^{\pi J_2/2}$ for all three sets. (b) Same as in Fig. 1(a) and Fig. 2(a) of the main text, with the analytical results for Δ in (C.30) obtained using integration on an $L_x \times L_y$ lattice, with effective $L_x = \infty$ and two values of the width, $L_y = 8$ and $L_y = 12$.

Since the zero-nodes of the pairing harmonic $\gamma_{\mathbf{p}}^-$ are along the $q_x = \pm q_y$ diagonals, perfectly missing the magnon band minima, the coupling of the low-energy magnons is *finite* at \mathbf{Q} , allowing us to approximate $(\gamma_{\mathbf{p}}^-)^2 \approx 1$ near \mathbf{Q} and giving us all the ingredients of the “ s -wave-like” pairing. Thus, in the weak-coupling limit, integration in (C.30) yields the answer that mirrors that of Eq. (C.16)

$$2\Delta \approx \frac{\Lambda}{m_{\mathbf{Q}}} \cdot e^{-\frac{4\pi}{m_{\mathbf{Q}}V_d}} = 2J_2\Lambda \cdot e^{-\pi J_2}, \quad (\text{C.31})$$

with Λ being the large-momentum cutoff and an extra factor $1/2$ in the exponent originating from the two inequivalent minima of the magnon band at $\mathbf{Q} = (0, \pi)$ and $(\pi, 0)$. Thus, the pairing in the d -wave channel in the considered problem indeed maps onto the textbook s -wave solution. One of the key consequence of that is the absence of the upper limit on J_2 for such a pairing to occur.

The other consequence is the exponential decay of the pair wave-function with the distance, $\psi_d(\mathbf{r}) \sim e^{-|\mathbf{r}|/\xi}$, with the correlation length that can be inferred from the virial theorem,

$\mathbf{q}_\xi^2/2m_{\mathbf{Q}} \simeq \Delta$, as $\xi \sim e^{\pi J_2/2}$. In Figure C.2(a), we show the real-space amplitudes of the bound-state wave-function $\psi_d(\mathbf{r})$ from (C.25) along the line $\mathbf{r} = (r_x, 0)$ for several representative values of J_2 together with the asymptotic exponential behavior with $\xi = 0.8e^{\pi J_2/2}$. Lastly, for $J_2 < 0.5$, the magnon band minimum shifts to $\mathbf{Q} = 0$, quickly terminating pairing at $J_2^c = 0.4077593304754(1)$, as can be inferred numerically from (C.30). This is the end-point of the h_{c2} line in Fig. 1(a) in zero field and $\Delta_0 = 0$ point in Fig. 2(a) of the main text, see also Fig. C.2(b) and its inset.

One can emulate the finite-size effects of the DMRG results for the pairing energy Δ that can be seen in Fig. 1(a) and Fig. 2(a) of the main text, by taking the analytical integral for Δ in (C.30) on an $L_x \times L_y$ lattice. The results of such an effort, with two values of L_y and effectively infinite L_x are shown in Fig. C.2. The results are nearly matched by the width $L_y = 12$, not $L_y = 8$, which can be interpreted in favor of the open-periodic boundary conditions employed by DMRG as giving a better approximation of the thermodynamic limit than its nominal width would suggest [3].

C.3 Finite-size scaling of the nematic order parameter

To investigate the order-parameter evolution with the system size, we follow the strategy of Ref. [3]. It suggests that the DMRG cylinders with the open-periodic boundary conditions and the aspect ratio L_x/L_y about 2.0 should cancel the leading finite-size effects for the order parameter in the center of the cluster, closely approximating its value in the thermodynamic 2D limit.

We use three cylinders with the aspect ratio of 2.0 and apply the nematic pair-field of $0.1\langle S_i^- S_{i+y}^- \rangle$ on both edges. The results for the nematic order-parameter $\langle S_i^- S_{i+y}^- \rangle$ and for the z -axis magnetization $\langle S_i^z \rangle$ are shown in Fig. C.3(a) as the profiles along the width of the

clusters. The $1/L_y$ -scaling of the nematic order parameter and magnetization in the center of the cylinders are presented in Fig. C.3(b). Both quantities show little change, giving a strong support to the existence of the nematic phase in 2D and providing a vindication to the strategy of Ref. [3] used in this work, suggesting that the width-8 cylinders that we rely on in our study approximate the 2D behavior very well.

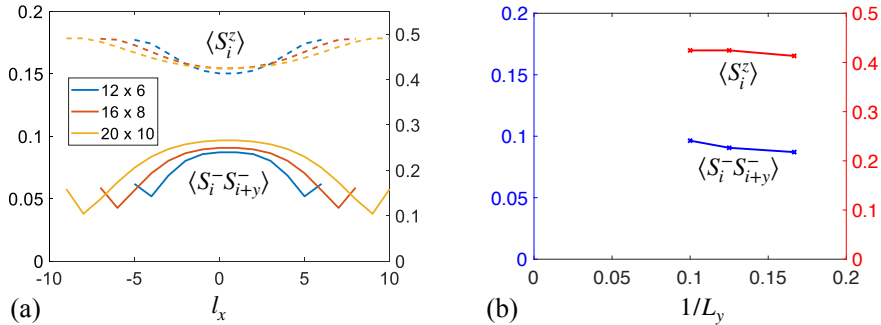


Figure C.3: Finite-size scaling of the nematic order parameter and z -axis magnetization in the nematic phase for $h = 0.96$ and $J_2 = 0.7$. (a) Nematic order parameter $\langle S_i^- S_{i+y}^- \rangle$ (left axis) and z -axis magnetization $\langle S_i^z \rangle$ (right axis) along the cylinder for the three cluster sizes of the same aspect ratio 2.0. There is a weak symmetry-breaking pairfield $0.1S_i^- S_{i+y}^-$ applied to both edges. (b) $1/L_y$ -scaling of $\langle S_i^- S_{i+y}^- \rangle$ and $\langle S_i^z \rangle$ at the center of the cylinders in (a).

C.4 Dipole and quadrupole order parameters in a Heisenberg antiferromagnet

In a multipole expansion, higher-order multipole correlations can exist merely as a byproduct of the lower-order ones, so the nematic (quadrupolar) order parameter should always be detectable in the presence of the conventional dipolar order. In this section, we present a numerical demonstration of this effect for the $J_1 > 0$, nearest-neighbor Heisenberg antiferromagnet in a magnetic field. By highlighting its differences from the J_1 - J_2 ferro-antiferromagnetic model that we study in the present work, we further confirm that the existence of the pure nematic phase in the J_1 - J_2 model is *not* a byproduct of the dipolar order.

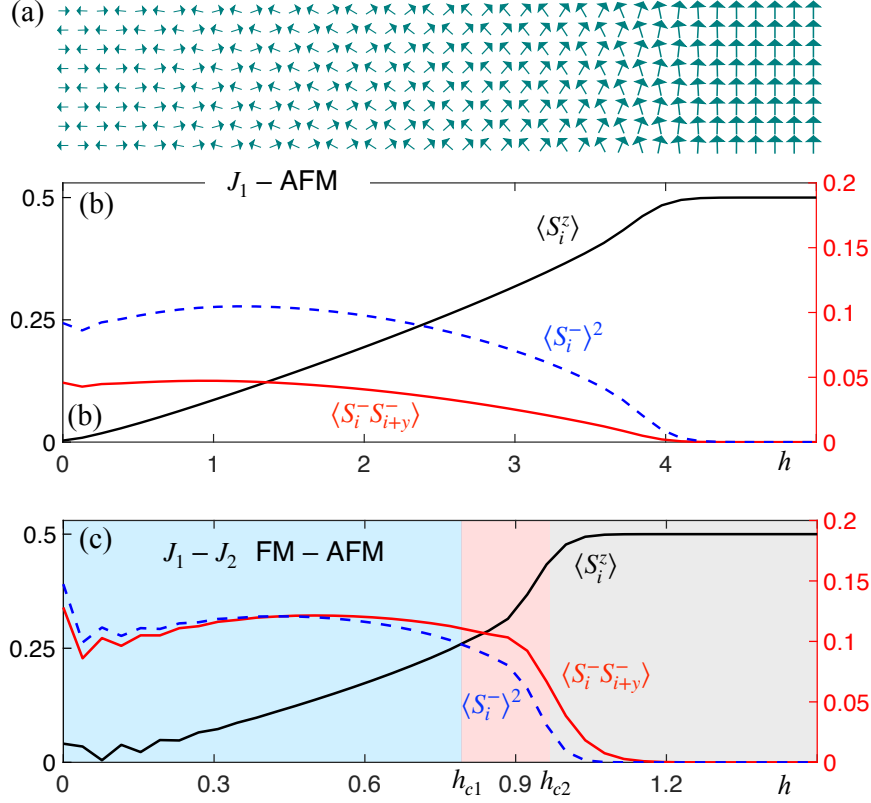


Figure C.4: (a) Spin configuration in a long-cylinder scan of the Heisenberg J_1 -AFM, with the magnetic field varying linearly across the length of the cylinder from zero to above the saturation field. (b) Magnetization $\langle S_i^z \rangle$ (left axis), square of the dipolar order parameter, $\langle S_i^- \rangle^2$, and the quadrupolar order parameter $\langle S_i^- S_{i+y}^- \rangle$, (right axis) along the cylinder in (a). (c) The same order parameters as in (b) for the J_1 - J_2 FM-AFM model for $J_2 = 0.7$, as in Fig. 4(b) of the main text, but for a wider field range. The shaded regions are the phases from the naive phase diagram in Fig. 1(a) of the main text based on the values of h_{c1} and h_{c2} . The actual AFM to nematic phase boundary is at $h \approx 0.95$, which is way above h_{c1} and only slightly below h_{c2} .

In Figs. C.4(a) and C.4(b) we show the DMRG results for the long-cylinder scan of the Heisenberg J_1 -AFM in a magnetic field, with $J_1 = 1$ set as the energy unit. The magnetization curve shown in Fig. C.4(b) agrees very closely with the prior spin-wave calculation [299]. One can see that the spin canting, demonstrated by the square of the order parameter, $\langle S_i^- \rangle^2$, occurs below saturation field with no sign of an intermediate nematic phase. There is also a finite quadrupolar order parameter, $\langle S_i^- S_{i+x(y)}^- \rangle$, which is detected alongside the dipolar order, but not independently. Furthermore, the dipolar order is always stronger than the

quadrupolar one throughout our scan, with no region where the former can dominate and indicate a possible occurrence of the pure nematic state.

This should be contrasted with the scan of the J_1 - J_2 ferro-antiferromagnetic model for $J_2 = 0.7$, as in Fig. 4(b) of the main text, but for a wider field range, shown in Fig. C.4(c). One can observe a region near the saturation field where the ordered moment has deviated from the full saturation, but shows no spin canting, also indicated by the dominant quadrupolar order, $\langle S_i^- S_{i+y}^- \rangle$, with the suppressed or vanishing dipolar one, $\langle S_i^- \rangle^2$, in this region. These are the distinct features of the spin nematic phase as we argue and analyze in more detail in the main text.

Appendix D

Supplemental materials for Chapter 5

D.1 phase boundaries from the DMRG scans

Here we illustrate how we determine the approximate phase boundaries and corresponding error bars from the DMRG scans. In Figure D.1, we show the in-plane, $|\langle S_i^x \rangle|$, and out-of-plane, $|\langle S_i^z \rangle|$, ordered moments along the DMRG J_3 -scan in Fig. 2(b) of the main text. Spins in the FM and ZZ phases are along the x axis, while in the Iz phase they order along the z axis. The transition points are chosen as the crossing points of their order parameters. Error bars are either the distance to the inflection points of the order-parameter curves or a minimum of one step of the scan (one column of the cylinder) for sharper transitions.

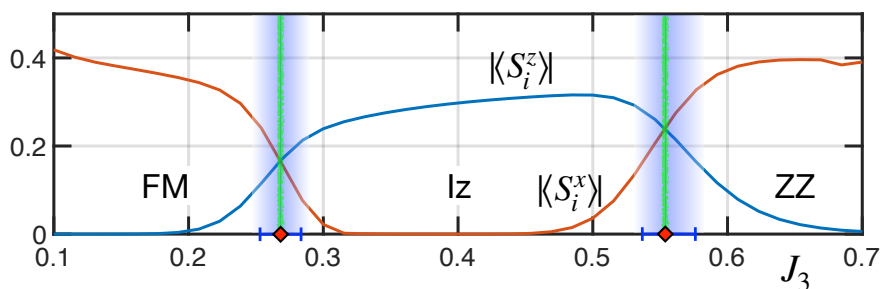


Figure D.1: $|\langle S_i^z \rangle|$ and $|\langle S_i^x \rangle|$ along the length of a 16×40 cylinder in a DMRG scan vs J_3 for the $\Delta = 0$ limit of the $J_1^\Delta - J_3$ model. The crossing points are the phase boundaries and the shaded regions are the error bars.

D.2 Proximity effect in the scans and the absence of an spiral phase

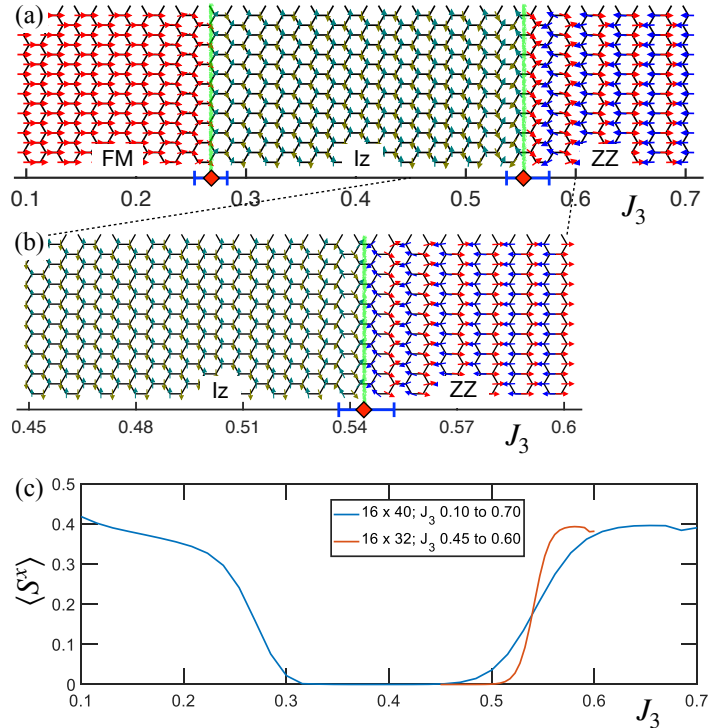


Figure D.2: Results for the J_1^Δ - J_3 model at $\Delta=0$. (a) The J_3 -scan from Fig. 2(b) of the main text. (b) The “zoom-in” J_3 -scan of the Iz-to-ZZ transition region in the 16×32 cylinder. (c) The column-averaged $\langle S^x \rangle$ vs J_3 for the scans in (a) and (b).

In some DMRG scans, such as the one in Fig. 2(b) of the main text, reproduced in Fig. D.2(a), spins at the boundary between the Iz and other phases appear to form a spiral pattern. To rule out an additional intermediate spiral phase, we perform a scan in a smaller range of the varied parameter (“zoom-in” scan) to observe the boundary region closer. In Fig. D.2(b) we focus on the transition region between the Iz phase and the ZZ phase. If the spiral phase would exist, it would become wider in such a scan. In Fig. D.2(b), the transition region has the same width (about ten columns) as in Fig. D.2(a), with the transition getting sharper for the smaller gradient of J_3 , see Fig. D.2(c), strongly suggesting the absence of any intermediate phase in the thermodynamic limit. In the non-scan calculation at $J_3=0.55$ we also do not find the spiral phase. This analysis clearly shows that the spiral-like pattern

in the scans is due to a proximity effect at the phase boundary. Similar verifications were carried out for all suspicious phases in all scans.

D.3 DMRG results for the J_1^Δ - J_2^Δ model

Ref. [281] has studied the J_1 - J_2 - J_3 XXZ model, demonstrating a potentially richer structure of its phase diagram compared to the J_1 - J_3 model investigated in our work. Specifically, it was suggested that the spin-liquid phase in the isotropic Heisenberg limit is stable in a much wider region along the J_1 - J_2 axis than along the J_1 - J_3 axis, with a specific point $J_2 = 0.18$ studied in more detail. In that work, an XXZ cut of the J_1^Δ - J_2^Δ model along the Δ -axis for $J_2 = 0.18$ (and $J_3 = 0$) was also investigated, and a transition to an incommensurate phase from an SL phase was identified near the Heisenberg limit, at $\Delta = 0.96$, with a wide range of the incommensurate phase extending down to the low values of Δ .

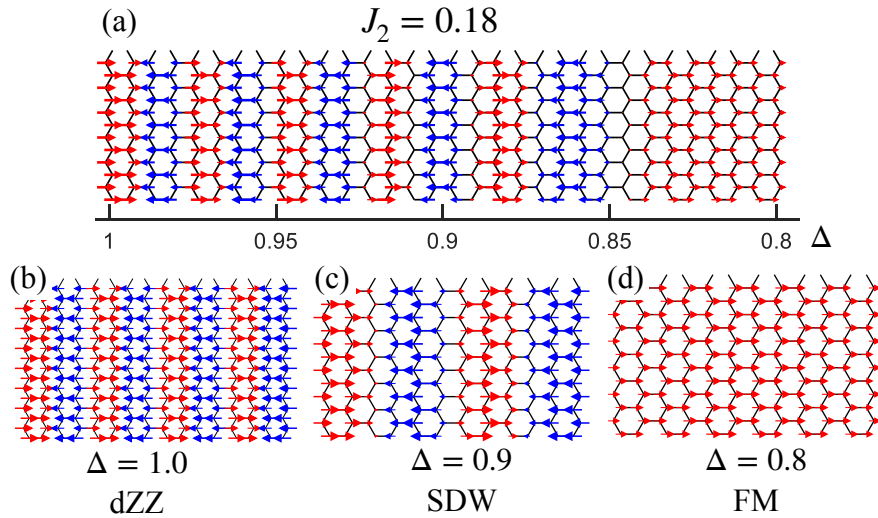


Figure D.3: Results for the J_1^Δ - J_2^Δ model for $J_2 = 0.18$. (a) DMRG scan on 12×32 cylinder vs Δ , and (b), (c), and (d) are non-scans on 16×16 and 12×12 cylinders for three representative values of Δ .

Here we briefly present our additional results for the J_1^Δ - J_2^Δ model for this specific choice of $J_2 = 0.18$ and $J_3 = 0$, thus extending our work in a different region of the parameter space.

The summary of our results is the following. We do not find any evidence for a spin-liquid state in the Heisenberg limit of this model, and find a double-zigzag state instead. This is similar to our results for the dZZ state in the J_1 - J_3 model, found instead of the SL state suggested in Ref. [281], as is discussed in the main text. For the 1D phase diagram along the Δ -axis for the same choice of $J_2=0.18$ and $J_3=0$, we find two transitions, one at $\Delta=0.93(2)$ and the other at $\Delta=0.86(2)$. The lower one is a transition to a FM state, with no sign of the incommensurate phase. While the existence of a transition at $\Delta=0.93(2)$ is, ideologically, in agreement with the transition found in Ref. [281], in our case it is between a dZZ phase and a potentially novel triple-zigzag state that also has a significant modulation of spins, characteristic of that of the spin-density wave (SDW). We refer to it as to tZZ-SDW state.

The numerical results to substantiate these findings are presented in Fig. D.3. The Fig. D.3(a) part shows a scan calculation at $J_2=0.18$ vs Δ from the Heisenberg limit down to $\Delta=0.8$. The double zigzag phase at the isotropic limit ($\Delta=1.0$) evolves into a FM state via an intermediate phase. The non-scan calculations in Fig. D.3(b) and Fig. D.3(d) confirm the dZZ and the FM phases at the respective ends of the scan, with both exhibiting a robust order. The non-scan for the intermediate phase at $\Delta=0.9$ in Fig. D.3(c) retains the characteristics of the SDW state, as the spin's magnitude is not varied in a fashion that would be consistent with a "simple" triple-zigzag phase. While it is possible that the SDW variation may be an artifact of the finite cluster as the tZZ phase has a large unit cell, the dZZ phase in the J_1 - J_3 case is much more symmetric and we believe that the observed SDW variation is genuine.

Lastly, we note that in the energy comparison for the J_1 - J_3 Heisenberg case discussed in the main text and shown in Fig. 3(b), we have also investigated a stability of the triple-ZZ state. The tZZ did come very close near the FM-dZZ boundary, but did not become the ground state in that limit. In that sense, the stabilization of the tZZ phase, or a descendant of it, in a different part of the phase diagram does not come as a complete surprise.

D.4 Minimally augmented spin wave theory

The spin-wave approach is based on the $1/S$ -expansion about a classical ground state of a spin model using bosonic representation for spin operators [300]. Since the classical energy is at a minimum, the first non-zero term of the expansion is quadratic (harmonic), yielding the linear spin-wave theory (LSWT) Hamiltonian in a standard form

$$\mathcal{H} = E_{cl} + \frac{1}{2} \sum_{\mathbf{q}} \left(\hat{\mathbf{x}}_{\mathbf{q}}^\dagger \hat{\mathbf{H}}_{\mathbf{q}} \hat{\mathbf{x}}_{\mathbf{q}} - \frac{1}{2} \text{tr}(\hat{\mathbf{H}}_{\mathbf{q}}) \right) + O(S^0), \quad \hat{\mathbf{H}}_{\mathbf{q}} = \begin{pmatrix} \hat{\mathbf{A}}_{\mathbf{q}} & \hat{\mathbf{B}}_{\mathbf{q}} \\ \hat{\mathbf{B}}_{\mathbf{q}}^\dagger & \hat{\mathbf{A}}_{-\mathbf{q}}^* \end{pmatrix}, \quad (\text{D.1})$$

where E_{cl} is the classical energy, $O(S^2)$, $\hat{\mathbf{x}}_{\mathbf{q}}^\dagger = (\hat{\mathbf{a}}_{\mathbf{q}}^\dagger, \hat{\mathbf{a}}_{-\mathbf{q}})$ is a vector of the bosonic creation and annihilation operators, and $\hat{\mathbf{H}}_{\mathbf{q}}$ is the Hamiltonian matrix, $O(S)$, in this basis. The diagonalization of $\hat{\mathbf{g}}\hat{\mathbf{H}}_{\mathbf{q}}$, where $\hat{\mathbf{g}}$ is the diagonal para-unitary matrix, yields the LSWT magnon eigenenergies $\{\varepsilon_{1\mathbf{q}}, \varepsilon_{2\mathbf{q}}, \dots, -\varepsilon_{1-\mathbf{q}}, -\varepsilon_{2-\mathbf{q}}, \dots\}$ [301] that are *guaranteed* to be positive definite because the expansion is around a minimum of the classical energy.

From that, the energy of the ground state to the order $O(S)$ is $\mathcal{E} = E_{cl} + \delta E$, where δE is the $1/S$ quantum correction

$$\delta E = \frac{1}{2} \sum_{\mathbf{q}} \left(\sum_{\alpha} \varepsilon_{\alpha\mathbf{q}} - \text{tr}(\hat{\mathbf{A}}_{\mathbf{q}}) \right). \quad (\text{D.2})$$

When the classical state stops being a minimum as some parameter of the model is varied, the quadratic Hamiltonian in (D.1) ceases to be positive definite, with some of the $\varepsilon_{\alpha\mathbf{q}}^2$ turning negative for some momenta \mathbf{q} , and the quantum correction in (D.2) becoming ill-defined. This hinders the use of the LSWT outside the classical region of stability of a state and limits its ability to describe the shift of the phase boundaries between classical states due to

quantum effects and the appearance of the ordered phases that are not favored classically but stabilized in a quantum case.

The resolution to this general conundrum that has plagued application of the SWT to the classically unstable states was suggested in Refs. [283–285]. The method consists of adding a local field term to the Hamiltonian, $\delta\mathcal{H} = \mu \sum_i a_i^\dagger a_i$ (see the main text) and referred to as the *minimally augmented SWT* (MAGSWT). The minimal value of this field is chosen from the condition that all eigenvalues $\varepsilon_{\alpha\mathbf{q}}^2$ are positive definite for all the momenta \mathbf{q} .

D.4.1 LSWT for the phases of the J_1 – J_3 model

The classical energies of the collinear phases of interest per number of atomic unit cells N_A are given by

$$E_{cl}^{\text{FM}} = -3S^2(1 - J_3), \quad E_{cl}^{\text{ZZ}} = -S^2(1 + 3J_3), \quad E_{cl}^{\text{Iz}} = 3S^2(\Delta_1 - J_3\Delta_3), \quad E_{cl}^{\text{dZZ}} = -2S^2, \quad (\text{D.3})$$

valid for any J_3 and $\Delta_{1(3)}$ of the model (1) of the main text, inside or outside the phase’s stability region.

Of the five phases in Fig. 1 of the main text, the magnetic unit cell in the FM and Iz phases is naturally that of the honeycomb lattice (two sites), while for the ZZ and Sp ones it can be reduced to that by the staggered or rotated reference frames, respectively, resulting in the 4×4 Hamiltonian LSWT matrix $\hat{\mathbf{H}}_{\mathbf{q}}$ (D.1) in all four cases. For the dZZ phase, the staggered reference frame reduces the unit cell from eight to four sites and yields the 8×8 LSWT matrix.

The LSWT treatment of the collinear phases is rather standard and we do not elaborate on it except for a few details. In all two-sublattice cases, FM, ZZ, Iz, and Sp, the LSWT matrices $\hat{\mathbf{A}}_{\mathbf{q}}$, $\hat{\mathbf{B}}_{\mathbf{q}}$ in (D.1) assume the same structure, for which the eigenvalues of the 4×4

Hamiltonian matrix can be found analytically. One can find additional simplifications of the eigenvalue problem for the FM and Iz phases, and in all four cases in the limit $\Delta_{1(3)}=0$, see also Ref. [278] for the limiting cases for the Sp phase.

In the 4-sublattice dZZ case, the eigenvalue problem for the 8×8 matrix is not reducible to a compact analytical form. However, analytical solutions are available for the eigenenergies at the high-symmetry $\mathbf{q} = 0$ and $\mathbf{q} = (0, \pi/\sqrt{3})$ points in the Heisenberg limit, which are instrumental for finding the MAGSWT parameter μ .

D.4.2 Finding μ in MAGSWT

In the FM, ZZ, and Iz phases, the search for the minimal value of μ for the MAGSWT follows a similar pattern. In a simplified case, such as full XXZ ($\Delta_1 = \Delta_3$) or XY limits, analytical expression for the lowest branch $\varepsilon_{1\mathbf{q}}^2$ simplifies sufficiently to yield the J_3 -dependence of the offending negative minimum that needs to be lifted up by a positive shift. The required energy shift is easily related to μ with the Δ -dependence of μ either absent or following trivially from the considered limiting cases. The resulting solutions correspond to a change of the diagonal matrix element $A \rightarrow \bar{A}$ of the LSWT matrix $\hat{\mathbf{A}}_{\mathbf{q}}$, with \bar{A} in all three cases given by

$$\bar{A} = A + \mu = 3S |\bar{\gamma}_{\mathbf{Q}_{\max}}|, \quad \text{where } \bar{\gamma}_{\mathbf{q}} = \gamma_{\mathbf{q}} - J_3 \gamma_{\mathbf{q}}^{(3)}, \quad (\text{D.4})$$

with the first- and third-neighbor hopping amplitudes $\gamma_{\mathbf{q}} = \frac{1}{3} \sum_{\alpha} e^{i\mathbf{q}\delta_{\alpha}}$ and $\gamma_{\mathbf{q}}^{(3)} = \frac{1}{3} \sum_{\alpha} e^{i\mathbf{q}\delta_{\alpha}^{(3)}}$, and \mathbf{Q}_{\max} defined as

$$\mathbf{Q}_{\max} = \begin{cases} (0, 0), & J_3 < J_{3,c1} = 0.25, \\ (Q_x, 0), \quad Q_x = \frac{2}{3} \cdot \arccos\left(\frac{1}{2J_3} \cdot \frac{1-3J_3}{1-2J_3}\right), & J_{3,c1} < J_3 < J_{3,c2}, \\ (2\pi/3, 0), & J_3 > J_{3,c2} = (\sqrt{17} - 1)/8 \approx 0.3904, \end{cases} \quad (\text{D.5})$$

Technically, the condition for the maximum of $|\bar{\gamma}_{\mathbf{q}}|$ is related to that of the classical energy minimum in the Sp phase.

Interestingly, the resultant MAGSWT spectrum in the Iz phase and the quantum energy correction (D.2) that derives from it, are fully independent of the anisotropy parameters Δ_n .

In the dZZ case, the search of μ has involved analysis of the spectrum obtained by a numerical diagonalization of the $(\hat{\mathbf{g}}\hat{\mathbf{H}}_{\mathbf{k}})^2$ matrix in the Heisenberg limit, which helped in identifying the relevant high-symmetry \mathbf{q} points that require stabilization corrections. The diagonalization at these points can be reduced to an analytical form, which, in turn, yields the minimal value of μ . In a narrow region of $0.1892 < J_3 < 0.2030$, the two lowest unstable branches trade places and, in a row, develop negative minima at small but finite \mathbf{q} 's. For that region, we find that a straightforward linear interpolation for μ between the analytic solutions from the neighboring regions is the most effort-effective, as it stabilizes the spectrum if not with zero but with a very small gap. The resultant explicit expressions for μ are

$$\mu = \begin{cases} S \left(\sqrt{5 - 2J_3 + J_3^2} - 1 - 3J_3 \right), & J_3 < \tilde{J}_{c1} = 0.1892, \\ \text{interpolate,} & \tilde{J}_{c1} < J_3 < \tilde{J}_{c2} = 0.203, \\ 2S \left(\sqrt{2 - 2J_3 + J_3^2} - 1 \right), & \tilde{J}_{c2} < J_3 < \tilde{J}_{c3} = 0.25, \\ 2SJ_3, & J_3 > \tilde{J}_{c3}. \end{cases} \quad (\text{D.6})$$

As in the other coplanar phases, FM and ZZ, μ is independent of the XXZ anisotropies Δ_n .

D.4.3 Energies

Following the MAGSWT strategy, quantum corrections to the groundstate energies in all competing phases can now be calculated in a conventional $1/S$ fashion using Eq. (D.2) with the expressions for the minimal chemical potential from (D.4) and (D.6). Then the total energies $\mathcal{E}(J_3, \Delta)$ can be compared between the phases to create the phase diagram.

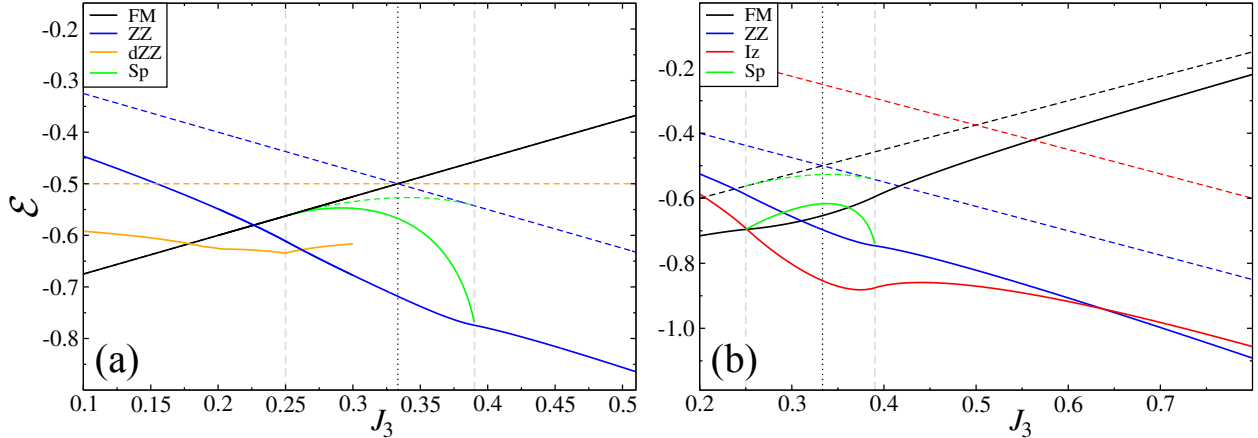


Figure D.4: (a) The classical (dashed lines) and quantum (solid lines, from (D.2)) energies of the FM, ZZ, Sp, and dZZ states vs J_3 for $\Delta_{1(3)} = 1$ per atomic unit cell. The vertical dashed lines are classical FM-Sp and Sp-ZZ boundaries and the dotted line is the crossing of E_{cl} for the FM and ZZ states. (b) Same as (a) for the FM, ZZ, Sp, and Iz states for $\Delta_1 = 0$ and $\Delta_3 = 1$.

Figure D.4(a) shows the J_3 energy-cuts in the Heisenberg limit, $\Delta_{1(3)} = 1$, of the J_1 - J_3 model. The dashed lines are classical energies (D.3) and solid lines are energies with quantum corrections (D.2). The vertical dashed lines are classical FM-Sp and Sp-ZZ boundaries, $J_{3,c1}$ and $J_{3,c2}$. The dotted line is the intersection of the FM and ZZ classical energies, $J_3 = 1/3$. The Iz phase is not competitive. The Sp phase uses standard SWT with no augmenting as it is stable through its extent. The FM is an exact eigenstate, so the quantum corrections to it are zero.

The first effect is the expansion of the ZZ phase (blue lines). While the FM is fluctuation-free, the ZZ is not, which pushes its energy down and the crossing with the FM's energy below the $J_{3,c1}$ point where the FM is unstable classically, superseding the non-collinear Sp phase, which is not effective in lowering its energy. However, near $J_{3,c1}$ another collinear phase, dZZ, is competitive, making it a ground state in a finite range of J_3 (orange lines).

One can note a very close agreement of the MAGSWT dZZ-ZZ transition at $J_3 = 0.262$ compared to the DMRG value of 0.26. On the other hand, the FM-dZZ transition is at a lower $J_3 = 0.1785$ than the DMRG one at $J_3 \approx 0.24$. One can ascribe this difference to a

larger sensitivity of the MAGSWT phase boundaries to the higher-order corrections in this case because FM state is non-fluctuating in the Heisenberg limit.

For the “partial” XY limit, with $\Delta_1 = 0$ and $\Delta_3 = 1$, see Figure D.4(b). In this case, dZZ is not competitive, but Iz is. All phases are fluctuating in this limit, including FM. The Sp phase is not effective in benefiting from quantum fluctuations. The transition point between FM and ZZ phase is renormalized to a slightly smaller J_3 from its classical value. However, both are overtaken by the strongly-fluctuating Iz phase in a wide window of J_3 . One observation is that while the FM- Iz transition is associated with a rather steep energy crossing, the Iz -ZZ crossing is rather shallow, suggesting stronger higher-order effects on the MAGSWT phase boundary for the latter, but not the former. This is in accord with the numerical values: $J_3 \approx 0.269(15)$ [DMRG] vs 0.2513 [MAGSWT] for the FM- Iz boundary and $J_3 \approx 0.554(23)$ [DMRG] vs 0.637 [MAGSWT] for the Iz -ZZ boundary. Similar discrepancies for the finite Δ_1 in the phase diagram in Fig. 1(b) of the main text can be attributed to the same effect.

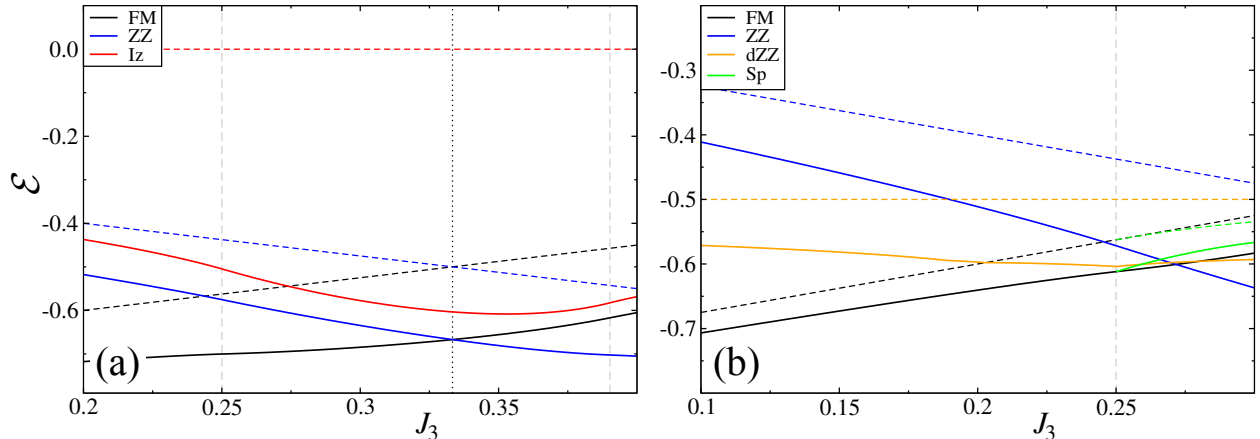


Figure D.5: (a) Same as in Fig. D.4(b) for the FM, ZZ, and Iz states in the “full” XY limit, $\Delta_1 = \Delta_3 = 0$. (b) Same as in Fig. D.4(a) for the FM, ZZ, Sp, and dZZ states for $\Delta_1 = 0.5$ and $\Delta_3 = 1$.

We note that in the “partial” XY case in Fig. D.4(b), the Heisenberg J_3 -term helps to stabilize the Iz state. The effect of the Δ_3 anisotropy is tested by the “full” XY limit of the model, in which the benefit of the out-of-plane spin-coupling is absent. The J_3 -cut in

this limit is shown in Figure D.5(a). The Iz phase can be seen as remarkably effective at lowering its energy, with the quantum fluctuation part being about four times of that for the FM and ZZ states. However, while being closely competitive, the Iz phase is not stable in the full XY limit according to MAGSWT. This result is, superficially, in a disagreement with the DMRG, which does show a narrow strip of the Iz phase in Fig. 5 of the main text. Nevertheless, with the energy curves in Fig. D.5(a) and Fig. D.4(b) in mind, it is clear that the MAGSWT misses Iz phase in the full XY limit only slightly.

An additional J_3 -cut for $\Delta_1 = 0.5$ and Heisenberg J_3 is shown in Fig. D.5(b). Here, the competing phases are the same as in Fig. D.4(a), with the dZZ phase coming extremely close, but not able to stabilize, yielding a direct FM-ZZ transition for this value of Δ_1 . This is in a close agreement with DMRG, which shows a narrow dZZ slice for J_3 between 0.280(4) and 0.290(6) at this Δ_1 , with the FM-ZZ transition being direct for the next cut at $\Delta_1 = 0.4$, see Fig. 1(b) of the main text. Given the energy differences in Fig. D.5(b), the agreement is indeed very close.

Such additional insights into the energetics of the competing phases are instrumental for the understanding of their competition. They also underscore the undeniable success of the MAGSWT in describing classically unstable states.